FLIGHT DATA ANALYSIS AND SIMULATION
OF WIND EFFECTS DURING
AERIAL REFUELING

by

TIMOTHY ALLEN LEWIS

Presented to the Faculty of the Graduate School of

The University of Texas at Arlington in Partial Fulfillment

of the Requirements

for the Degree of

MASTER OF SCIENCE IN AEROSPACE ENGINEERING

THE UNIVERSITY OF TEXAS AT ARLINGTON

May 2008

To my brothers Ben and John,

from whom I have learned much.

ACKNOWLEDGEMENTS

ABSTRACT

FLIGHT DATA ANALYSIS AND SIMULATION

OF WIND EFFECTS DURING

AERIAL REFUELING

Timothy Allen Lewis, M.S.

The University of Texas at Arlington, 2008

Supervising Professor: Atilla Dogan

This thesis presents an analysis of data obtained in an automated aerial refueling test flight conducted with a KC-135 as the tanker and a Learjet 25 as the surrogate receiver UAV. The purpose is to identify the wind induced by the tanker wake and its effect on the receiver aircraft. From the available flight data, a direct computation of the winds experienced by the tanker and receiver is carried out. The mean variation of the receiver wind is compared with the tanker wind when the receiver is at the observation and contact positions. This results in the identification of the wake-induced wind. A spectrum analysis is conducted to characterize the turbulence and to identify the pilot-effects. The thesis also presents methods used to model (i) prevailing wind, (ii) wake vortex induced wind and (iii) turbulence as the three sources of wind that the aircraft are exposed to and the approach used for incorporating the wind effect into the dynamic simulation of the aircraft. The test flight is simulated in various cases with different turbulence models and flight controllers. The simulation results are analyzed and compared with the flight data in terms of the power spectral

densities and mean variations in order to validate the wind and turbulence modeling techniques.

TABLE OF CONTENTS

LIST OF TABLES

CHAPTER 1

INTRODUCTION

1.1 Background

The Air Force Research Laboratory (AFRL) is currently investigating the feasibility of Automated Aerial Refueling (AAR) of UAVs. This program involves a series of flight tests using a KC-135 tanker and a Learjet 25 as a surrogate for the UAV receiver. During the first flight test, the Learjet was flown by a pilot, without an automatic positioning system. The objectives of the flight test were to: (i) verify acceptable handling qualities of the Learjet in the tankers wake, (ii) assess the performance of GPS/EO (electro-optical) guidance for determining relative position, and (iii) obtain flight data for investigating the wake vortex effect on the Learjet. No physical contact was made between the Learjet and the tanker during this test flight and no actual fuel transfer took place.

In the design, development and validation of control algorithms for automated aerial refueling, a mathematical model and computer simulation of the receiver dynamics during the refueling are essential. In order to generate authentic results from the simulation, it is critical to model the receiver aircraft with sufficient accuracy, taking into account all major factors that influence its dynamics. The most significant one of these is the aerodynamic coupling of the receiver with the tanker aircraft through the trailing wake vortex system. This system generates a nonuniform wind field, which is both deterministic and stochastic, over the receiver aircraft, inducing additional forces and moments. It also reduces the reliability of the receiver airspeed

measurement since the measured local airspeed is no longer a true representation of the wind field the aircraft is exposed to.

Recent work [3–16] has dealt with demonstration of the benefit of and issues with the control system development for aerial refueling. Most of this work treats the vortex as an unknown disturbance or stochastic turbulence in the control law development and validation procedure. Since vortex-induced velocities acting on an aircraft are highly nonuniform, standard aerodynamic force and moment equations, based on airspeed, angles of attack and sideslip, and uniform wind components and gradients acting at the center of mass (CM) of the aircraft, cannot be used directly. To overcome this difficulty, two approaches are commonly used [17–19]. The first generates a database of induced forces and moments for a specific pair of aircraft by CFD models or wind tunnel and/or flight test measurements. The required databases can be extremely costly to generate, are too computationally intensive to use for even near real-time simulation, and very difficult to use in control system development. Furthermore, they are specific to certain pairs of aircraft and flight conditions. The second approach is to model the effect of nonuniform wind in a simplified manner, or to treat it as an unknown disturbance and avoid modeling all together. A Vortex Effect Modeling Technique (VEMT) has recently been developed that enables the use of standard dynamic equations of motion and aerodynamic build-up equations with wind effect terms included [20–27]. The technique has proven to be very useful and accurate in the case of formation flight modeling and control [20–22, 24–26]. It has also been implemented for aerial refueling simulation and control design verification [28–31].

1.2   Research Objective and Thesis Content

The objective of this research is to develop a wind effect modeling technique for the receiver aircraft during aerial refueling based on the previously developed VEMT.

The data available from the AAR test flight are used for model validation. The work toward this goal documented in this thesis consists of the following activities:

(i) An analysis of the flight data to extract the motion of the air (wind) for the tanker and the receiver.

(ii) An analysis of the mean variation of the flight data wind for the tanker and receiver to identify the effect of the tanker's wake on the receiver, and to identify the prevailing wind.

(iii) A spectral analysis of the calculated flight data wind to identify stochastic characteristics of the turbulence components.

(iv) The application of the previously developed VEMT to this scenario.

(v) The application of the Dryden turbulence model to this scenario.

(vi) The simulation of the test flight using the wind effect modeling technique.

(vii) A mean variation and spectral comparison of the response of the receiver aircraft in the simulation and in the test flight, to validate the wind effect modeling technique, and to identify the effect of the pilot or controller dynamic response on the receiver.

In this thesis, the KC-135 is referred to as the "tanker" and the Learjet 25 as the "receiver." The "observation" position is the holding position taken by the receiver some distance away from the tanker, and the "contact" or "refueling" position is the position close to the tanker refueling boom taken by the receiver to simulate actual aerial refueling. No physical contact was made between the Learjet and the tanker during this test flight and no actual fuel transfer took place.

CHAPTER 2

MATHEMATICAL CONCEPTS AND TOOLS

This chapter presents the mathematical concepts and tools for aircraft dynamics modeling and digital signal processing used in this thesis.

2.1 Inertial Frame

The inertial frame is a nonaccelerating flat Earth. The inertial frame (I) axes (x_I, y_I, z_I) are aligned with the local north–east–down directions. The origin of the inertial frame is the reference starting point of the test flight. Where test data is given in latitude and longitude, a transformation from geodetic coordinates to a local cartesian space is used. The distortion caused by the flat Earth assumption is not significant for the work in this thesis over the area of interest in this test flight (a 140 km × 120 km rectangular region). The conversion from Earth-centered longitude and latitude to local rectangular coordinates is detailed in Appendix A.

2.2 Aircraft Frames

Aircraft orientation and position are described in this thesis using the common flight dynamics body frame representation. An aircraft has a body frame whose origin is fixed to its center of mass (CM). The body frame axes (x_B, y_B, z_B) are aligned with the body forward–right–down directions, as shown in Fig. 2.1. The body frame translates and rotates with the aircraft. The orientation of the body frame with respect to the inertial frame is parameterized by the 3-2-1 Euler angles (ψ, θ, ϕ), defined in Fig. 2.2. Two aircraft body frames are used in this thesis; the "tanker body

4

frame" (B_T) and the "receiver body frame" (B_R). In addition to the aircraft body frames, each aircraft has an associated wind frame (W_T, W_R) parameterized by the angle of attack and sideslip angle (α, β), defined in Fig. 2.3.
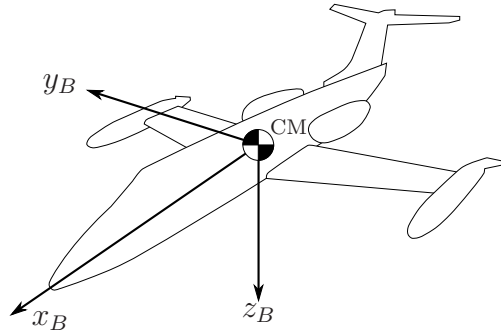
Figure 2.1. Aircraft body frame definition.
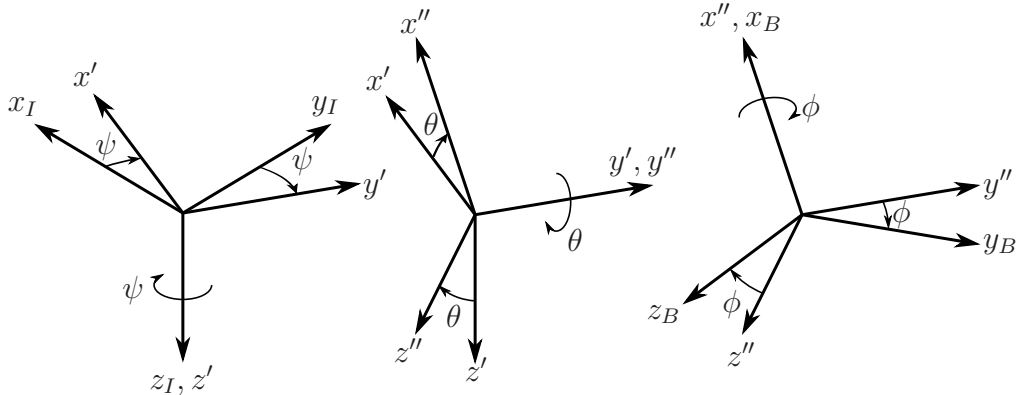
Figure 2.2. 3-2-1 Euler angle rotations from the inertial frame to the aircraft body frame. From left to right: yaw ψ about z_I, pitch θ about y', and roll ϕ about x''.
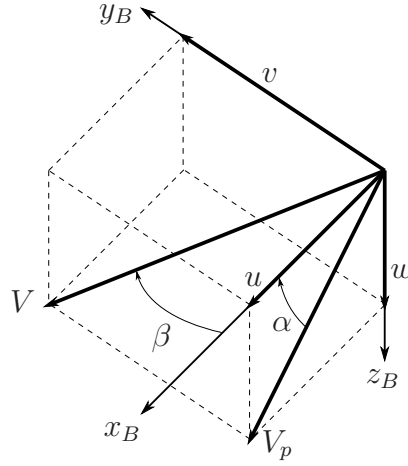
Figure 2.3. Wind frame, angles of attack and sideslip definition. $(u,\ v,\ w)$ are the components of the airspeed vector V. V_p is the projection of V on the x_B–z_B plane.

2.3 Rotation Matrices

This section was adapted from Ref. [1]. Consider a vector $\underline{a}$ that has components $a_X = [a_{1X}\ a_{2X}\ a_{3X}]^T$ when written in the X frame. If $\mathbf{R_{YX}}$ is the rotation matrix from the X frame to the Y frame, then the components of $\underline{a}$ written in the Y frame are given by

$$a_Y = \mathbf{R_{YX}}\, a_X \tag{2.1}$$

Due to the orthonormal property of rotation matrices, the inverse rotation from Y to X is performed by using the transpose of $\mathbf{R_{YX}}$:

$$a_X = \mathbf{R_{YX}^T}\, a_Y \tag{2.2}$$

In the aerial refueling activity that was studied, there are five frames involved: the inertial frame (I), tanker body frame (B_T), tanker wind frame (W_T), receiver body frame (B_R), and receiver wind frame (W_R). The equations of motion for the aircraft employed in this thesis are written in matrix form to facilitate numerical simulations. The matrix equations include rotation matrices to transform the components of a vector from one frame to another. Typically, a vector is written in the most convenient

frame (e.g., airspeed written in the aircraft wind frame) and then transformed to the frame of interest for simulation or dynamical analysis (e.g., the inertial frame or aircraft body frame). The rotation matrices defined between the reference frames in this thesis are shown in Fig. 2.4.
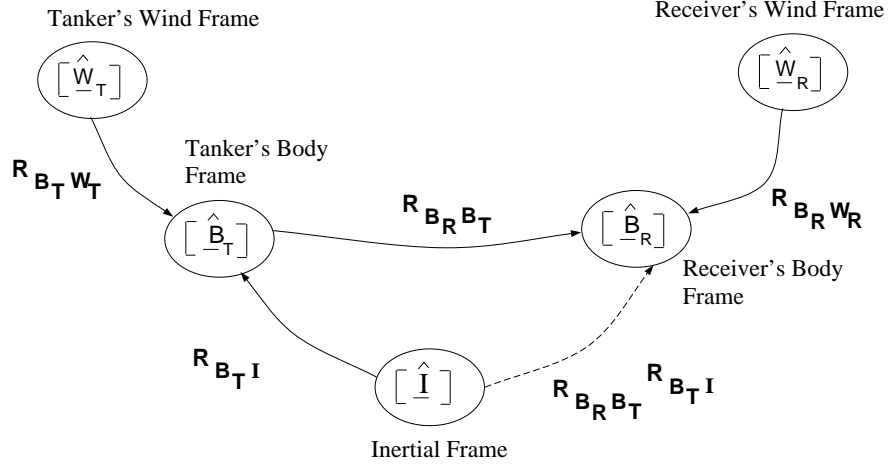
Figure 2.4. Various reference frames and the rotation matrices between them. Reproduced from [1].

For example, the relationship between the components of a vector in the inertial frame and the B_T-frame is

$$a_{B_T} = \mathbf{R_{B_T I}}\, a_I \tag{2.3}$$

where $\mathbf{R_{B_T I}}$ is the rotation matrix from the inertial frame to B_T-frame.

A rotation between two frames can also be accomplished through an intermediate frame. For example, a rotation from the inertial frame to the receiver body frame can be accomplished through the intermediate B_T-frame:

$$\mathbf{R_{B_R I}} = \mathbf{R_{B_R B_T}}\mathbf{R_{B_T I}} \tag{2.4}$$

which simply states that a rotation from the inertial frame to the B_R-frame is equivalent to a rotation from inertial to B_T and then from B_T to B_R.

2.4 Synchronization and Resampling of Digital Signals

The data from the test flight are available as digital signals sampled at different sampling frequencies—primarily 20 or 100 Hz. Additionally, some signals have the same sampling frequency but are not synchronized; i.e., those data acquisition clocks were not started at the same instant, and the measurements were not taken at identical instants during the test flight. In order to perform the airspeed calculations on this data in Chapter 3, it is necessary to both synchronize the measurements and resample some of the data to either 20 or 100 Hz. This ensures all of the data used in the calculation are at the same sampling frequency so that a discrete, homogeneous computation can be performed. The method of resampling is especially important for the receiver data, which will be used for spectral analysis. Resampling should be done in a manner that causes as little distortion of the spectral domain of the signal as possible.

2.4.1 Synchronization

Consider a finite length discrete time signal $y(k)$ with length N and sampling period T, where the discrete index $k = 1, 2, \ldots, N$ corresponds to the continuous sampling time instants $t_y = (k - 1)T$. The sampling frequency of the signal is

$$f = \frac{1}{T} \tag{2.5}$$

Consider another signal $z(k)$ with the same T but whose sample time instants are offset from those belonging to y by a small, arbitrary amount τ. The sampling time instants for z are then given by

$$t_z = t_y + \tau = (k - t)T + \tau \tag{2.6}$$

Therefore, $y(k)$ and $z(k)$ are not synchronized in their sampling instants t_y and t_z. The synchronization of z with t_y is accomplished by linear interpolation. In the

data used here, $\tau \ll T$, so the effect of the interpolation on the data is not considered significant.

2.4.2   Downsampling

The case of resampling a signal from 100 Hz to 20 Hz ("downsampling") requires consideration of the Shannon-Nyquist sampling theorem [32]. The theorem states that if a continuous time signal contains no frequencies higher than f, it can be perfectly reconstructed from a set of samples at a frequency of $2f$. Alternatively, a continuous time signal can be sampled at frequency $2f$, without aliasing if the signal is bandlimited to frequencies less than f. These limitations on the sampling frequency and signal bandwidth are the Nyquist sampling criterion.

The criterion can be applied to downsampling a discrete signal. Consider a hypothetical continuous signal reconstructed from the 100 Hz discrete signal. That hypothetical continuous signal can then be safely sampled at 20 Hz if its bandwidth is less than 10 Hz. This process is accomplished using a digital lowpass filter to limit the bandwidth of the 100 Hz signal to 10 Hz, and then taking every 5th sample $(100/20 = 5)$ to be the new 20 Hz signal. In this thesis, this filtering and sampling is accomplished using the MATLAB resample function [33].

2.4.3   Upsampling

Resampling a signal from 20 Hz to 100 Hz ("upsampling") follows similar reasoning. A 20 Hz signal can be used to reconstruct a hypothetical continuous time signal whose bandwidth is 10 Hz. This hypothetical continuous signal automatically satisfies the Nyquist criterion for sampling at 100 Hz. This is also accomplished in this thesis with the MATLAB resample function.

2.5 Power Spectral Density Calculation

In order to perform the spectral analysis on the flight data in Chapter 3, it is necessary to compute the power spectral density of several digital signals. The flight data represent a finite-length record of discrete-time samples of a continuous physical variable. If the continuous time signal $y(t)$, $t \in (-\infty, \infty)$ is a wide-sense stationary random process, then its power spectral density is given by [34]

$$\phi(\omega) = \int_{-\infty}^{\infty} R(\tau)e^{-j\omega\tau}d\tau \tag{2.7}$$

which is the Fourier transform of the autocorrelation function $R(\tau)$ of $y(t)$. A similar definition exists for the PSD of a discrete time signal $y(k)$, $k = 0, \pm 1, \pm 2, \ldots$ [35]:

$$\phi(\omega) = T \sum_{\kappa=-\infty}^{\infty} R(\kappa)e^{-j\omega T\kappa} \tag{2.8}$$

where T is the sampling period of $y(k)$. Equation (2.8) is the discrete time Fourier transform (DTFT) of the autocorrelation sequence $R(\kappa)$ of $y(k)$. This definition is equivalent to

$$\phi(\omega) = \lim_{N\to\infty} E\left\{ \frac{T}{N} \left| \sum_{k=1}^{N} y(k)e^{-j\omega Tk} \right|^2 \right\} \tag{2.9}$$

where $E\{\cdot\}$ is the expectation operator. Equation (2.9) is the form used in the PSD estimation methods in this thesis. In the above definitions, $\omega \in [-\pi/T, \pi/T]$ is the angular frequency in rad/s. Note that Eqs. (2.8) and (2.9) are often developed in terms of a normalized ω in units of radians per sampling interval, which removes T from the expressions. The forms used here, including the sampling period T, ensure the correct PSD scaling and units for comparison with the continuous PSD function in Eq. (2.7).

The spectral estimation problem is to find an estimate $\hat{\phi}(\omega)$ of the power spectral density $\phi(\omega)$ of the continuous signal $y(t)$ using the finite set of discrete samples

$y(k)$ [36]. In this thesis, both the PSD estimate and the actual PSD are both referred to as the "PSD" where there is no confusion.

There are a number of spectral estimation methods to compute the PSD, the choice of which depends on the signal in question and the desired qualities of the PSD estimate. The Welch method is chosen for this thesis. The Welch method is a common, nonparametric method used in the case for general signals. While MATLAB contains a built-in function to calculate the PSD using the Welch method (the pwelch function), the MATLAB implementation is not fully documented. The Welch method is independently implemented in this thesis based on the algorithm given in Ref. [36]. A summary of the Welch method follows.

Consider a discrete-time signal $y(k)$, where $k = 1, 2, \ldots, N$ and N is the number of samples in or the length of the signal. The periodogram of $y(k)$ is an estimate of the PSD based on Eq. (2.9) with finite N:

$$\hat{\phi}(\omega) = \frac{T}{N} \left| \sum_{k=1}^{N} y(k) e^{-j\omega Tk} \right|^2 \quad \text{(Periodogram)} \quad (2.10)$$

The periodogram provides a statistically poor estimate of the PSD; i.e., the periodogram estimate has a large variance about the true PSD. The Welch method is an adaptation of the periodogram to improve the quality of the PSD estimate. The Welch method divides $y(k)$ into a number of segments, calculates the windowed periodogram of each segment, and then averages the periodograms together to yield the PSD.

Let

$$y_j(k) = y((j-1)K + k), \ k = 1, 2, \ldots, M, \ j = 1, 2, \ldots, S \quad (2.11)$$

be the jth segment of $y(k)$; M is the length of each segment, and K is the amount of overlap between the segments. Then, $(j-1)K$ is the starting point for the jth segment. The M and K are user-chosen parameters. If $K = M$, then the segments

do not overlap. The generally recommended choice is $K = M/2$, which leads to a 50% overlap between the segments. S is the number of segments, given by

$$S = \text{floor}((N - M)/K + 1) \tag{2.12}$$

The windowed periodogram corresponding to $y_j(k)$ is

$$\hat{\phi}_j(\omega) = \frac{T}{MP} \left| \sum_{k=1}^{M} v(k) y_j(k) e^{-j\omega Tk} \right|^2 \tag{2.13}$$

where P is given by

$$P = \frac{1}{M} \sum_{k=1}^{M} |v(k)|^2 \tag{2.14}$$

and $v(k)$ is a windowing function. The windowing function provides a smoothing effect to the periodogram. The $1/P$ term in Eq. (2.13) provides a correction for the added "power" of the windowing function. The Hann window is a common choice and it is used in this implementation. The Hann windowing function is given by

$$v(k) = \frac{1}{2} \left(1 + \cos(\pi k/M) \right) \tag{2.15}$$

The Welch estimate of the PSD is given by:

$$\hat{\phi}(\omega) = \frac{1}{S} \sum_{j=1}^{S} \hat{\phi}_j(\omega) \quad \text{(Welch estimate)} \tag{2.16}$$

which is the average of the windowed periodograms of the segments of $y(k)$. The above implementation does not take advantage of the fast Fourier transform (FFT) and so it is relatively slow in computation. However, the speed was acceptable for the sizes of the data sets in this thesis. Analysis in this thesis is carried out using the temporal frequency f in Hz, and so the conversion $f = \omega/(2\pi)$ from angular frequency ω is used in all cases.

Figure 2.5 shows the Welch estimate of a random sequence (labeled "estimate") compared with the continuous Dryden turbulence model PSD function (labeled "exact") from which the sequence was generated. The Dryden model PSD function is

described in Section 4.3.1. The figure shows the effect the choice of M has on the variance of the PSD estimate. The M should be chosen based on the number of samples N in the discrete signal and the desired amount of smoothing. Smaller segment sizes lead to more segments and more averaging, causing the PSD estimate to be smoother with a lower variance. The overlap amount K has a much smaller effect on the Welch estimate. In this thesis, PSD calculations use a rule of thumb, $M = \text{round}(N/50)$, with 50% segment overlap given by $K = \text{round}(M/2)$, where the rounding functions force M and K to be integers.
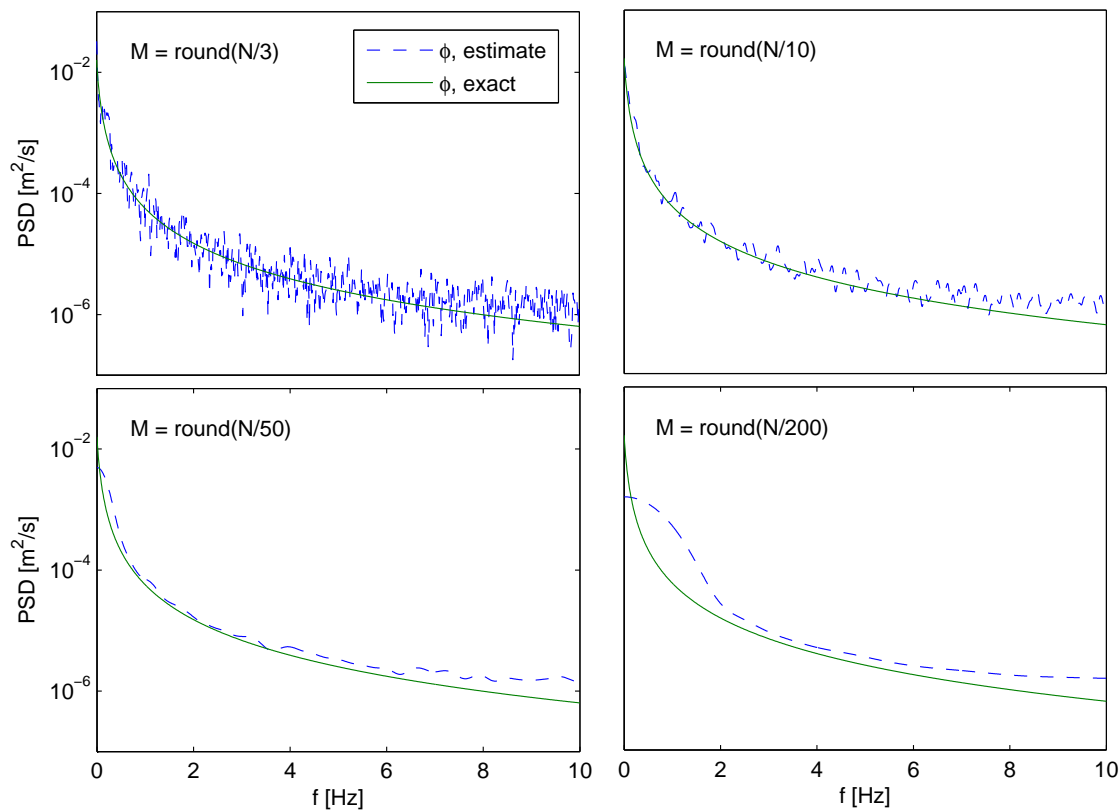
Figure 2.5. Welch estimate compared with actual PSD function, for several values of M.

CHAPTER 3

FLIGHT DATA ANALYSIS

This section details the analysis performed on the data from the test flight. First, the airspeeds of the aircraft are determined from measured air data. The angle of attack and sideslip angle determine the direction of the airspeed vector, giving the motion of the aircraft relative to the air. Further, the motion of the aircraft relative to the inertial frame is known from GPS/inertial velocity measurements. These two aircraft velocities allow the motion of the air relative to the inertial frame (the "wind") to be calculated. Additionally, comparison of the wind experienced by the tanker and the receiver allows the effect of the tanker's wake vortex field on the receiver to be determined. Mean variation and spectral analysis are performed on the wind data to identify characteristics of the wind in the test flight.

3.1   Description of Test Flight

The test flight, depicted in Fig. 3.1, was conducted over Lake Ontario, north of Rochester, NY, on September 22, 2004. An Air National Guard 107th Air Refueling Wing KC-135 was used as the tanker and a Calspan Learjet 25 was used as the surrogate receiver UAV. The test flight was conducted at a nominal altitude of 7010 m and with nominal speed of 190 m/s. Figure 3.2 shows the ground track of the tanker in terms of GPS latitude and longitude in degrees. While the tanker moves on this track, the receiver stays at the observation position or contact position relative to the tanker, or in transition between these two positions. While different time clocks were used during data logging, all clock times recorded in the test flight were eventually

Figure 3.1. Automated aerial refueling test flight.

converted to UTC (Coordinated Universal Time) in seconds, where zero seconds is 22–Sept–2004 00:00 UTC. The numbers printed near the small squares on the tanker track in Fig. 3.2 indicate the start and end times of the observation and contact position passes. Ox and Cx indicate whether the receiver was at the observation or contact position during the specific pass. Note that there are two observation passes and four contact passes.

Figure 3.3 shows the position of the receiver relative to the tanker in UTC time domain. The stripes indicate the time intervals when the receiver was at the observation or contact position. Note that start and end times of the stripes correspond to the UTC times printed in Fig. 3.2.

3.2   Summary of Flight Data Sources

Table 3.1 lists the measured quantities from the flight test data that are used in this thesis. The tanker's calibrated airspeed from the air data avionics was recorded along with pressure altitude at 2 Hz. Similarly, the receiver's avionics provided impact
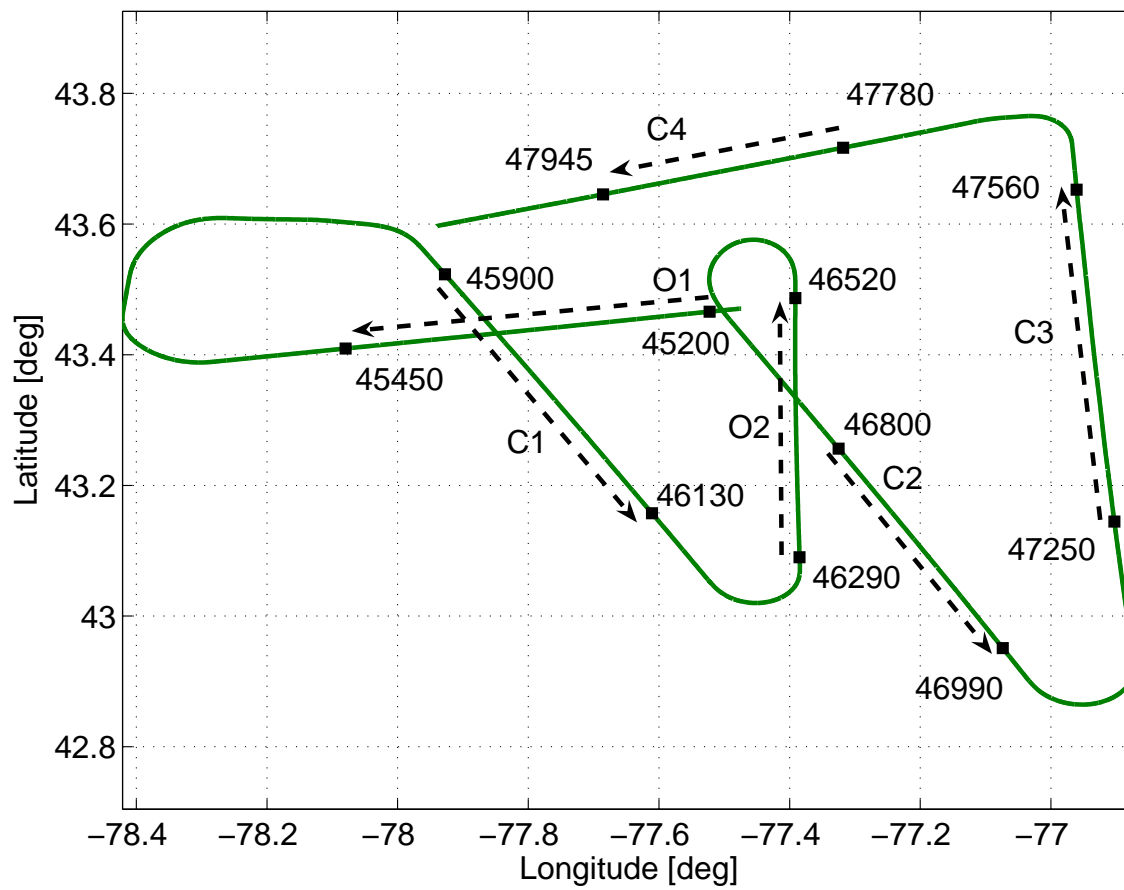
Figure 3.2. Tanker GPS track with start and end times of observation and contact positions passes.
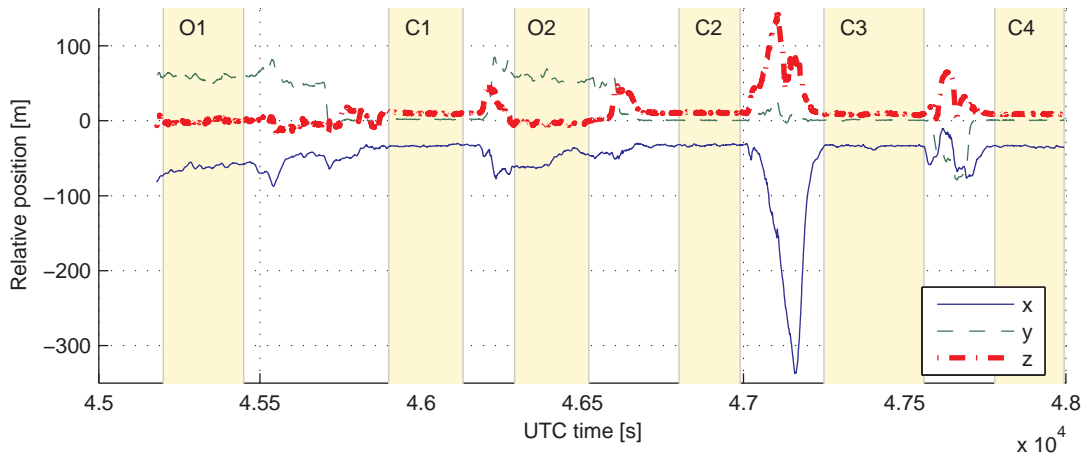
Figure 3.3. Relative position from tanker CM to receiver CM, written in the tanker's body frame.

pressure, static pressure, and total air temperature. Unlike the tanker, the receiver's instruments also provided the angle of attack and sideslip angle, and the control surface deflections. The receiver data were available at 20 Hz. Both aircraft were equipped with identical sets of GPS receivers, which were used for tanker-receiver relative position measurements at 10 Hz. Both aircraft were equipped with Litton LN-100 and LN-251 EGI (embedded GPS-inertial) units, where each provided a separate hybrid GPS-inertial navigation solution. The EGI units were used for ground position and speed, acceleration, orientation, and body angular rates. Both the LN-100 and LN-251 output data at 100 Hz.

For the yaw angle ψ, the EGI units provided two outputs: "platform heading" and "true heading." The true heading angle is used for both the tanker and the receiver in this thesis. This is to ensure that the both EGI units use the same heading angle reference direction (true north).

The flight data measured onboard the tanker and receiver during the test flight were recorded in various data files at different sampling rates, primarily 20 or 100 Hz. The data from different sources were not synchronized, i.e. not sampled at the

Table 3.1. Flight Data Sources.

Tanker

Symbol	Description	Units	Source	Frequency
r_{B_T}	Inertial position	m	EGI	100 Hz
$\dot{r}_{B_T}$	Inertial velocity	m/s	EGI	100 Hz
ψ, θ, ϕ	Yaw, pitch, roll angles	deg	EGI	100 Hz
V_c, VCAS	Calibrated airspeed	m/s	avionics	2 Hz

Receiver

Symbol	Description	Units	Source	Frequency
r_{B_R}	Inertial position	m	EGI	100 Hz
$\dot{r}_{B_R}$	Inertial velocity	m/s	EGI	100 Hz
ψ, θ, ϕ	Yaw, pitch, roll angles	deg	EGI	100 Hz
a_x, a_y, a_z	Acceleration components	m/s^2	EGI	100 Hz
p, q, r	Angular velocity components	deg/s	EGI	100 Hz
ξ	Position relative to tanker	m	GPS	10 Hz
α, β	Angle of attack, sideslip angle	deg	avionics	20 Hz
p, SAP	Static air pressure	Pa	avionics	20 Hz
$p_t - p$, IP	Impact pressure	Pa	avionics	20 Hz
T_t, TAT	Total air temperature	K	avionics	20 Hz
Δp	Differential jet engine pressure	Pa	avionics	20 Hz
δ_e, δ_s	Elevator, stabilizer deflection	deg	avionics	20 Hz

same time instants. Additionally, in some cases, there were discrepancies in the flight data for the same variable provided from multiple data sources. The methods for synchronization and for resampling data are discussed in Section 2.4, and some of the implications of resampling are discussed later in this thesis.

3.3 True Airspeed Calculation

In order to extract the wind information from the available flight data, an accurate calculation of the true airspeed (VTAS) for the tanker and receiver is crucial.

This section describes this calculation, taking special care to include the compressibility and air density corrections, and to avoid using the standard atmosphere model.

3.3.1 True Airspeed of the Receiver

Reference [37] provides an equation for Mach number for subsonic speeds that require consideration of compressibility effect:

$$M^2 = \frac{2}{\gamma - 1} \left[\left(\frac{p_t - p}{p} + 1 \right)^{\frac{\gamma-1}{\gamma}} - 1 \right] \tag{3.1}$$

where $p_t - p$ is the impact pressure (IP) or pressure difference, p is the static air pressure (SAP), and $\gamma = 1.4$, the ratio of specific heats of air at constant pressure and constant volume. Since both IP and SAP are available from the receiver flight data, the Mach number M of the receiver is directly computed. The SAT (Static Air Temperature) is computed using M computed in Eq. (3.1) and the TAT (Total Air Temperature) available from receiver flight data as [38]

$$T = T_t \left(1 + \frac{\gamma - 1}{2} M^2 \right)^{-1} \tag{3.2}$$

where T is the SAT and T_t is TAT. Once SAT and M are computed, the speed of sound V_a is calculated by

$$V_a^2 = \gamma \, R \, T \tag{3.3}$$

where $R = 287.05$ J/kg·K is the gas constant of air. Then, the VTAS of the receiver is computed using

$$V = \sqrt{M^2 \, V_a^2} \tag{3.4}$$

In summary, since IP, SAP, and TAT measurements are available in the flight data, VTAS of the receiver can be computed directly. Further, since the three measured variables are from the same data file at 20 Hz, there is no need for resampling. The airspeed calculated here is therefore a 20 Hz signal.

3.3.2   True Airspeed of the Tanker

The calculation of VTAS of the tanker follows a slightly different approach. This is because the tanker's flight data did not provide IP, SAP, or TAT. Only VCAS (Calibrated Air Speed) measurements are available. The tanker IP is computed using VCAS data as

$$p_t - p = p_0 \left\{ \left[1 + \frac{\gamma - 1}{2} \left(\frac{V_c}{V_{a_0}} \right)^2 \right]^{\frac{\gamma}{\gamma - 1}} - 1 \right\} \tag{3.5}$$

where V_c is VCAS, $p_0 = 101325$ N/m^2 is SAP at STP and $V_{a_0} = 340.3$ m/s is the speed of sound at STP. The IP calculation of the tanker employs STP as a reference and thus may include error by the possible deviation of the actual atmospheric conditions. This tanker IP is calculated from the 2 Hz tanker VCAS data, and so the calculated IP is also a 2 Hz signal.

The tanker IP computed by Eq. (3.5) is compared with the receiver IP. Both aircraft fly in formation in the same air and are exposed to the same possible prevailing wind when the receiver is not in the trailing wake of the tanker, i.e., when it is at the observation position. Thus, the receiver IP should be equal to tanker IP when the receiver is at the observation position. The resultant IP from Eq. (3.5), however, is not the same as the measured IP of the receiver even when the receiver is at the observation position. Therefore, the computed IP of the tanker is calibrated by a constant offset to match the receiver IP when the receiver is in the first observation pass. Figure 3.4 shows the comparison of the tanker IP with the receiver IP after 718.2 Pa (N/m^2) is subtracted from the tanker IP. Note that the callibration factor of 718.2 Pa is about 6% of the measured receiver IP of 11.5 kPa. Although the calibration factor is determined from the first observation pass, the fact that the tanker IP matches the receiver IP in the second observation pass supports the validity of the constant calibration factor.
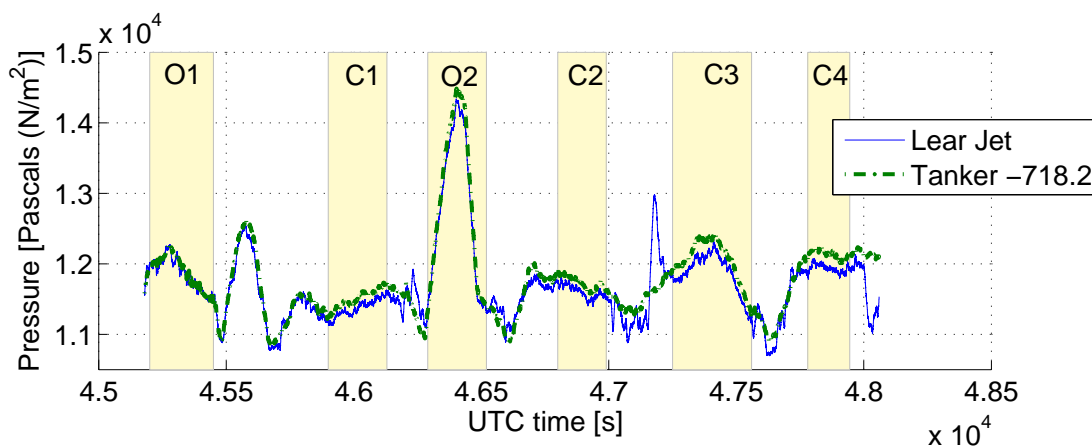
Figure 3.4. Receiver–tanker impact pressure comparison.

Other than IP, SAP and TAT measurements are also missing from tanker flight data. Since both aircraft fly in formation and SAP and TAT are properties of the ambient air, measurements from the receiver can be used for the tanker VTAS calculation. Once the IP, SAP, and TAT for tanker are determined, the procedure explained in Section 3.3.1 is used for calculating VTAS of the tanker. Because some variables are taken from the receiver flight data and used with variables from the tanker flight data, the tanker's VTAS calculation requires resampling and synchronization. In this case, the receiver IP, SAP, and TAT at 20 Hz are resampled and synchronized with the 2 Hz tanker IP. Here, the 20 Hz receiver data are roughly resampled and synchronized by finding the two points closest in time to each tanker sampling instant, and taking their average. This preliminary resampling approach is acceptable for the tanker data since no spectral analysis is performed on the result. Otherwise, the resampling and synchronization should follow the procedure described in Section 2.4.

3.3.3   Comparison of Tanker and Receiver Speeds

Figure 3.5 shows the airspeeds of the tanker and receiver computed in the previous sections as well as GPS-based speeds available from the flight data. A close

examination shows that both aircraft have the same airspeed at observation-1 (see Fig. 3.6). When the receiver goes to the contact position (contact-1 as shown in Fig. 3.6), the receiver airspeed decreases. The same observation can be made from the other observation and contact passes (see Fig. 3.5). Since the receiver aircraft is in the wake of the tanker when it is at the contact position, the decrease in the receiver airspeed at the contact position indicates the presence of vortex-induced wind that the receiver is exposed to whenever it is in the contact position. Further, comparison of the receiver or tanker airspeed with its own GPS-based speed in Fig. 3.5 reveals that during the test flight both aircraft were exposed to headwind or tailwind. When the airspeed is higher than the GPS-based speed (i.e. ground speed), the aircraft are exposed to headwind. Conversely, a lower airspeed is due to tailwind.

Figures 3.5 and 3.6 show that (i) both aircraft were exposed to prevailing wind that switches between headwind and tailwind, (ii) the receiver aircraft was exposed to additional wind when it was in the wake of the tanker, and (iii) high frequency oscillations in both tanker and receiver speeds indicate the presence of turbulence. In the next section, the wind velocities that the aircraft were exposed to will be quantified from the available flight data and the airspeeds computed in this section.
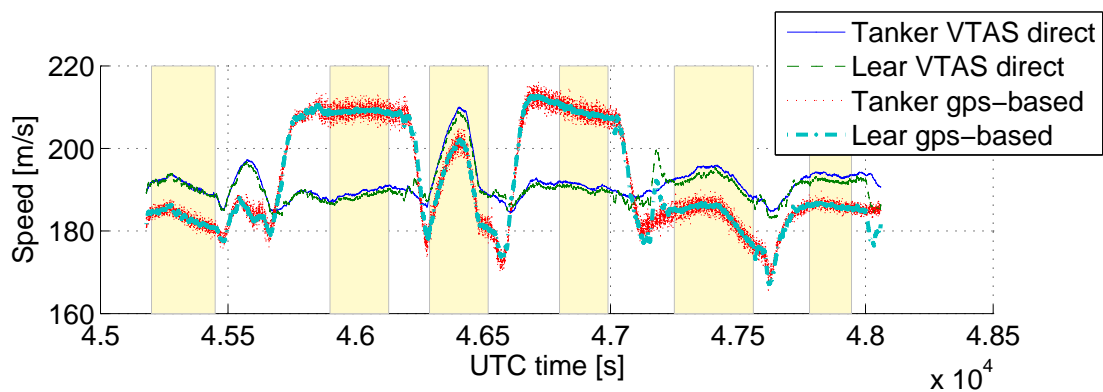
Figure 3.5. Comparison of air and GPS-based speeds of tanker and receiver.
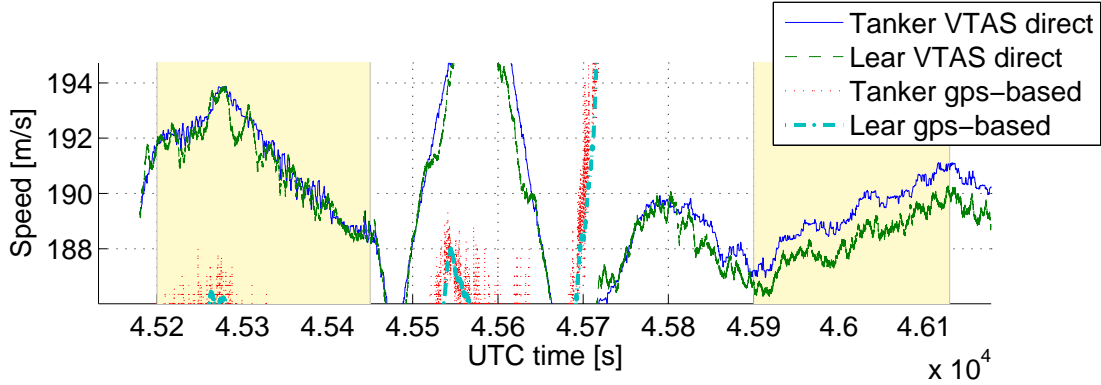
Figure 3.6. Detail view of airspeeds in observation-1 and contact-1 in Fig. 3.5.

3.4 Calculation of Wind Components for Receiver and Tanker

The translational kinematics of an aircraft can be written as

$$V_{\frac{A/C}{Inertial}} = V_{\frac{A/C}{Air}} + V_{\frac{Air}{Inertial}} \tag{3.6}$$

which states that the velocity of an aircraft relative to an inertial frame is the sum of the velocity of the aircraft relative to the air and the velocity of the air relative to the inertial frame. This leads to an expression for the wind that the aircraft is exposed to

$$W_I = \dot{r}_B - \mathbf{R}_{BI}^T \, \mathbf{R}_{BW} \, [V \; 0 \; 0]^T \tag{3.7}$$

where W_I is the representation of the wind vector in the inertial frame, $\dot{r}_B$ is the representation of the aircraft's inertial velocity in the inertial frame, $\mathbf{R}_{BI}$ is the rotation matrix from the inertial frame to the aircraft's body frame, $\mathbf{R}_{BW}$ is the rotation matrix from the aircraft's wind frame to body frame, and V is the aircraft's airspeed.

From the flight data, $\dot{r}_B$ is available as GPS- and/or IMU-based velocity measurement for both the tanker and the receiver, while V is computed in the previous section for both aircraft. The rotation matrix $\mathbf{R}_{BI}$ can be expressed in terms of the 3-2-1 Euler angles, $(\psi, \, \theta, \, \phi)$—yaw, pitch, and bank angles—respectively. The Euler angles of both aircraft are available from their respective flight data. Similarly, the

rotation matrix $\mathbf{R}_{BW}$ is expressed in terms of $(\beta,\ \alpha)$—sideslip angle and angle of attack—respectively. Sideslip angle and angle of attack measurements of the receiver are also available in the flight data. However, the flight data do not provide these angles for the tanker. To carry out the tanker's wind calculation in Eq. (3.7), it is assumed that the tanker's sideslip angle was zero and the angle of attack was equal to its pitch angle throughout the flight. For the receiver's wind calculation, note that Euler angles and GPS/IMU-based velocity measurements are available as 100 Hz data while V is computed as 20 Hz data and $(\beta,\ \alpha)$ are available in 20 Hz from the flight data. Thus, using Eq. (3.7), receiver's wind can be computed (i) as 20 Hz data after downsampling GPS/IMU-based velocity and Euler angles, or (ii) as 100 Hz data after upsampling $(V,\ \beta,\ \alpha)$ data. For reasons discussed later, the 100 Hz signals are all resampled to 20 Hz as described in Section 2.4. The results presented hereafter are from the wind calculation at 20 Hz.

Figure 3.7 presents the results of Eq. (3.7) for both aircraft. Note that the inertial frame is the local north-east-down navigational frame. The first observation from this figure, particularly from tanker-based results, is that during the test flight a prevailing wind was present with varying magnitude and direction relative to north- and east-directions. The down component of tanker-based wind shows a zero mean wind, which implies that no down/updraft as a component of the prevailing wind was present. The down-component of the receiver-based wind clearly shows the downdraft that the receiver experienced whenever it was in the contact position.

Figure 3.8 in general and zooming in on the x-component of the winds in observation-1 and contact-1 in particular (Fig. 3.9) show that the x-component of the receiver-based wind is equal to that of the tanker when the receiver is at the observation position. When the receiver is at the contact position, the two figures clearly show that the x-component of the wind experienced by the receiver is slightly higher.
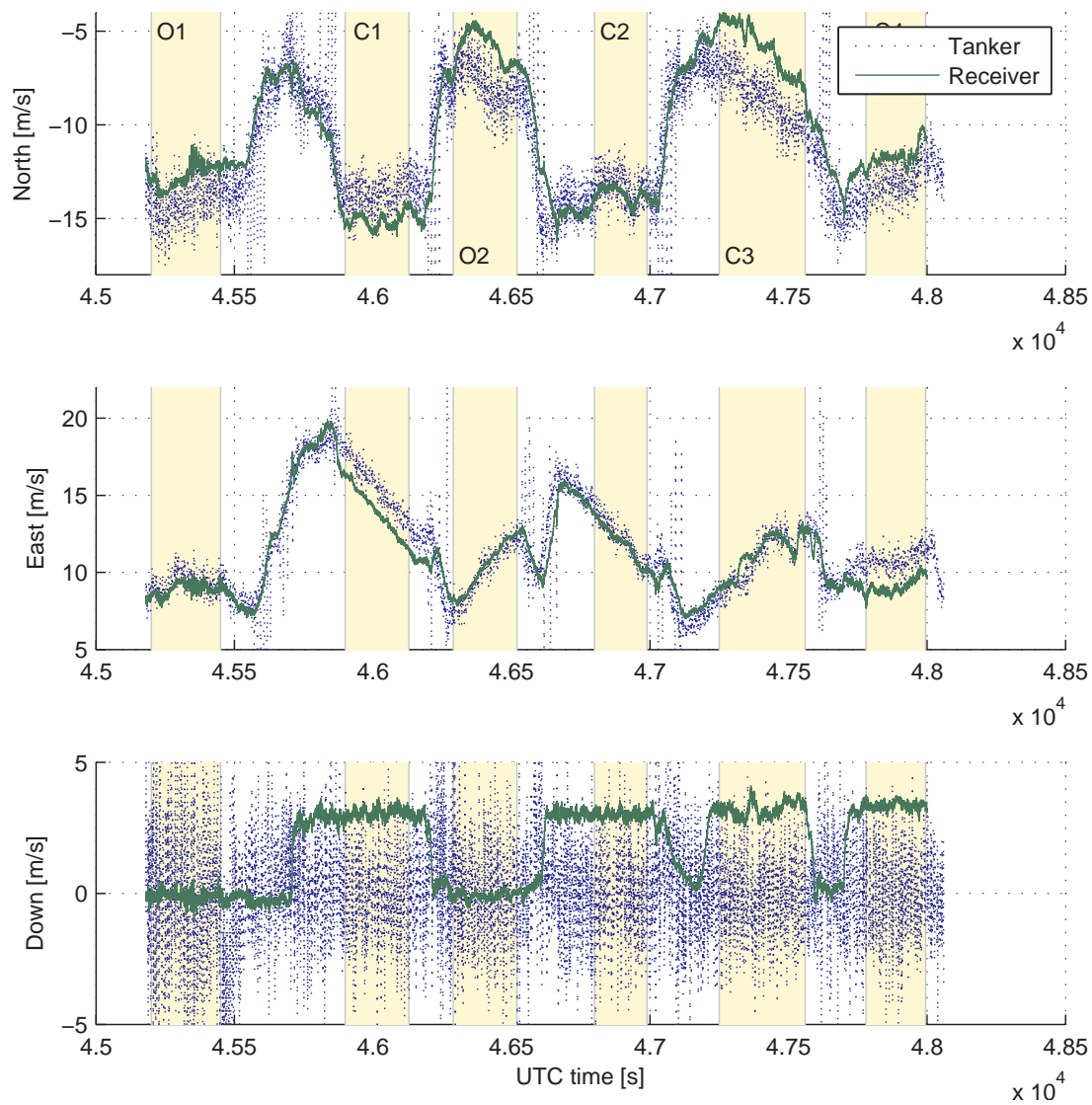
Figure 3.7. Wind components in the inertial frame.

This observation implies that the tanker's wake induced wind has a component in the positive x-direction of the receiver, i.e. wind component blowing towards the tanker. In both observation passes (see Fig. 3.10), note that y-component of receiver wind is slightly higher than that of the tanker. Since the receiver is outside the wake of the tanker when it is at the observation position, the receiver should not experience any additional crosswind. It was expected that both aircraft have the same crosswind as was the case in the x-wind analysis. The observed difference is attributed to possible errors introduced by sensor measurements and the assumption made for the sideslip angle and angle of attack in tanker's wind calculation. Figure 3.10 shows that the difference becomes larger when the receiver goes to the first contact position from the first observation position. The increase is roughly 1.4 m/s. This observation implies that the receiver experiences sidewash induced by the wake vortex at the contact position. The difference is smaller at the second contact position and almost the same as that observed at the observation positions when the receiver was at the last two contact positions. The contact position C1 was offset from the centerline of the tanker while the others were aligned with the centerline. When the receiver is not aligned with the tanker centerline, it experiences sidewash induced by the tanker's wake vortex. This induced sidewash is manifested by the difference observed between the y-components of the tanker and receiver winds.

As observed in Fig. 3.7, the third subplot in Fig. 3.8 also clearly shows the vortex-induced downwash that the receiver experiences when it is at the contact position. The magnitude of the downwash is 4 m/s at the first two contact positions and 3 m/s at the last two contact positions. From the first subplot of Fig. 3.8, it can be seen that during the time of the first two contact passes, the aircraft were exposed to tailwind (wind in the positive x-direction is tailwind) and during the last two contact passes, the aircraft were exposed to headwind. As depicted in Fig. 3.11,
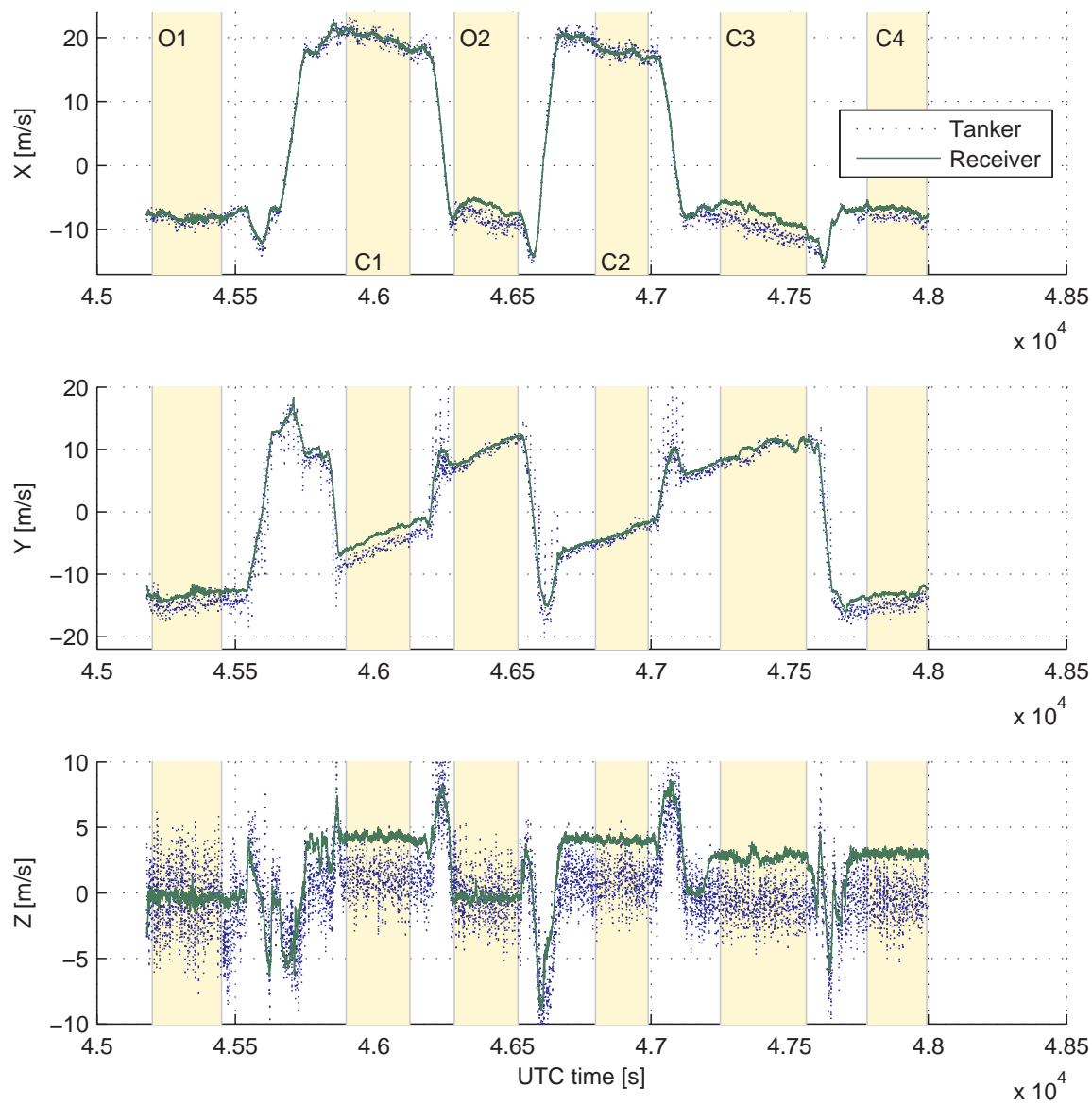
Figure 3.8. Wind components in the receiver body frame.
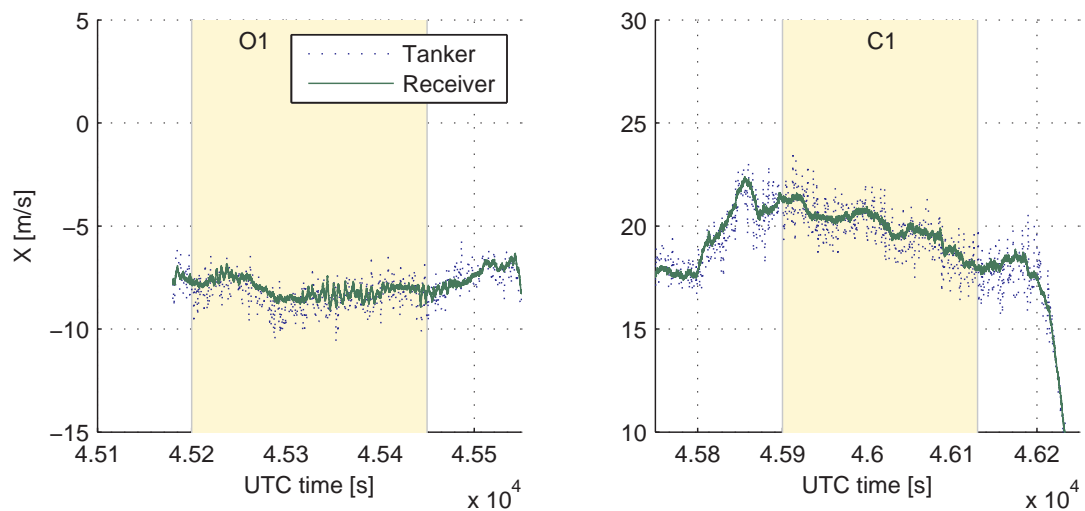
Figure 3.9. Detail view of x-component of winds in Fig. 3.8.
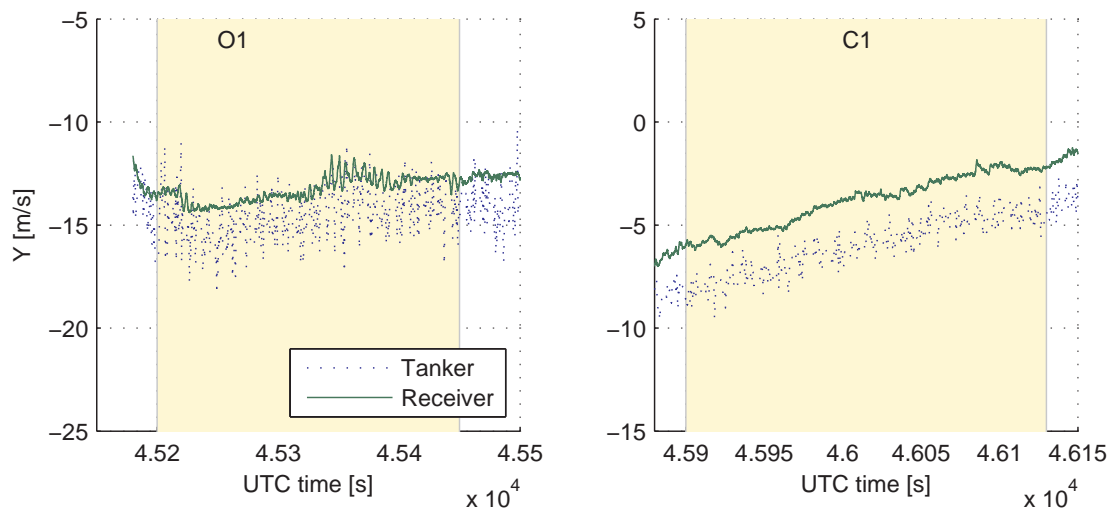
Figure 3.10. Detail view of y-component of winds in Fig. 3.8.

with a positive pitch angle, tailwind resolved in the body frame has a component in positive z-axis while headwind has a component in negative z-axis. The wind that the receiver experiences is the sum of the prevailing wind and the vortex-induced wind. Thus, the prevailing tailwind increases the downwash effect while prevailing headwind reduces it.
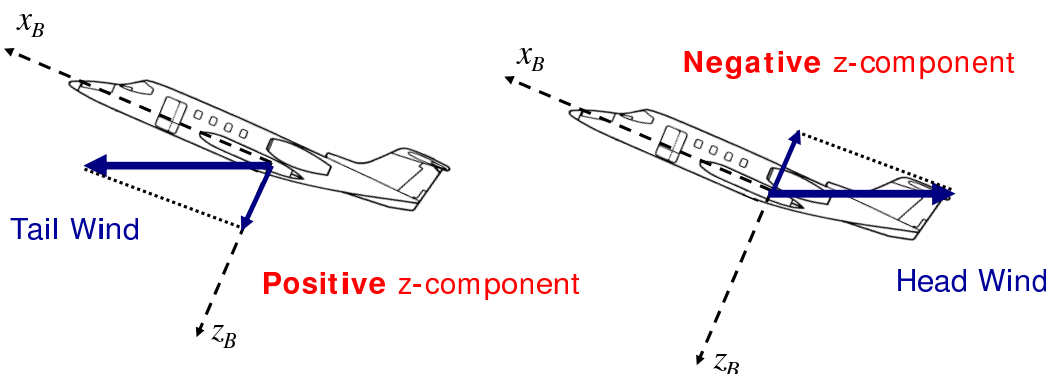
Figure 3.11. Component of tailwind and headwind in body z-axis.

3.5 Power Spectral Analysis of the Receiver Wind

In this section, an analysis is carried out on the frequency content of the components of the receiver wind through the Power Spectral Density (PSD) functions. This analysis is motivated by the fact that stochastic content of the atmospheric wind, i.e. turbulence, is commonly modeled by PSD functions [2,39]. The mean variation of the receiver wind is attributed to the variations in prevailing wind and vortex-induced wind, both modeled as deterministic quantities. Thus, power spectral analysis is conducted on each wind component after subtracting the corresponding mean variation from the original signal.

The mean variation of each wind component is calculated using a non-causal moving-window averaging filter

$$W_{mean}(k) = \frac{1}{2n+1} \sum_{i=k-n}^{k+n} W(i) \tag{3.8}$$

where $2n + 1$ is the window size and k is the discrete time index. The non-causal filter is used to avoid introducing delay into the signal. The PSD function of each wind component is based on the corresponding zero mean signal, $W(k) - W_{mean}(k)$. For the estimation of PSD functions, the Welch method is used as described in 2.5. Recall that there are two observation passes and four contact passes. Thus, for each component of the wind, two different PSD functions are computed: (i) based on two observation passes, and (ii) based on four contact passes. A PSD function is calculated for each of the two observation passes and then the average of the two PSD functions is called the observation PSD. Similarly, the four contact PSD functions are averaged and called the contact PSD.

As discussed earlier, there is a choice between calculating the receiver wind at 100 Hz or 20 Hz. Calculation at 100 Hz requires upsampling (V, β, α) from 20 to 100 Hz, while calculation at 20 Hz requires downsampling GPS/IMU velocity and Euler angles from 100 Hz to 20 Hz. Figure 3.12 shows the PSD of the x-component of the receiver wind for both the 100 and 20 Hz calculations. Note the Nyquist frequency of sampled data is half the sampling frequency. Thus, for the 20 Hz data, the PSD function can only be calculated up to 10 Hz. The segments of the plot from 10 to 30 Hz are the aliasing of the PSD function in the -10 to 10 Hz frequency range. Note the 100 Hz PSD function matches the 20 Hz PSD function until 10 Hz, after which it falls off rapidly. This is because the original 20 Hz signals, although upsampled to 100 Hz, are still limited in their authentic spectral content to 10 Hz. Thus, the consistency of a PSD function of an output signal is limited to one-half the lowest
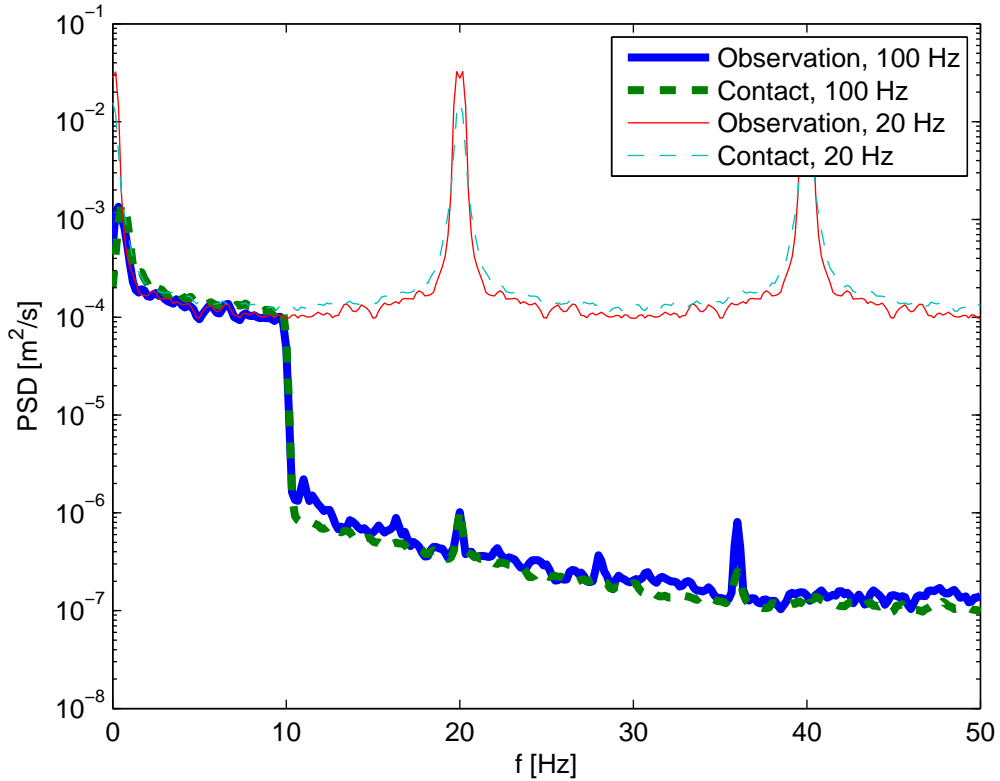
Figure 3.12. PSD functions of the x-component of the receiver wind. Comparison between 100 Hz and 20 Hz calculations.

sampling frequency of the input signals. For this reason, the wind calculation is carried out at 20 Hz hereafter.

Figure 3.13 shows the two PSD functions for the x-, y-, and z-components of the wind. Note that the PSD functions are plotted for the frequency up to 10 Hz, due to the Nyquist frequency at 10 Hz. The wind data show slightly more energy at the contact position than that at the observation position. However, the difference is so small that it is considered insignificant. Therefore we conclude that the stochastic content of the receiver wind is not influenced in a noticeable way by the wake vortices.
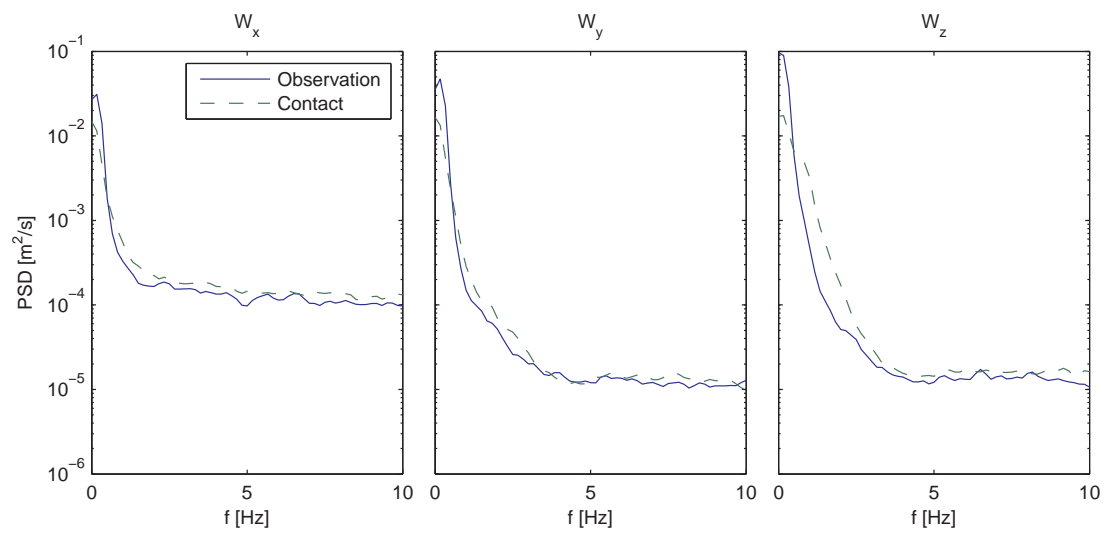
Figure 3.13. PSD functions of receiver wind components. Comparison between observation and contact.

CHAPTER 4

WIND EFFECT MODELING TECHNIQUE

During aerial refueling, the wind experienced by the aircraft can be divided into three components. Both the tanker and receiver aircraft are subject to the same prevailing wind present during the flight. Further, both aircraft experience turbulence along with the prevailing wind. In addition to prevailing wind and turbulence, the wind experienced by the receiver is also contributed to by the tankers wake vortex. The total wind experienced by the tanker is assumed to be the superposition of the prevailing wind and turbulence, while the wind that the receiver is subject to is modeled as the superposition of prevailing wind, turbulence, and vortex-induced wind. This leads to a wind model taking the form of a slowly changing mean component representing prevailing wind and tanker vortex, superimposed with a high frequency random process representing turbulence. This wind model is common in the study and simulation of aircraft flight dynamics and control [40]. This section presents the methods used to model each wind component. This wind effect modeling technique will be used to simulate the test flight, discussed in Chapter 5.

4.1 Prevailing Wind Calculation

Since one objective of this work is to simulate the test flight, the prevailing wind that the aircraft will be subjected to in the simulation should be the same as that experienced in the actual test flight. The wind experienced by the tanker and receiver are separately computed from the flight data in Section 3.4. Since the wind computed from the receiver flight data may include the effect of the tanker's wake

vortex, the wind computed from the tanker flight data is used for the calculation of the prevailing wind. Further, the wind computed from the flight data may include the effect of turbulence and measurement noise. Thus, the prevailing wind is modeled as the deterministic mean variation of the wind computed from the tanker flight data. The components of the prevailing wind in the inertial frame (north-east-down) are the mean variation of the components of the tanker wind in the same inertial frame. The mean variations are determined using the non-causal moving-window averaging filter, formulated in Eq. (3.8). Figure 4.1 shows the mean value of the tanker wind along the corresponding unfiltered wind as computed from the flight data.

In addition to the wind, the equations of motion used in the simulation include terms with the time derivative of the wind. Thus, the time derivative of the prevailing wind is computed by the slope of the mean variation of the tanker wind. A first order approximation is used to compute the slope from the mean variation of the wind components as

$$\widehat{\dot{W}}(k) = \left[W_{mean}(k) - W_{mean}(k-1)\right]/\Delta t \tag{4.1}$$

where $W_{mean}(k)$ and $W_{mean}(k-1)$ are computed by Eq. (3.8) at the kth and the previous steps, respectively; Δt is the sampling period of the non-causal filter. To remove the high-frequency content, the slopes computed in Eq. (4.1) are filtered through the same noncausal filter once more. Figure 4.2 shows slopes as computed by Eq. (4.1) and their mean values after the second filtering.
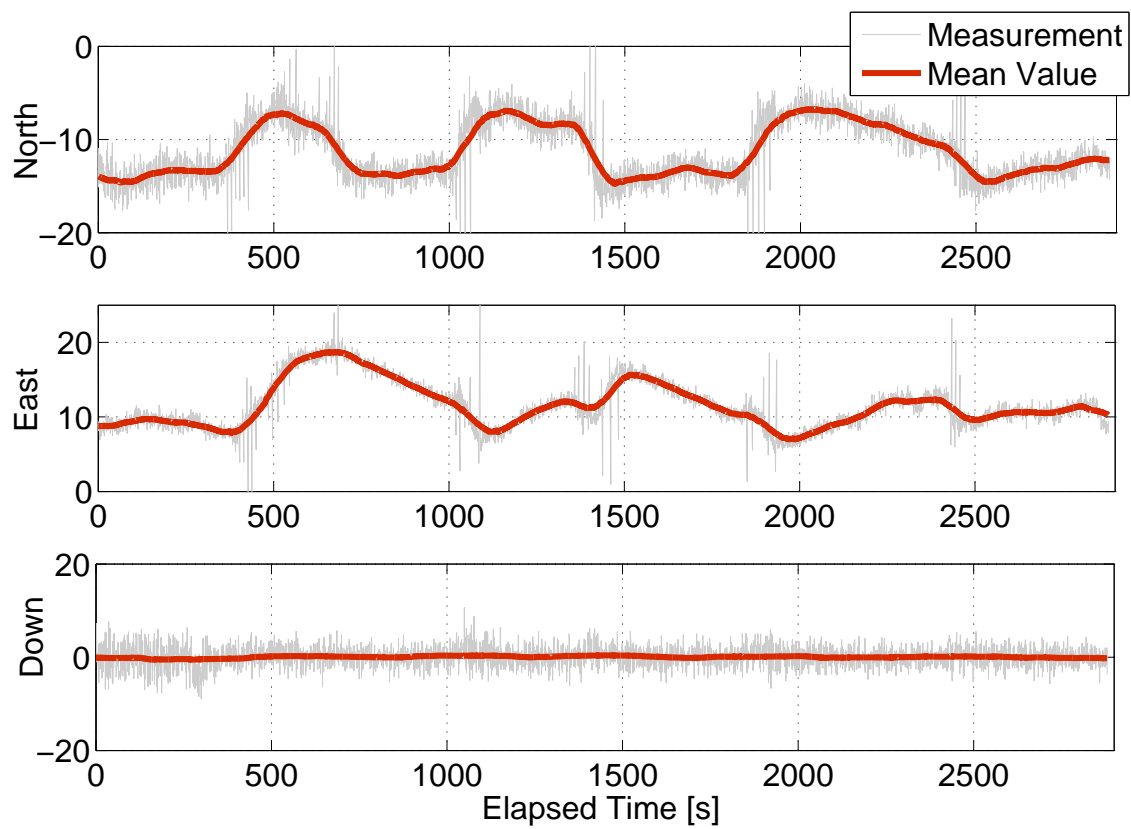
Figure 4.1. The components of tanker wind in inertial frame [m/s].
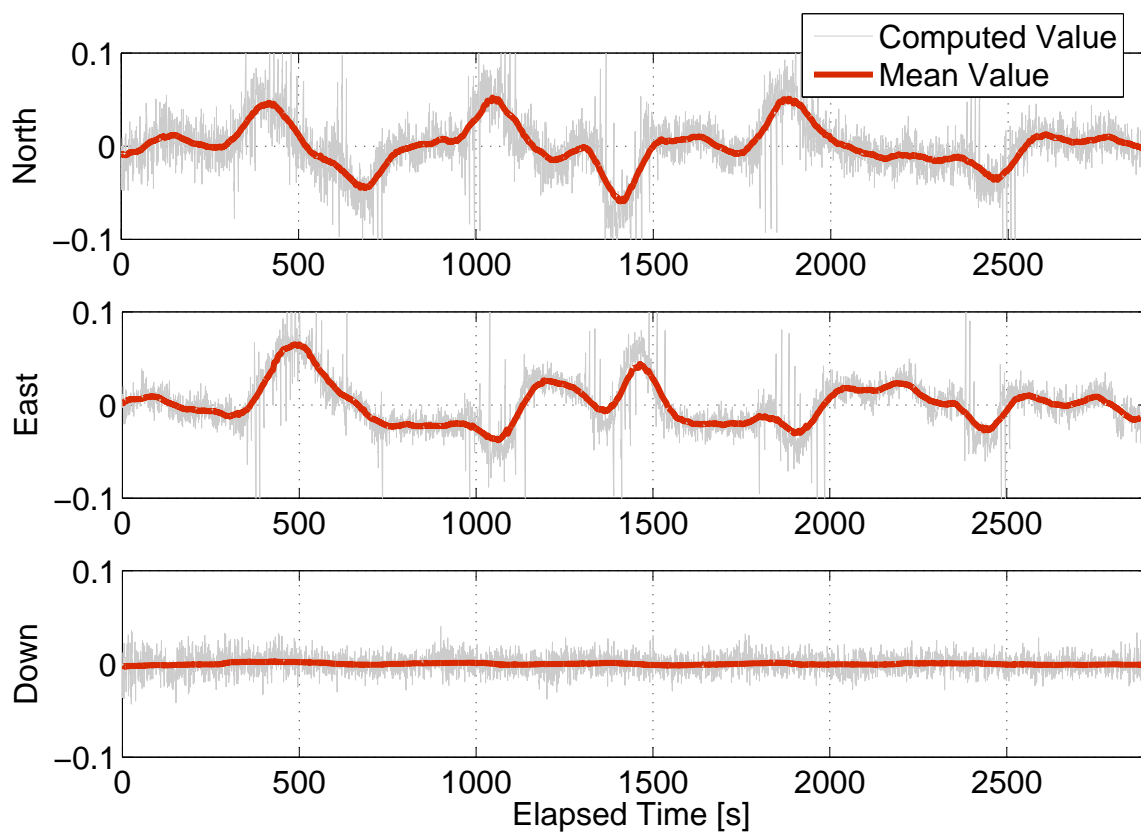
Figure 4.2. Derivative of the tanker wind in the inertial frame [m/s^2].

4.2   Wake Vortex Induced Wind Modeling

Using lifting line theory [41], the wing and the horizontal tail of the tanker aircraft are modeled as horseshoe vortices as depicted in Fig. 4.3. The part of the vortex sheet along the span of the wing or horizontal tail is the bound vortex while the parts that continue in the downstream direction are the trailing or tip vortices [41]. The half length of a bound vortex, which also determines the origins of the trailing vortices on each side, is $\pi/4$ times the physical half span. As depicted in Fig. 4.3, wing vortices rotate inward as the wing generates positive lift and tail vortices rotate outward as the horizontal tail generates negative lift. The wing vortices are much stronger than the tail vortices as the wing generates more lift; e.g. about 34 times more lift by the wings of the tanker in the AAR flight condition. The tip vortices are always aligned with the downstream direction, i.e. the air velocity vector. This implies that the tip vortices rotate relative to the body frame of the tanker as the angle of attack and sideslip angle change. The inclusion of the bound vortex is new in this thesis; the previous development of this vortex effect modeling technique (VEMT) [21] included only the trailing vortices. The addition of the bound vortex improves the agreement of the simulation results with the observations from the flight data, described in Chapter 5.

The Biot-Savart law [42] along with the modified Helmholtz horseshoe vortex model [21] compute the magnitude of the wind induced by each filament at a given point as

$$W_r = \frac{\Gamma \, r}{2 \, \pi \, (r^2 + r_c^2)} \left[1 - \exp\left(-\frac{r^2}{4 \, \upsilon \, \tau} \right) \right] \tag{4.2}$$

where Γ is the vortex strength, r is the radial distance from the point to the filament (see Fig. 4.4), r_c is the radius of the vortex core, υ is the viscosity parameter specified as $0.06 \times \Gamma$ [21], and τ is the vortex age specified as the distance to the vortex filament
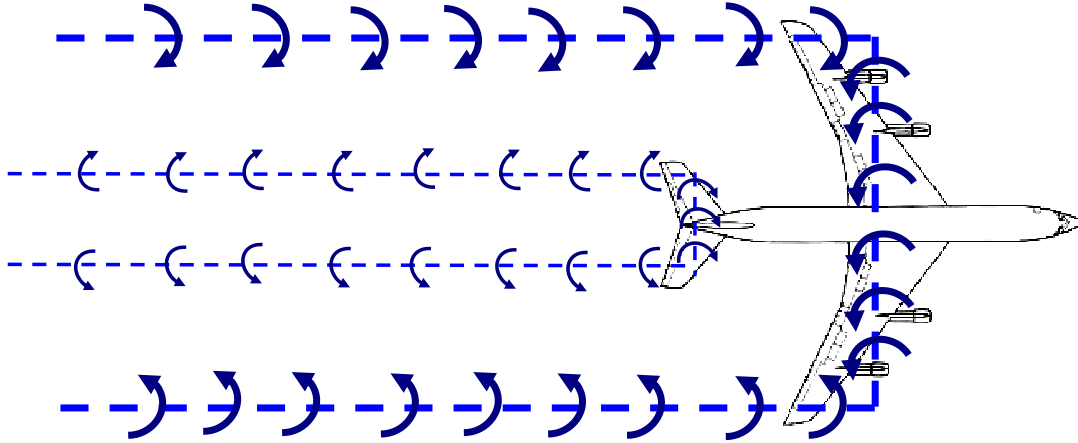
Figure 4.3. Depiction of horseshoe vortices for wing and horizontal tail.

divided by the speed of the tanker [21]. The strength of a vortex filament, including the effect of finite length is [21, 42]

$$\Gamma = \frac{L}{\rho \, V \, (\pi/4) \, b} \frac{\cos \gamma_1 + \cos \gamma_2}{2} \tag{4.3}$$

where L is the lift generated by the wing or tail, ρ is the air density, V is the airspeed of the tanker, b is the span of the wing or tail, and γ_1 and γ_2 are angles as depicted in Fig. 4.4. Note that γ_1 and γ_2 are always nonzero for bound vortices while γ_1 or γ_2 is zero for tip vortices as tip vortices are modeled to be semi-infinite. Note that there are six vortex filaments: a wing bound vortex, two wing tip vortices, a tail bound vortex and two tail tip vortices. The velocity of the wind induced by the wake vortex of the tanker at a given point is the vectorial sum of the wind vectors due to all six vortex filaments.

As the point of interest moves behind the tanker, the vector sum yields a wind velocity vector of different magnitude and direction. Figure 4.5 illustrates an example of how the induced wind at the origin of the body frame varies as the the receiver laterally traverses the tanker's wake. During the lateral move, the receiver is 35.5 m
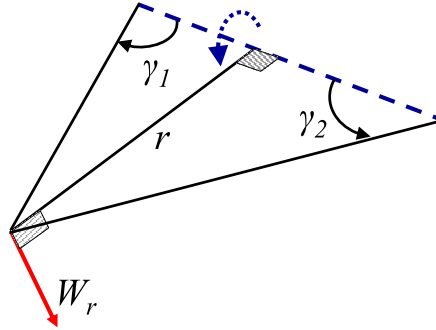
Figure 4.4. Wind induced by a filament, normal to the radial direction.

behind and 8.5 m below the tanker (note that the tanker has a wingspan of 39.9 m). The three plots in the figure show the components of the wind vector in the body frame of the receiver with the maximum values given in m/s.

Figure 4.5 also shows that the receiver aircraft may have a significant wind gradient over its span/length/height depending on its position relative to the tanker. Reference [21] introduced a technique for modeling the effect of a nonuniform wind distribution on the dynamics of an aircraft. Using this technique, a nonuniform wind distribution over an aircraft is approximated by a uniform wind component and a uniform wind gradient. Figure 4.6 depicts the approach applied to a nonuniform distribution along the y-axis of the body frame of the wind component in the body z-direction. As depicted in Fig. 4.6, the nonuniform $W_z(y)$ is approximated by the effective wind $(W_z)_{eff}$ and effective wind gradient $(\partial W_z/\partial y)_{eff}$. The same approach is used for all three components of the wind distribution along the three axes of the body frame of the aircraft. This leads to three components of effective translational
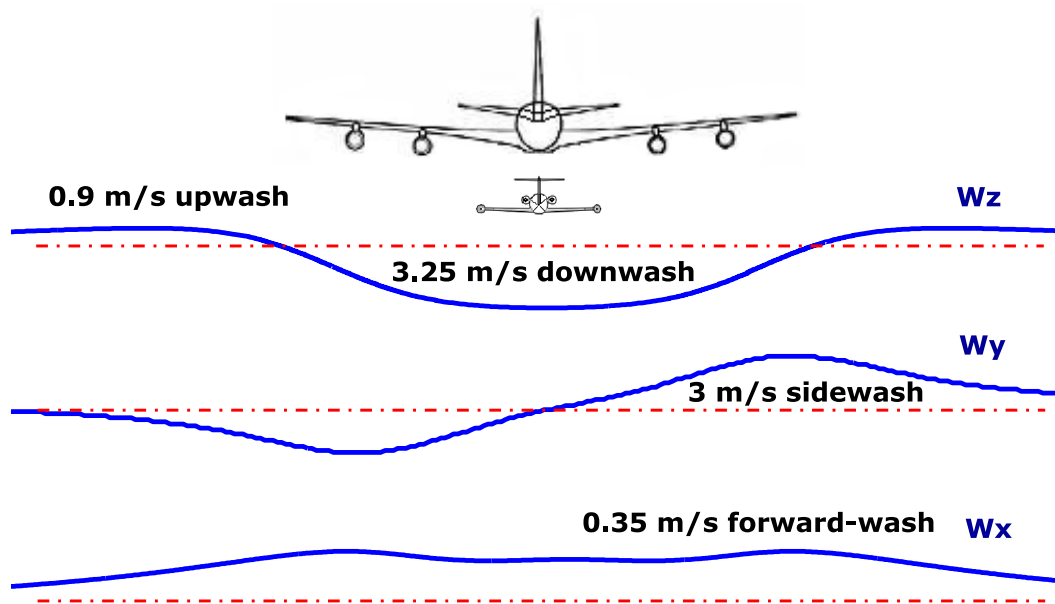
Figure 4.5. An example of the nonuniform wind distribution behind the tanker aircraft.
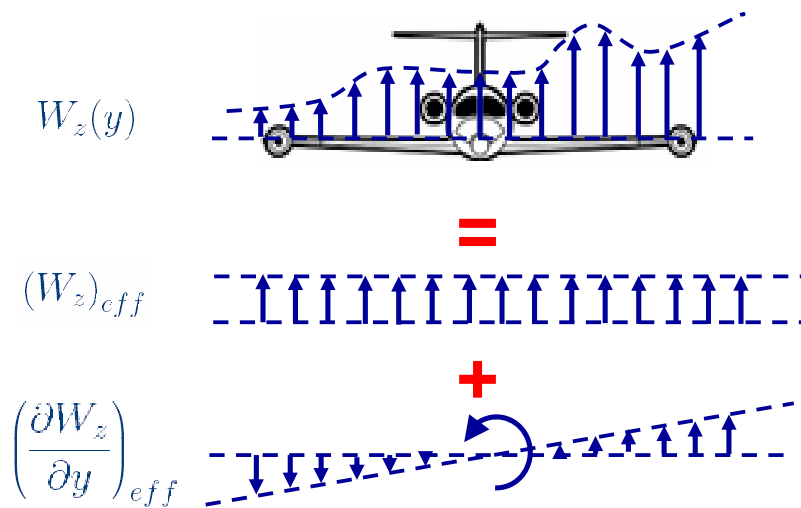
Figure 4.6. Nonuniform wind distribution approximated by uniform wind and wind gradient.

wind velocity and three components of effective rotational wind velocity. The effective rotational wind components are computed as

$$p_{eff} = \left(\frac{\partial W_z}{\partial y}\right)_{eff} - \left(\frac{\partial W_y}{\partial z}\right)_{eff} \tag{4.4}$$

$$q_{eff} = \left(\frac{\partial W_x}{\partial z}\right)_{eff} - \left(\frac{\partial W_z}{\partial x}\right)_{eff} \tag{4.5}$$

$$r_{eff} = \left(\frac{\partial W_y}{\partial x}\right)_{eff} - \left(\frac{\partial W_x}{\partial y}\right)_{eff} \tag{4.6}$$

4.3   Turbulence Modeling

Two methods of representing turbulence in a flight simulation are (i) a random velocity disturbance generated by filtered white noise shaped to a specific power spectrum, and (ii) the use of natural turbulence recorded in wind tunnels or in the atmosphere [40]. Both of these methods are employed and compared in the simulation of the test flight. In the following discussion, u_g, v_g, and w_g refer to the three components of the translational velocity turbulence and p_g, q_g, and r_g refer to the three components of the angular velocity turbulence.

4.3.1   Dryden Turbulence Model

The stochastic turbulence component is commonly treated as a frozen field, zero mean, wide-sense stationary random process [40]. The frozen field assumption is that the turbulence disturbance field does not change during the space and time of the aircraft's passage through the area. Much of the complexity of a multidimensional random process such as turbulence is simplified in this description.

As recommended in the military flying qualities specification [2,39], the Dryden model PSD functions are used to model turbulence as a random process. The Dryden

form of the spectra for the translational turbulence velocity components in the body frame of the aircraft is [2]

$$\Phi_{u_g}(\Omega) \;=\; \sigma_u^2 \frac{2L_u}{\pi} \frac{1}{1+(L_u\Omega)^2} \tag{4.7}$$

$$\Phi_{v_g}(\Omega) \;=\; \sigma_v^2 \frac{L_v}{\pi} \frac{1+3(L_v\Omega)^2}{[1+(L_v\Omega)^2]^2} \tag{4.8}$$

$$\Phi_{w_g}(\Omega) \;=\; \sigma_w^2 \frac{L_w}{\pi} \frac{1+3(L_w\Omega)^2}{[1+(L_w\Omega)^2]^2} \tag{4.9}$$

where Ω is the spatial frequency in rad/m, σ_u, σ_v, σ_w are known as the RMS turbulence intensities and are a measure of the intensity of the turbulence, and L_u, L_v, L_w are the scale lengths. The spectra for the angular velocity disturbance components in the body frame due to turbulence are [2]

$$\Phi_{p_g}(\Omega) \;=\; \frac{\sigma_w^2}{L_w} \frac{0.8(\pi L_w/4b)^{1/3}}{1+(4b\Omega/\pi)^2} \tag{4.10}$$

$$\Phi_{q_g}(\Omega) \;=\; \frac{\Omega^2}{1+(4b\Omega/\pi)^2}\, \Phi_{w_g}(\Omega) \tag{4.11}$$

$$\Phi_{r_g}(\Omega) \;=\; \frac{\Omega^2}{1+(3b\Omega/\pi)^2}\, \Phi_{v_g}(\Omega) \tag{4.12}$$

Reference [2] recommends the assumption of isotropy for turbulence above 20,000 ft, i.e.,

$$\sigma_u = \sigma_v = \sigma_v \tag{4.13a}$$

$$L_u = L_v = L_w \tag{4.13b}$$

In the MATLAB/Simulink implementation of the Dryden turbulence model, Monte Carlo simulation [43] is used, i.e. Gaussian white noise, with unity spectral density, is input to a linear filter. Spectral factorization [44] is used to obtain the transfer functions and then state-space representations of the linear filters that yield signals with the Dryden power spectral densities. This procedure is shown in Appendix B for u_g and v_g. The other components follow a similar derivation.

The state-space representations of the filter to generate the x-component of the translational velocity of turbulence is

$$\dot{u}_g = -\frac{V}{L_u}u_g + \sigma_u\sqrt{\frac{2V}{L_u\pi}}\,\eta \tag{4.14}$$

For the y- and z-components, the state-space representation has the same form as

$$\begin{bmatrix} \dot{x}_1 \\ \dot{x}_2 \end{bmatrix} = \begin{bmatrix} 0 & 1 \\ -\dfrac{V^2}{L^2} & -\dfrac{2V}{L} \end{bmatrix} \begin{bmatrix} x_1 \\ x_2 \end{bmatrix} + \begin{bmatrix} 0 \\ \dfrac{V^2}{L^2} \end{bmatrix}\eta \tag{4.15a}$$

$$\{v_g, w_g\} = \sigma\sqrt{\frac{L}{\pi V}}\left(x_1 + \sqrt{3}\frac{L}{V}x_2\right) \tag{4.15b}$$

where $\sigma = \sigma_v$ and $L = L_v$ for v_g and $\sigma = \sigma_w$ and $L = L_w$ for w_g. For the turbulence angular velocity component around the x-axis, the state-space equation is

$$\dot{p}_g = \frac{\pi V}{4b}\left[-p_g + \frac{\sigma_w}{L_w^{1/3}}\sqrt{\frac{0.8}{V}}\left(\frac{\pi}{4b}\right)^{1/6}\eta\right] \tag{4.16}$$

where b is the wingspan of the aircraft. For the turbulence angular velocity components around the y- and z-axes, a state-space representation of the same form is used

$$\begin{bmatrix} \dot{x}_1 \\ \dot{x}_2 \\ \dot{x}_3 \end{bmatrix} = \begin{bmatrix} 0 & 1 & 0 \\ 0 & 0 & 1 \\ -\dfrac{\pi V^3}{L^2 ab} & -\dfrac{\pi V^2}{L^2 ab}\left(\dfrac{ab}{\pi}+2L\right) & -\dfrac{\pi V}{Lab}\left(\dfrac{2ab}{\pi}+L\right) \end{bmatrix} \begin{bmatrix} x_1 \\ x_2 \\ x_3 \end{bmatrix} + \begin{bmatrix} 0 \\ 0 \\ \dfrac{\pi V^3}{L^2 ab} \end{bmatrix}\eta \tag{4.17a}$$

$$\{q_g, r_g\} = \sigma\sqrt{\frac{L}{\pi V^3}}\left(x_2 + \sqrt{3}\frac{L}{V}x_3\right) \tag{4.17b}$$

where $\sigma = \sigma_w$, $L = L_w$ and $a = 4$ for q_g, and $\sigma = \sigma_v$, $L = L_v$ and $a = 3$ for r_g. In all the state-space equations above, η is the zero mean, bandlimited, Gaussian white noise with unity flat power spectral density, obtained in the simulations from a band-limited white noise generator. Reference [2] states that u_g, v_g, w_g and p_g shall be considered mutually independent (uncorrelated) in a statistical sense while q_g is

correlated with w_g and r_g is correlated with v_g. This is modeled in the simulation by using different seeds for the white noise generators of u_g, v_g, w_g and p_g while the seed of q_g is equal to that of w_g and the seed of r_g is equal to that of v_g.

In order to use the Dryden turbulence model to simulate the turbulence experienced by the tanker and receiver during the test flight, it is necessary to identify the Dryden model parameters from the flight data. There are six parameters that can be varied among the translational and rotational turbulence PSD functions $(\sigma_u, \sigma_v, \sigma_w, L_u, L_v, L_w)$. To identify these parameters, the six parameters are varied to minimize the logarithmic least squares error, in the frequency range of 0 to 10 Hz, between the Dryden PSD functions and the PSD of the flight data turbulence (Fig. 3.13), according to the objective

$$\min_{\sigma, L} \sum_f \left[(\log \phi_{u\text{Dry}} - \log \phi_u)^2 + (\log \phi_{v\text{Dry}} - \log \phi_v)^2 + (\log \phi_{w\text{Dry}} - \log \phi_w)^2 \right] \quad (4.18)$$

where log is the base-10 logarithm.

The logarithmic least squares approach is taken in order to provide equal weight to the fit of the PSD over the whole frequency range, since the magnitude of the PSD function is a very small number at frequencies greater than about 0.5 Hz.

Parameter identification is performed under four sets of constraints on σ and L. The cases are summarized in Table 4.1. For the first three cases, the isotropic constraint is observed (Eq. (4.13)). In case 1, L is fixed at 533.4 m, the value recommended by MIL-F-8785C [2], and σ is allowed to vary. In case 2, L varies while σ is fixed at 0.1 m/s, a representative value chosen for "light turbulence." In case 3, both σ and L are allowed to vary. Finally, in case 4, the isotropic constraint is removed, and all σ and L are are allowed to vary independently. The results of the parameter identification are shown in Table 4.2.

Table 4.1. Dryden model parameter cases.

Case 1	σ and L isotropic	σ varies, L fixed at 533.4 m
Case 2	σ and L isotropic	σ fixed at 0.1 m/s, L varies
Case 3	σ and L isotropic	σ and L both allowed to vary
Case 4	No isotropic constraint	All σ and L allowed to vary independently

Table 4.2. Dryden model parameters from the logarithmic least squares fit. σ [m/s], L [m].

Case	σ_u	σ_v	σ_w	L_u	L_v	L_w
1	0.39	0.39	0.39	533.4	533.4	533.4
2	0.11	0.11	0.11	43.36	43.36	43.36
3	0.29	0.29	0.29	283.5	283.5	283.5
4	0.20	0.21	0.28	18.49	483.5	597.6

Despite the large variations in the identified L, all of the sets of parameters in Table 4.2 produce similarly shaped PSD curves, differing mostly in the frequency range below 1 Hz. As a result, σ and L of case 1 are used in the rest of the analysis in this thesis because this is the value of L as recommended in MIL-F-8785C [2]. Figure 4.7 shows the resulting case 1 Dryden model PSD function and the receiver wind PSD, previously shown in Fig. 3.13. Note that the flight data PSD shown in Fig. 4.7 is the average between the observation and contact position PSD in Fig. 3.13. The turbulence level identified in case 1 is classified as "light turbulence," marked on Fig. 4.8, reproduced from [2]. This is because $\sigma = 0.39$ m/s (1.3 ft/s) at an altitude of 7000 m (20,000 ft) lies close to the "light" turbulence curve. This result is also consistent with what the pilots reported in the test flight.
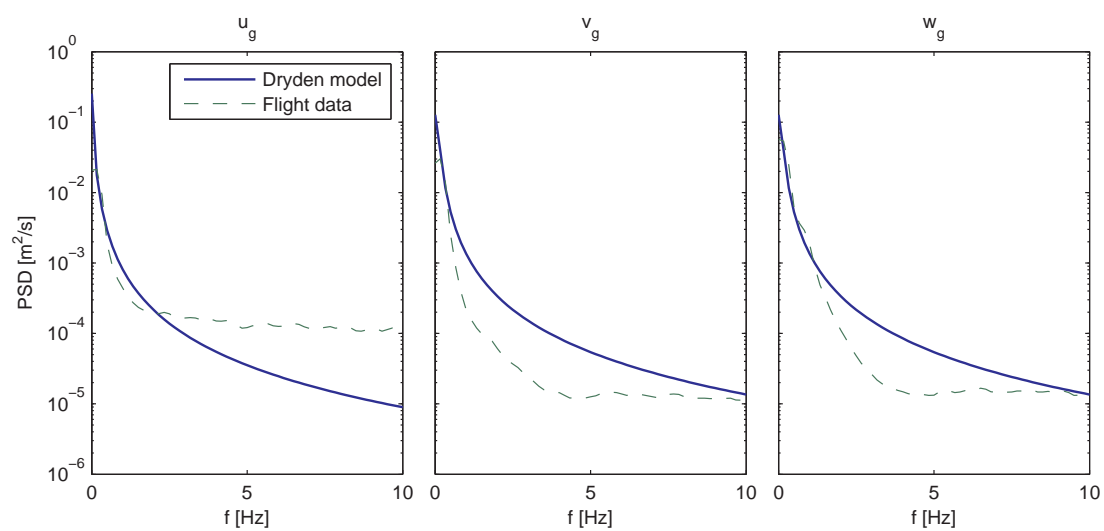
Figure 4.7. Dryden model and flight data PSDs of the receiver wind.
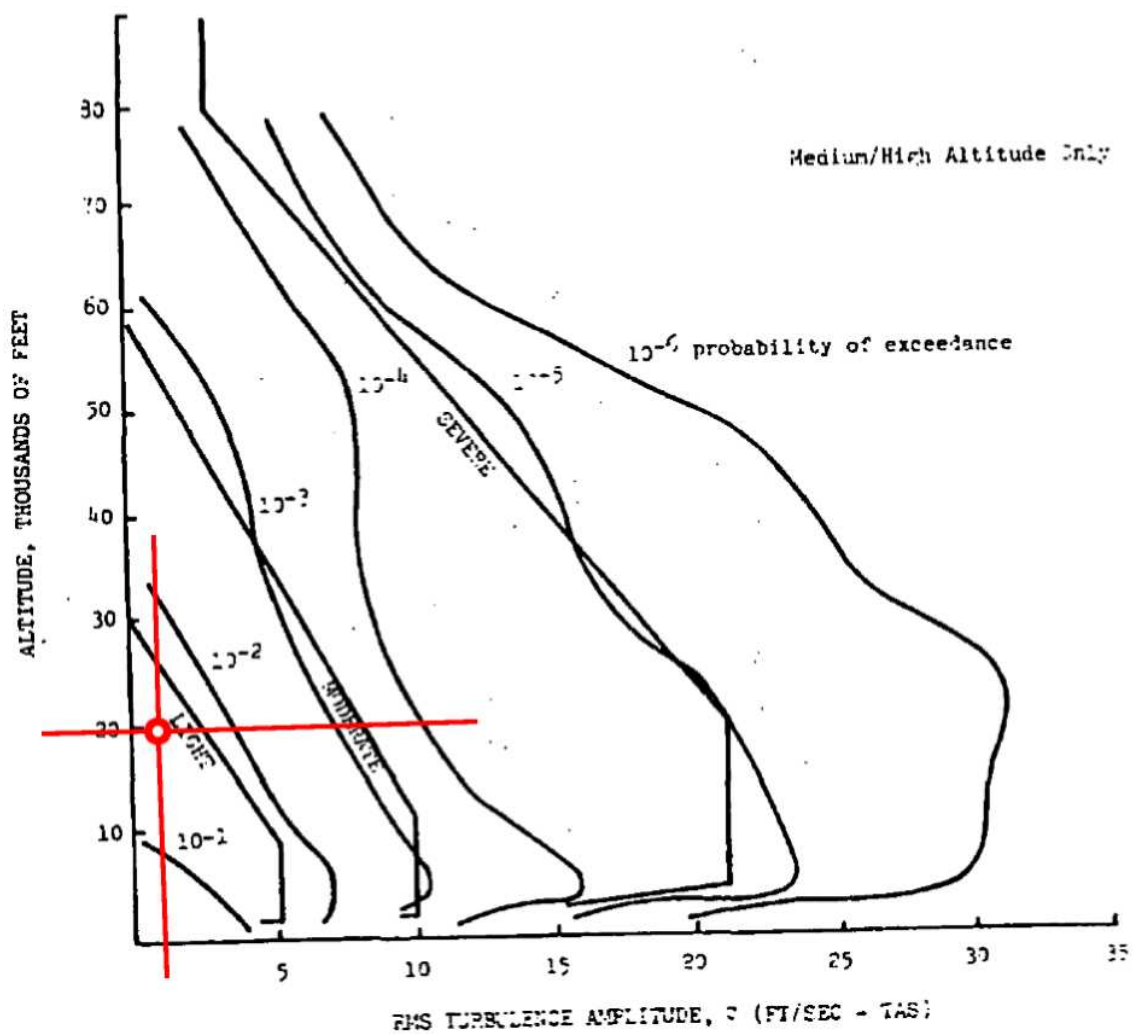
Figure 4.8. Turbulence intensity vs. altitude for given turbulence classifications. Reproduced from [2]. The red circle and crosshairs in the lower left mark the location of σ from Dryden turbulence case 1.

4.3.2 Use of Turbulence Data from Test Flight

As an alternative to the Dryden turbulence model, the turbulence can be extracted from the wind experienced by the receiver in the test flight. The receiver wind body frame components, calculated in Section 3.4 and shown in Fig. 3.8, are used as the basis for the flight data turbulence. By subtracting the moving average, as described in Section 3.5, the zero mean stochastic portion of the wind can be used directly in the simulation, in place of u_g, v_g, and w_g calculated by the Dryden model in the previous section. The turbulence extracted from the flight data will hereafter be referred to as "flight data turbulence." This approach has the advantage that it results from physical measurements and therefore should be the best representation of the actual turbulence experienced during the test flight. However, the turbulence recorded on any particular day may not be "universal" enough to apply to general simulated flights. Additionally, since no attempt was made to measure the angular velocity of the receiver relative to the air, the angular wind velocity cannot be extracted from the flight data. Therefore, there is no source of p_g, q_g, or r_g from the flight data, and so the simulation must operate without angular turbulence components when using the flight data as a turbulence source. The effect of the angular turbulence components will be discussed later.

4.4 Implementation of Wind Effect in 6 DOF Dynamics Equations

The total wind W is incorporated directly into the nonlinear, six degrees of freedom dynamics equations for both aircraft. The equations for the tanker and the receiver used in this simulation are listed in Appendix C, reproduced from Ref. [45]. To illustrate the appearance of W and its time derivative in the dynamics equations, some of the equations for the receiver aircraft are also shown below.

The translational kinematics of the receiver relative to the tanker, in matrix form, is

$$\dot{\xi} = \mathbf{R}_{\mathbf{B_R B_T}}^{\mathbf{T}} \mathbf{R}_{\mathbf{B_R w_R}} \, V_w + \mathbf{R}_{\mathbf{B_R B_T}}^{\mathbf{T}} \, W - \mathbf{R}_{\mathbf{B_T I}} \, \dot{r}_{B_T} + \mathbf{S}(\omega_{\mathbf{B_T}})\xi \qquad (4.19)$$

ξ is the position of the receiver relative to the tanker, expressed in the tanker's frame. $\mathbf{R}_{\mathbf{B_R B_T}}^{\mathbf{T}}$ is the orientation of the receiver relative to the tanker. $\mathbf{R}_{\mathbf{B_T I}}$ is the orientation of the tanker relative to the inertial frame. $\dot{r}_{B_T}$ is the translational velocity of the tanker relative to the inertial frame, expressed in the inertial frame. $\mathbf{S}(\omega_{\mathbf{B_T}})$ is the skew-symmetric matrix constructed by the representation of the angular velocity of the tanker relative to the inertial frame. Note the appearance of W, the representation in the receiver's frame of the total wind experienced by the receiver, due to the prevailing wind, the tanker's wake vortex, and the stochastic turbulence.

The translational dynamics of the receiver, in matrix form, is

$$\begin{bmatrix} \dot{V}_R \\[2mm] \dot{\beta}_R \\[2mm] \dot{\alpha}_R \end{bmatrix} = \mathcal{E}_{\mathbf{R}}^{-1} \left[\mathbf{S}(\omega_{\mathbf{B_R B_T}}) + \mathbf{R}_{\mathbf{B_R B_T}} \mathbf{S}(\omega_{\mathbf{B_T}}) \mathbf{R}_{\mathbf{B_R B_T}}^{\mathbf{T}} \right] \left(\mathbf{R}_{\mathbf{B_R w_R}} \, V_w + W \right)$$

$$- \mathcal{E}_{\mathbf{R}}^{-1} \dot{W} + \frac{1}{m_R} \mathcal{E}_{\mathbf{R}}^{-1} \left(\mathbf{R}_{\mathbf{B_R B_T}} \mathbf{R}_{\mathbf{B_T I}} M_R + \mathbf{R}_{\mathbf{B_R w_R}} \, A_R + P_R \right) \quad (4.20)$$

Note that the wind effect is included in the dynamics through W and $\dot{W}$. Further note that the dynamics is written in terms of V_R, β_R, and α_R (airspeed, sideslip angle, and angle of attack), which are based on the velocity of the receiver relative to the air and thus account for the presence of wind.

The expressions for aerodynamic force and moment coefficients are

$$C_D = C_{D0} + C_{D\alpha}\alpha_R + C_{D\alpha2}\alpha_R^2 + C_{D\delta_e}\delta_e + C_{D\delta_e2}\delta_e^2 + C_{D\delta_s}\delta_s + C_{D\delta_s2}\delta_s^2 \qquad (4.21)$$

$$C_S = C_{S0} + C_{S\beta}\beta_R + C_{S\delta_a}\delta_a + C_{S\delta_r}\delta_r \qquad (4.22)$$

$$C_L = C_{L0} + C_{L\alpha}\alpha_R + C_{L\alpha2}(\alpha_R - \alpha_{ref})^2 + C_{Lq}\frac{c}{2V_R}q_{rel} + C_{L\delta_e}\delta_e + C_{L\delta_s}\delta_s \qquad (4.23)$$

$$C_\mathcal{L} = C_{\mathcal{L}0} + C_{\mathcal{L}\delta_a}\delta_a + C_{\mathcal{L}\delta_r}\delta_r + C_{\mathcal{L}\beta}\beta_R + C_{\mathcal{L}p}\frac{b}{2V_R}p_{rel} + C_{\mathcal{L}r}\frac{b}{2V_R}r_{rel} \qquad (4.24)$$

$$C_\mathcal{M} = C_{\mathcal{M}0} + C_{\mathcal{M}\alpha}\alpha_R + C_{\mathcal{M}\delta_e}\delta_e + C_{\mathcal{M}\delta_s}\delta_s + C_{\mathcal{M}q}\frac{c}{2V_R}q_{rel} \qquad (4.25)$$

$$C_\mathcal{N} = C_{\mathcal{N}0} + C_{\mathcal{N}\delta_a}\delta_a + C_{\mathcal{N}\delta_r}\delta_r + C_{\mathcal{N}\beta}\beta_R + C_{\mathcal{N}p}\frac{b}{2V_R}p_{rel} + C_{\mathcal{N}r}\frac{b}{2V_R}r_{rel} \qquad (4.26)$$

Note the appearance of β_R and α_R in these equations and the fact that standard expressions for the aerodynamic force and moment components include V_R as well. Since V_R, β_R, and α_R already incorporate the effect of wind and wind derivative, the effect of the variation of V_R, β_R, and α_R due to the presence of wind is directly included in the aerodynamic force and moment components. Additionally, the equations include p_{rel}, q_{rel}, and r_{rel}, the angular velocity of the receiver relative to the air. They are computed by

$$\{p, q, r\}_{rel} = \{p, q, r\} - \{p, q, r\}_{eff} \qquad (4.27)$$

where $\{p, q, r\}_{eff}$ are the effective angular velocity of the wind, due to the rotational components of the tanker wake vortex, as computed in Eqs. (4.4)–(4.6), and the stochastic turbulence, as represented in Eqs. (4.16) and (4.17).

CHAPTER 5

SIMULATION AND RESULTS

5.1 Simulation of Test Flight

The 2004–Sept–22 test flight is simulated with a MATLAB/Simulink model that includes tanker and receiver sub-models. The tanker model is a nonlinear 6 DOF model of the KC-135 including wind effects. The tanker controller tracks commanded speed, altitude, and turn rate. Turn rate scheduling is used to simulate the tanker motion from the test flight. The receiver model is a nonlinear 6 DOF model of the Learjet 25, including wind effects. The primary receiver controller, referred to as controller-1, tracks commanded position relative to the tanker. A commanded trajectory generation algorithm is employed, along with the position tracking controller, to simulate the Learjet 25 motion behind the KC-135. The second receiver controller, controller-2, is a speed, altitude, and turn rate tracking controller similar to the tanker's controller. The second controller is used only to generate simulation data for analysis of the controller dynamics on the closed-loop response of the aircraft in terms of acceleration and angular velocity. The controllers employed were developed in [45, 46] and are reproduced in Appendix D.

The simulation is run to recreate the test flight and to obtain data at 20 Hz. To assess the two different turbulence generation methods and to investigate the effect of the controller on the PSD of the closed-loop response, four different simulation cases were run. In each case, a different combination of controller and turbulence source is used. The simulation results are analyzed in the next sections.

51

Table 5.1 summarizes the four simulation cases. Case 1 uses the Dryden model with all turbulence components (translational + rotational), and receiver controller-1. Case 2 uses the Dryden model with only the translational turbulence components, and receiver controller-1. Case 3 uses the same turbulence as case 2, but uses receiver controller-2. Finally, case 4 uses the flight data turbulence source, which is limited to the translational turbulence components only, with the receiver controller-1.

Table 5.1. Simulation cases.

Sim Case	Turbulence Source	Turbulence Components	Receiver Controller
1	Dryden model	$u_g, v_g, w_g, p_g, q_g, r_g$	controller-1
2	Dryden model	u_g, v_g, w_g	controller-1
3	Dryden model	u_g, v_g, w_g	controller-2
4	Flight data	u_g, v_g, w_g	controller-1

Figure 5.1 shows the tanker's trajectory ground track from the flight test and the simulation. Compare Fig. 5.1 with Fig. 3.2 for the reference flight times and segments. Note that in the simulation, the tanker's turns are not as sharp as in the flight test. This is an intentional deviation from the flight test, since the simulated receiver controller cannot maintain the proximity of the commanded position when the tanker makes sharp turns. Since this analysis focuses on the flight segments where the receiver keeps station at the contact and observation positions, the tanker turn radius deviation is an acceptable compromise for the purposes of this thesis. Otherwise, the tanker's overall flight track in the simulation is close to the test flight. In addition, since the prevailing wind used in the simulation is extracted from the test flight data, the prevailing wind in the simulation is the same as in the test flight at the observation and contact segments.
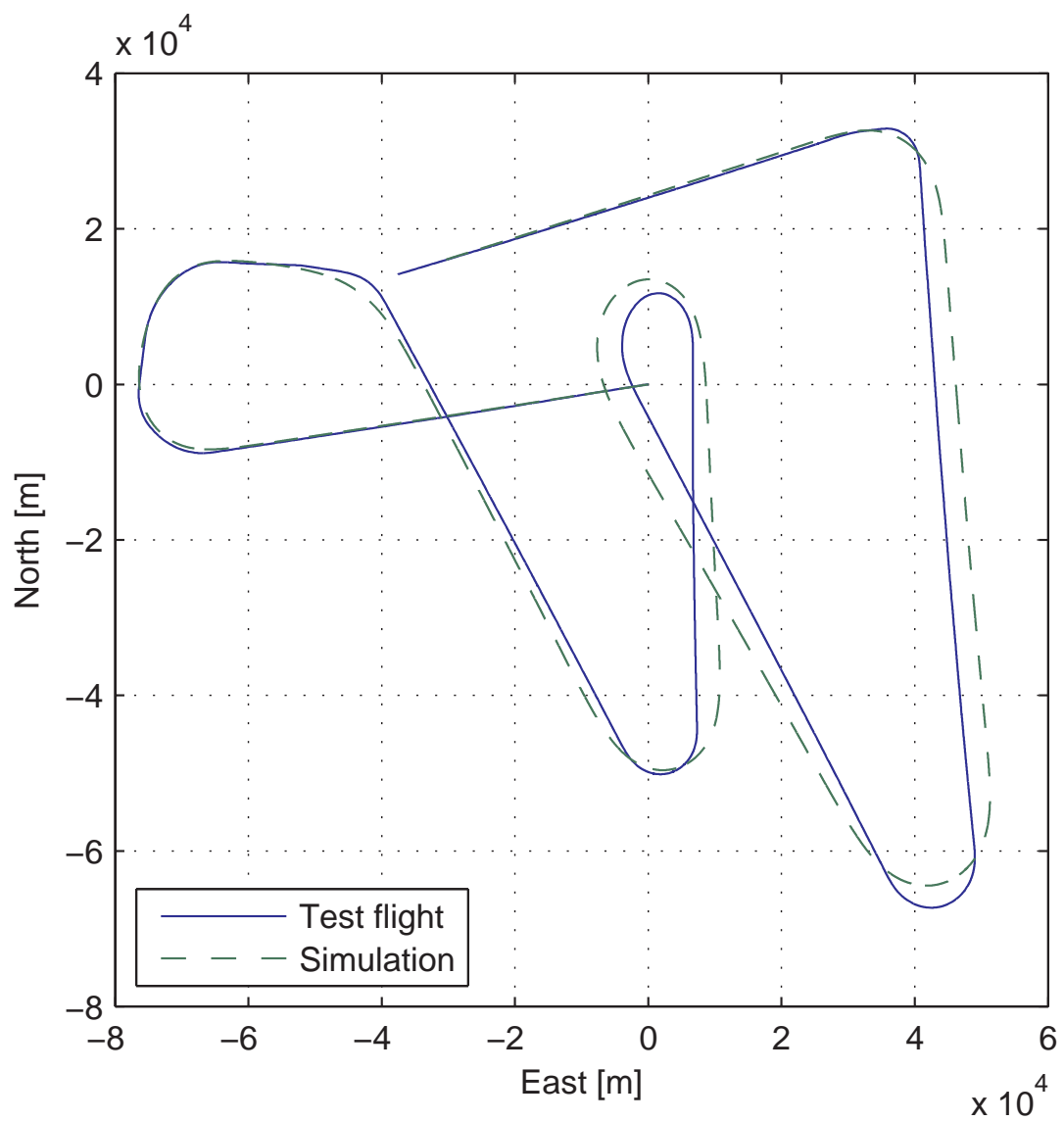
Figure 5.1. Tanker trajectory ground track. Comparison between flight test and simulation.

Figure 5.2 shows the components of the receiver position relative to the tanker from the flight test and simulation case 2. The positions at the contact and observation stations in the simulation are patterned after the actual relative position in the flight test. The maneuver from observation to contact involves three steps: (i) descend to the contact altitude, (ii) move laterally to the position directly behind the tanker, (iii) and then move forward to the final contact position. At the observation position, the receiver in the test flight deviates more from the nominal observation position than does the simulation. The simulation controller-1 performs better station keeping than the human pilot, at both observation and contact. A breakaway maneuver performed in the flight test can be seen between contact-2 and contact-3 in Fig. 5.2, where the receiver descends and falls behind several hundred meters. This maneuver is not performed in the simulation.

5.2 Analysis of Simulation Results and Comparison with Test Flight

In this section, the simulation results are analyzed and subsequently compared to the test flight data. Two modes of investigation are taken: the data are examined (i) in the frequency domain using PSD functions, and (ii) in the time domain by comparing the mean variation of the signals.

5.2.1 Power Spectral Density Analysis

In this section, the PSD function is used to examine the effect of the turbulence model and the controller on the frequency response of the receiver. The simulation PSD is also compared to the flight data PSD in order to evaluate the performance of the simulation with respect to the test flight in the frequency domain. This analysis focuses on the closed-loop response of the receiver. The receiver acceleration and angular velocity are used to characterize the receiver's closed-loop response.

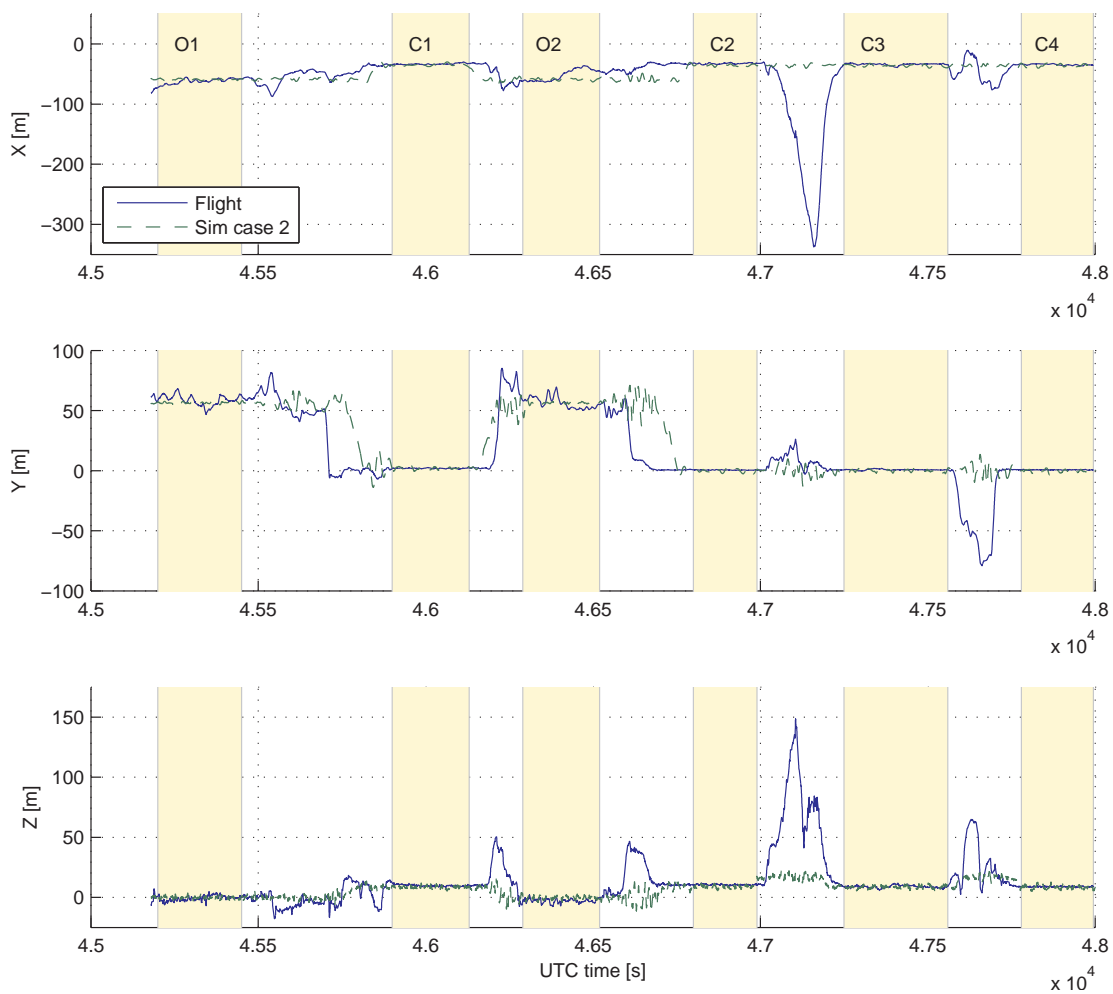Figure 5.2. Tanker-relative position time history from flight data and simulation case 2.

Figure 5.3 shows the PSD functions of the receiver acceleration in the x-direction, a_x, for the observation and the contact position. The difference between observation and contact is negligible for this and the other aircraft state variables. For this reason, in the subsequent results, a PSD function from the simulation results is presented as a single curve, being the average of the observation and contact positions.

The flight data turbulence is limited to the translational components (u_g, v_g, w_g) only. In order to make a direct comparison between the effects of the flight data turbulence and the Dryden model, the Dryden model must similarly be used with only the translational components, i.e., with the rotational components (p_g, q_g, r_g) turned off. Figure 5.4 shows the receiver angular velocity about the x-axis p for simulation cases 1 and 2 (with and without rotational turbulence components from the Dryden model). Part (a) shows the PSD functions for p, and part (b) shows a sample of the time history of p. Both signals are nearly identical, suggesting that the effect of the rotational velocity disturbance components from the Dryden model are very small. The magnitude of p_g, q_g, and r_g is small enough that they can be neglected in the simulation without significant effects. For this reason, all of the subsequent simulation results are from cases without the Dryden rotational turbulence components.

In order to compare the simulation results with the flight data, it is necessary to know the effect of the pilot or controller on the closed loop response of the aircraft. Figures 5.5 and 5.6 show the PSD functions for the receiver acceleration and angular velocity components using the two receiver controllers. In every case, the signals have more total power when the receiver uses controller-1, the controlling the receiver position relative to the tanker. Qualitatively, tracking the commanded position relative to the tanker frame, which is accelerating and rotating, requires more control effort than maintaining altitude and speed. To deliver the required control authority of higher magnitude and frequency, controller-1 injects more energy into the system
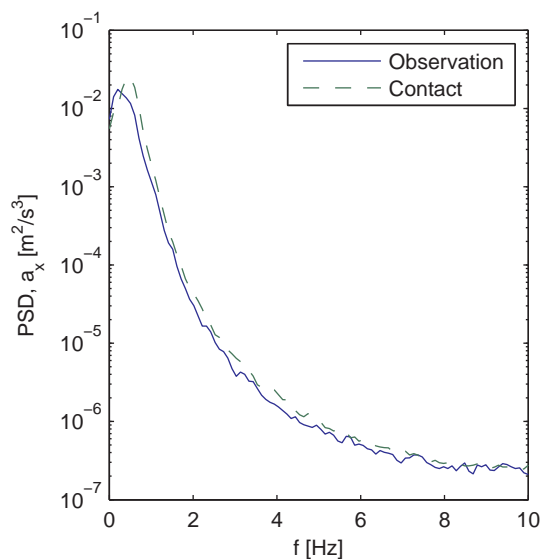
Figure 5.3. PSD functions of the acceleration x-component of the receiver, simulation case 1. Comparison between observation and contact.
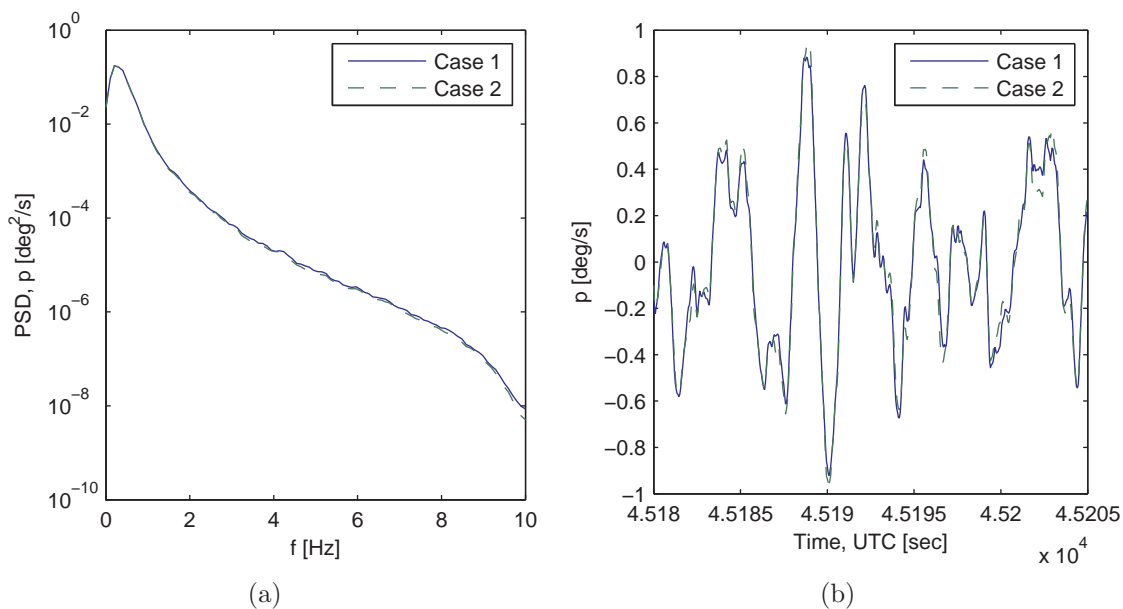
Figure 5.4. Receiver angular velocity component p. Comparison between simulation cases 1 and 2: with and without rotational turbulence from the Dryden model. (a) PSD functions. (b) Example time history.

Figure 5.5. PSD functions of the acceleration components of the receiver. Comparison between two different receiver controllers in the simulation.

Figure 5.6. PSD functions of the angular velocity components of the receiver. Comparison between two different receiver controllers in the simulation.

throughout the whole frequency range, resulting in the power increase in the PSD functions. This leads to an important observation: when examining the response of an aircraft to turbulence, the effect of the controller or pilot cannot be discounted. For this reason, direct comparisons between the frequency contents of flight data and the simulation data are not possible because, while the simulation attempts to model the turbulence in the actual test flight, no effort is made for the controllers in the simulation to represent the dynamic response of the pilot in the test flight.

With the preceding caveats, the simulation results can now be compared with the test flight data in the frequency domain in order to evaluate the simulation's performance. Figures 5.7 and 5.8 show the PSD functions of the receiver acceleration and angular velocity, from the simulation and the test flight. For the simulation curves, results are shown from cases 2 and 4, being with Dryden turbulence and with flight data turbulence, respectively. For the flight test curves, the observation and contact positions are shown. In general, all of the PSD curves rise to a peak value at a very low frequency near 0 Hz, and thereafter decrease until the Nyquist frequency.

In contrast to the simulation result shown in Fig. 5.3, there is a consistent and significant difference between the PSD functions for the observation and contact position in the flight data. There is always more power in the signals at contact compared to observation. By examining Figs. 5.5 and 5.6, the difference in power from observation to contact can be attributed to a change in the pilot's behavior. At the observation position, the pilot is not trying to strictly maintain a specific relative position from the tanker, and therefore his task is less demanding. At contact, the pilot must react and make changes to the aircraft position on a far tighter scale in order to maintain the appropriate position relative to the tanker. Further, the pilot has different visual cues at contact, which may require even more control effort. Therefore, the contact PSD of the aircraft response states is always higher than the
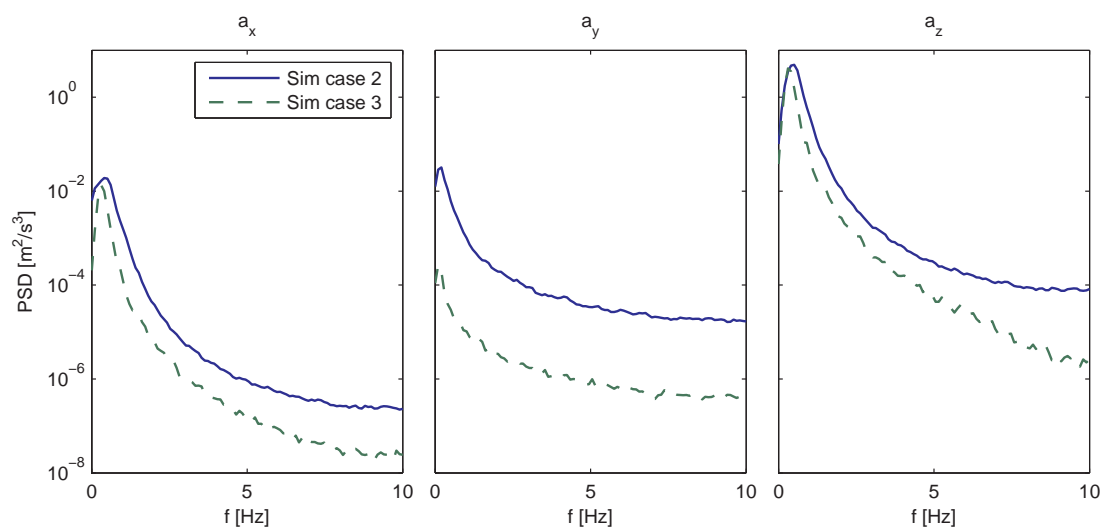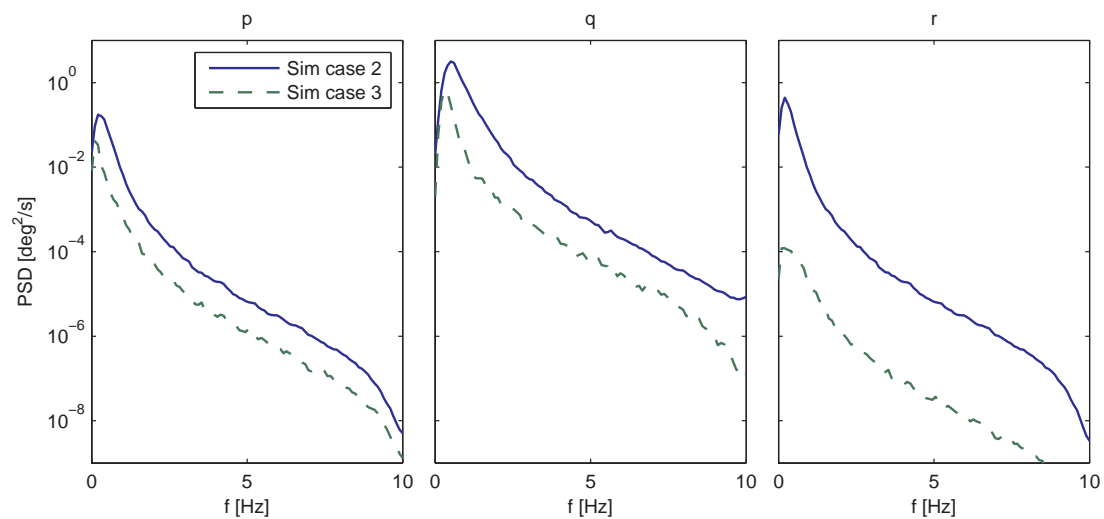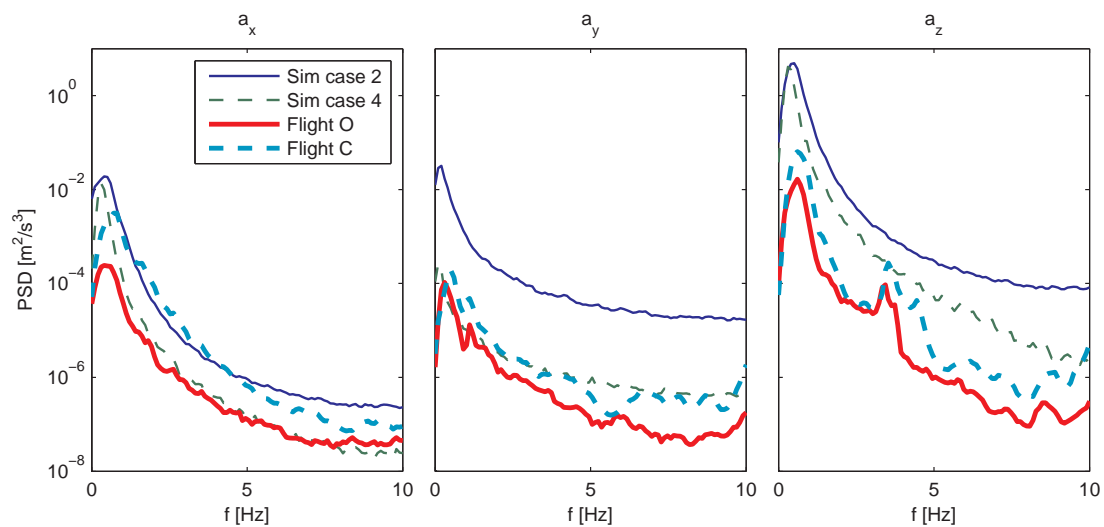
Figure 5.7. PSD functions of the acceleration components of the receiver, from the flight test data and from the simulation.
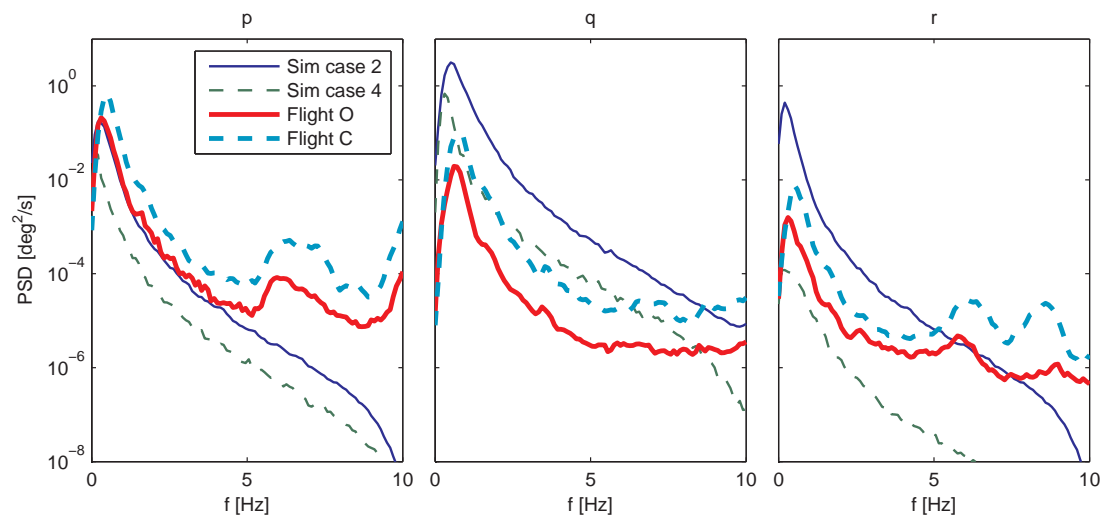
Figure 5.8. PSD functions of the angular velocity components of the receiver, from the flight test data and from the simulation.

observation PSD. The difference between the "relaxed" pilot at observation and the "stressful" pilot at contact is analogous to the difference between simulation receiver controllers 1 and 2.

Figures 5.7 and 5.8 show the difference between the simulation results with the two turbulence sources. In all cases the Dryden model turbulence source produces a simulation result with more power than the flight data turbulence source. This suggests that the Dryden model parameter identification procedure described in Section 4.3.1 results in stronger turbulence than the flight data turbulence.

The simulation cases have varying agreement with the flight data. In a_x, simulation case 2 matches the flight at contact position, while simulation case 4 matches the flight observation position. For a_y, simulation case 2 is far above the flight data, while simulation case 4 matches flight contact. For a_z, both simulation case 2 and 4 are above the flight data, although case 4 is closer to the flight data. In p, simulation case 2 seems to be the best match for the flight data, while simulation case 4 is too low. In q, simulation case 2 is again too high, while simulation case 4 is the better fit. Finally, in r, the flight data are bounded above by simulation case 2 and below by case 4. Overall, simulation case 4 seems to be the closer match but neither simulation case is in consistent agreement with the flight test. This can probably be explained by the differences in the flight test pilot and the controller used in the simulation, as well as shortcomings of the Dryden turbulence model and its parameter identification process. Additionally, the simulation does not have any sensor model—the flight data may be showing additional effect of sensor dynamics and noise.

5.2.2   Mean Variation Comparison

In this section, the mean variation of several receiver and tanker states is compared between the simulation results and the flight data. The mean variation compar-

ison reveals the effect of the deterministic components of the Wind Effect Modeling Technique—the prevailing wind and the trailing wake vortex. In order to make the mean variation as clear as possible, the signals in some of the following figures are smoothened using the moving average filter described in Eq. (3.8).

Figure 5.9 shows the receiver angle of attack, sideslip angle, and pitch angle $(\alpha,\ \beta,\ \theta)$ for the simulation and the test flight. At observation, the pitch angle is identical to the angle of attack. At contact position, the receiver pitches up from $2.5°$ to $3.5°$ due to the presence of downwash behind the tanker. Note that the performance of the simulation matches very well the behavior observed in the test flight. This indicates the accuracy of the vortex model used in the simulation.

Figure 5.10 shows the receiver and tanker air and ground speeds from the simulation. The same graph is shown for the flight data in Fig. 3.5. A detail of Fig. 5.10 is shown in Fig. 5.11. The same trend is observed in both the flight test and in the simulation. The airspeed of the receiver is the same as the tanker at the observation position. At the contact position, the receiver's airspeed is lower than the tanker's due to the additional wind induced by the wake vortices of the tanker. Figure 5.10 can also be used for comparison of the receiver or tanker airspeed with its own inertial speed. Since the test flight prevailing wind profile is used in the simulation and the aircraft ground tracks in the simulation match well the test flight, the aircraft in the simulation experience the exactly same head and tailwind as in the test flight. The consistency of the simulation with the test flight in this regard can be seen by comparing Fig. 5.10 with Fig. 3.5.

Figure 5.12 shows the engine thrust used in the flight test and the simulation. For the test flight, a differential engine pressure is shown, which is a measure of the engine thrust. For the simulation, the throttle setting percentage is shown. For both the simulation and the test flight, the receiver at contact increases the engine
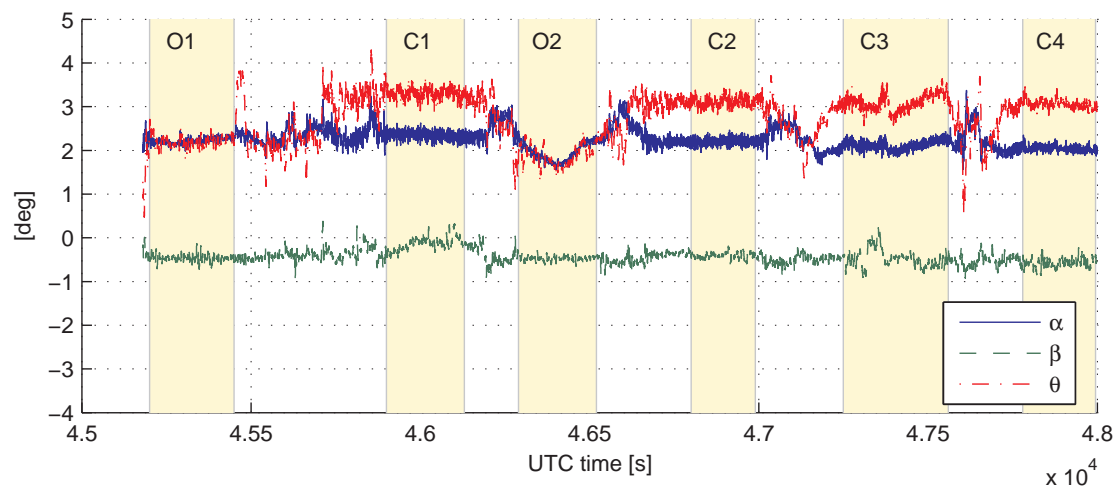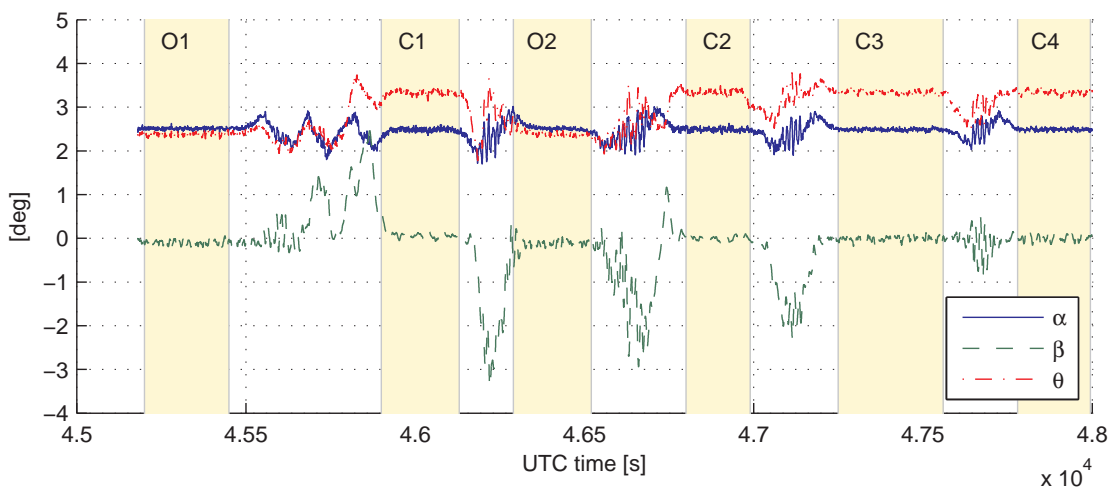
Figure 5.9. Receiver angle of attack, sideslip angle, and pitch angle. Comparison between flight data and simulation. (a) Flight data. (b) Simulation data, case 2.
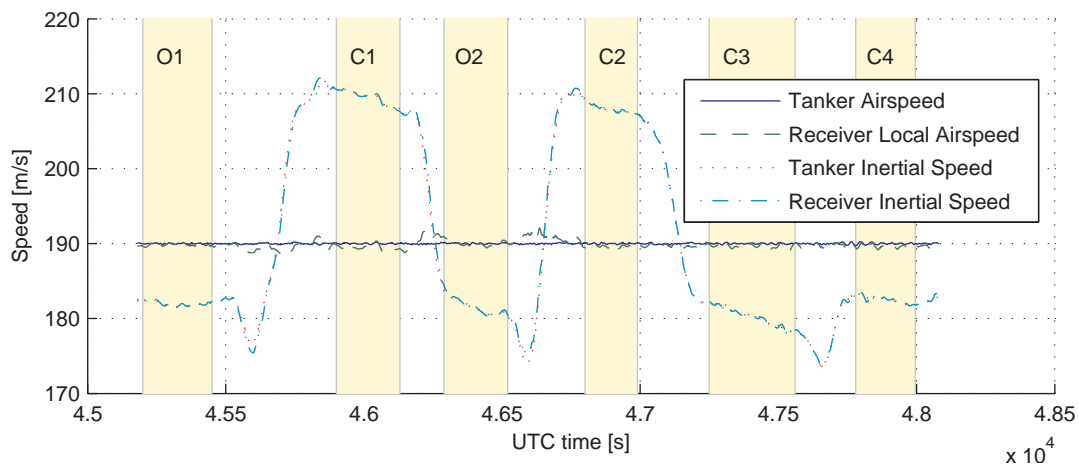
Figure 5.10. Comparison of airspeeds and GPS-based speeds of the tanker and the receiver. Simulation data, case 2.
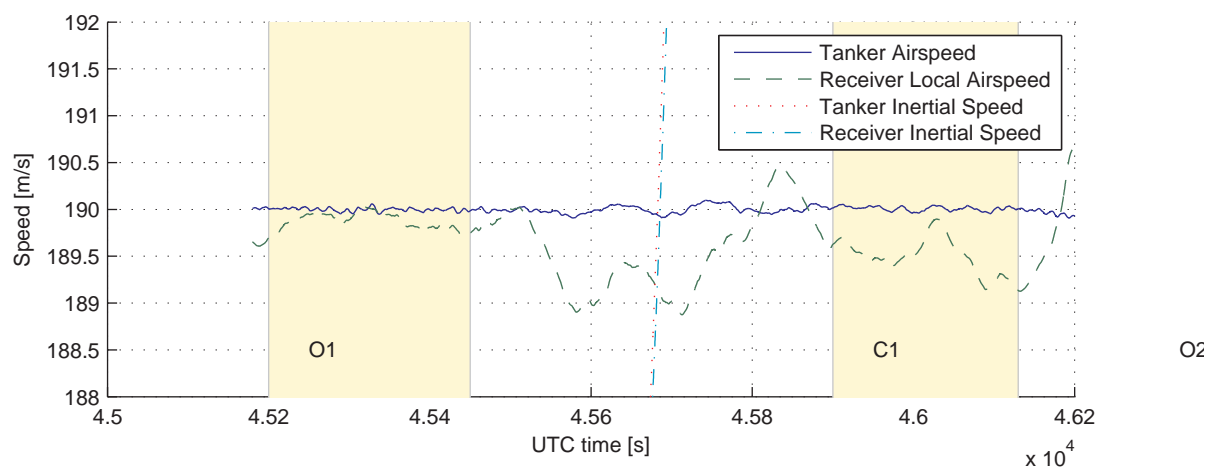
Figure 5.11. Detail view of airspeeds at observation-1 and contact-1 in Fig. 5.10.

power by about 20% to be able to maintain relative position with the tanker while experiencing the vortex induced wind.

Figure 5.13 shows the elevator, stabilizer, aileron, and rudder deflections for the receiver in the test flight. Figure 5.14 shows the same for simulation case 2. In the flight test, the stabilizer is mostly adjusted during the turns, while in the simulation the stabilizer remains fixed. In the flight test, the elevator deflection is decreased slightly at the contact position, while it slightly increases during the simulation. The rudder in the flight test seems to have a bias, where it is expected to remain trimmed at zero deflection, as in the simulation. The receiver in the simulation appears to use the aileron more during the turns than does the receiver in the flight test. Some of these differences are clearly due to the fact that the controller in the simulation does not represent the flight test pilot. Further, improvement in the Learjet 25 aerodynamic data in the simulation may reduce the difference in control surface response.

Figures 5.15–5.18 show the receiver wind in the receiver's body frame from the simulation. The same are plotted for the flight test in Figs. 3.8–3.10. In both the simulation, as shown in Fig. 5.16, and the flight, as shown in Fig. 3.9, the tanker and receiver wind components in the x-direction are the same at observation, but the receiver experiences, at the contact position, additional wind in the positive x-direction, induced by the tanker's wake vortices. Recall that the vortex-induced sidewash on the receiver at the first contact position was identified from the flight data (see Fig. 3.10). The sidewash observed at the first contact position was not seen at the other contact positions. This was attributed to the lateral offset for the first contact position from the tanker centerline. In the simulation, the first contact position is also 2 m offset from the tanker centerline. The comparison of the difference in y-components of the tanker and receiver winds when the aircraft are at observation-

Figure 5.12. Comparison between receiver throttle setting for the flight data and the simulation results. (a) Receiver differential jet engine pressure, flight data. (b) Receiver throttle setting, simulation data, case 2.

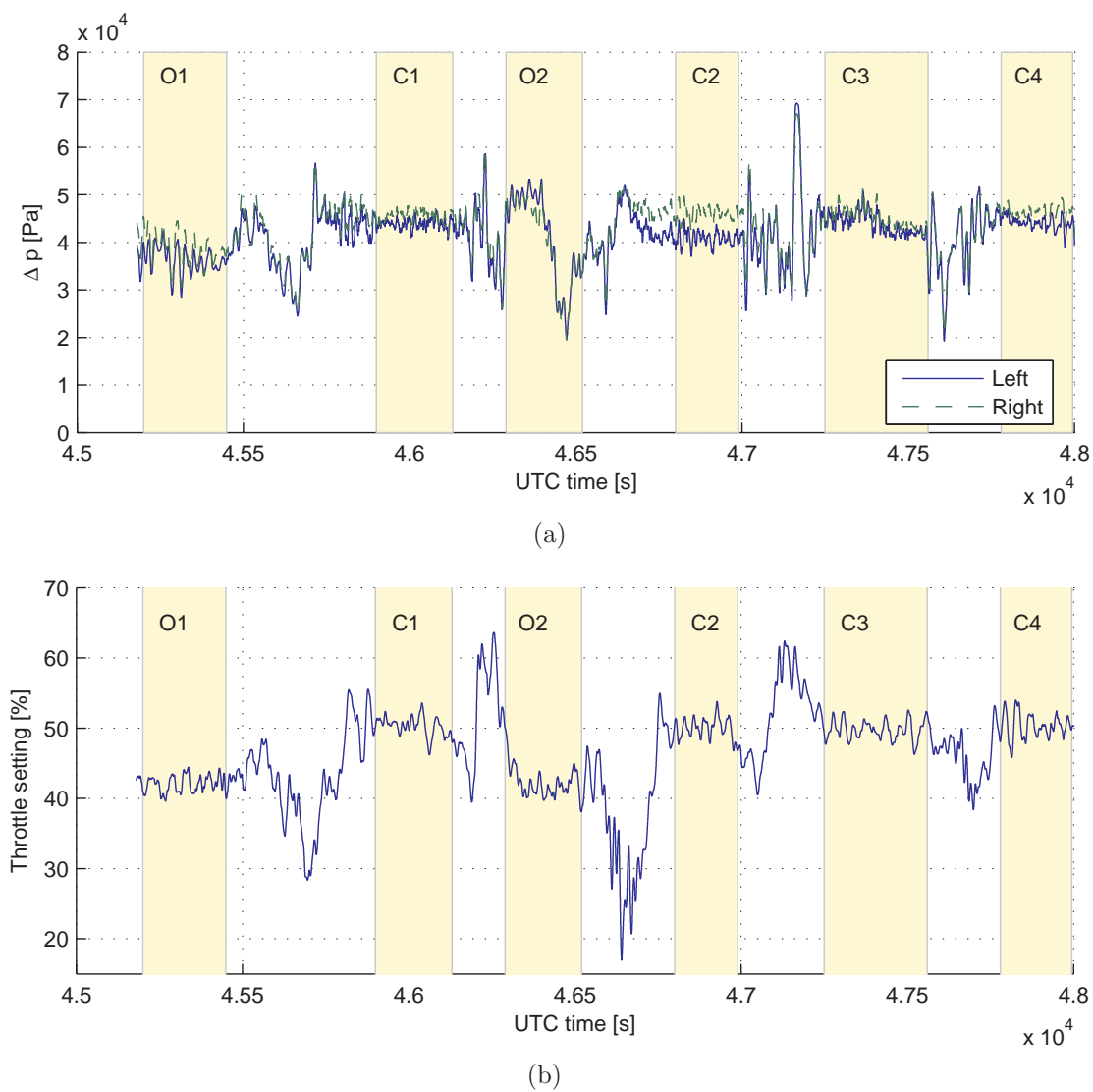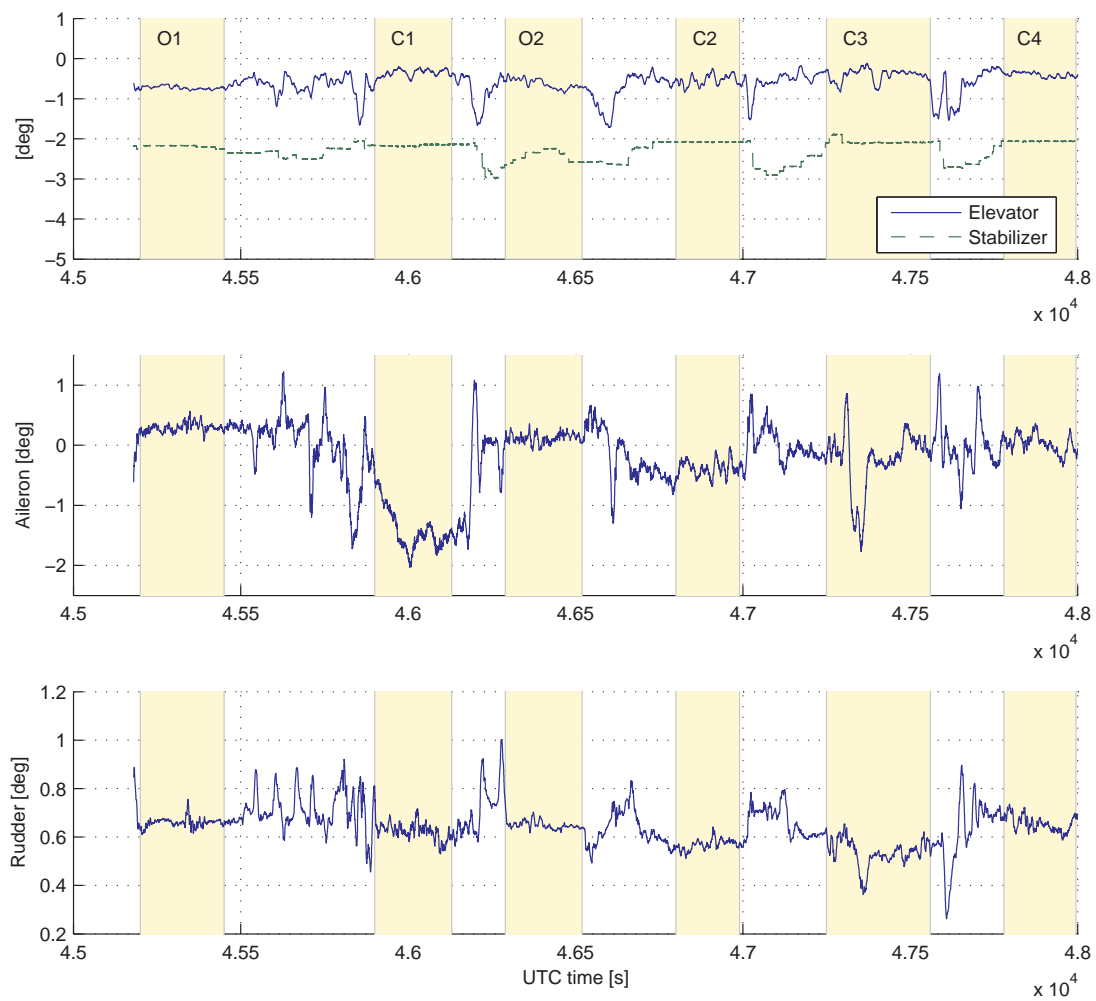Figure 5.13. Receiver control surface deflections, from the test flight.
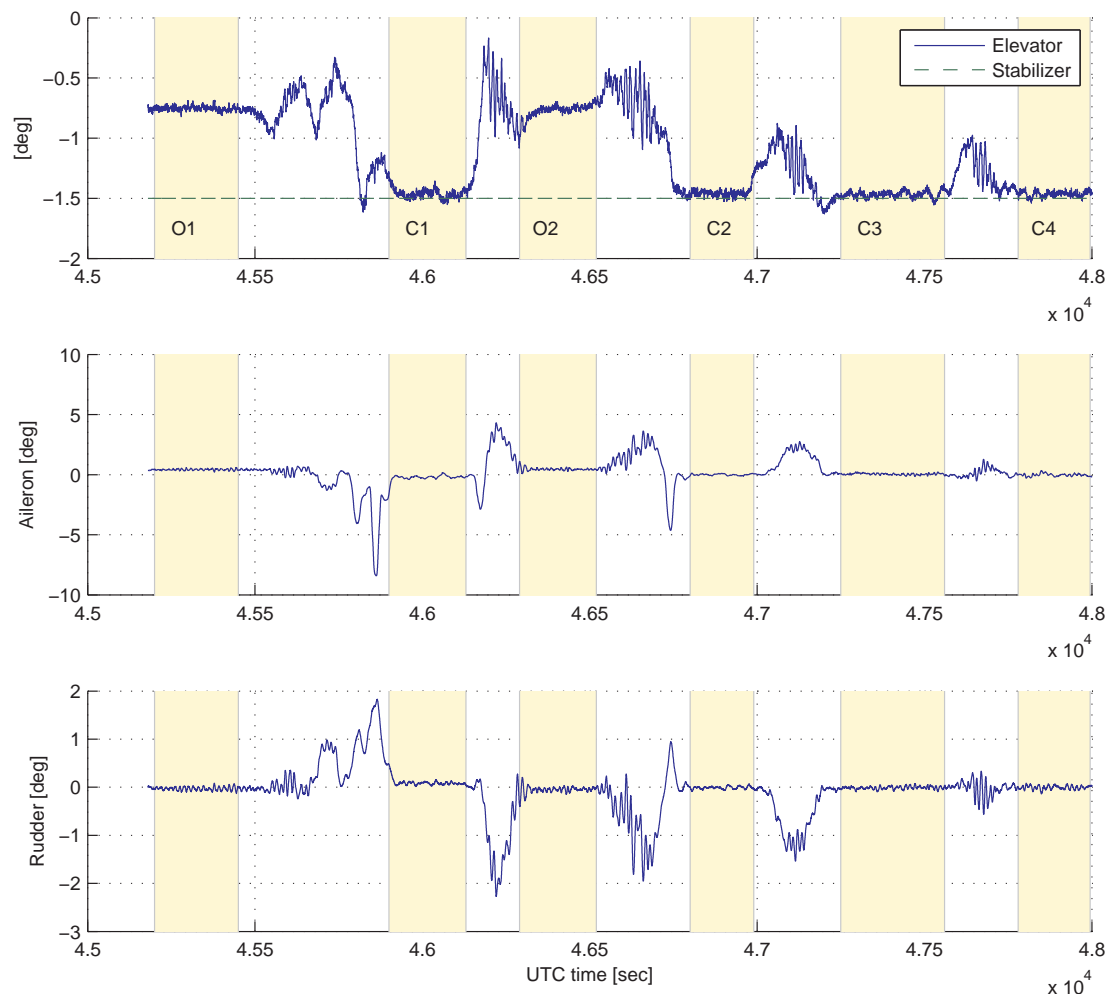
Figure 5.14. Receiver control surface deflections, from simulation case 2.

1 and contact-1 (see Fig. 5.17) shows a similar trend. However, the magnitude of the sidewash in the flight is about 1.4 m/s, much larger than the 0.3 m/s in the simulation. This could be due to the presence of the refueling boom in the flight. The refueling boom, present in the flight but not modeled in the simulation, has lifting control surfaces that can induce additional sidewash in the flight that was not observed in the simulation. The sidewash can also be seen in the simulation in the y-direction in Fig. 5.18, as the receiver moves laterally from observation to contact position, passing through the tanker vortex field. Note that as the receiver moves closer to the tanker centerline, the magnitude of the sidewash decreases because the vortices from the left and right wing/tail reduce each other's effect.

The z-component plot in Fig. 5.15 shows the downwash that the receiver experiences in the simulation when it is at the contact position. Note that the simulation result is in full agreement with the downwash observed in the test flight (Fig. 3.8). At the first two contact positions, the downwash is 4 m/s, identical to the downwash in the test flight when the aircraft are exposed to tailwind. At the last two contact positions when the aircraft are exposed to headwind, the downwash in the simulation is 2.5 m/s, also very close to the test flight. The difference, as explained in the test flight, is due to the prevailing wind being headwind or tailwind.

Figure 5.19 shows the wind vorticity experienced by the receiver in the simulation. Note that the receiver experiences wind rotation around the y-axis when it is at the contact positions, indicating a pitching moment induced by the tanker's trailing wake vortex. Note also that in the segments between the last three contact positions, q-rotation decreases but does not vanish. This is because during these segments the receiver stays close to the contact position at a slightly lower altitude. Figure 5.20 presents a detail view of Fig. 5.19 showing the vorticity increase that occurs when the receiver moves between observation-1 and contact-1. Moving through the tanker's
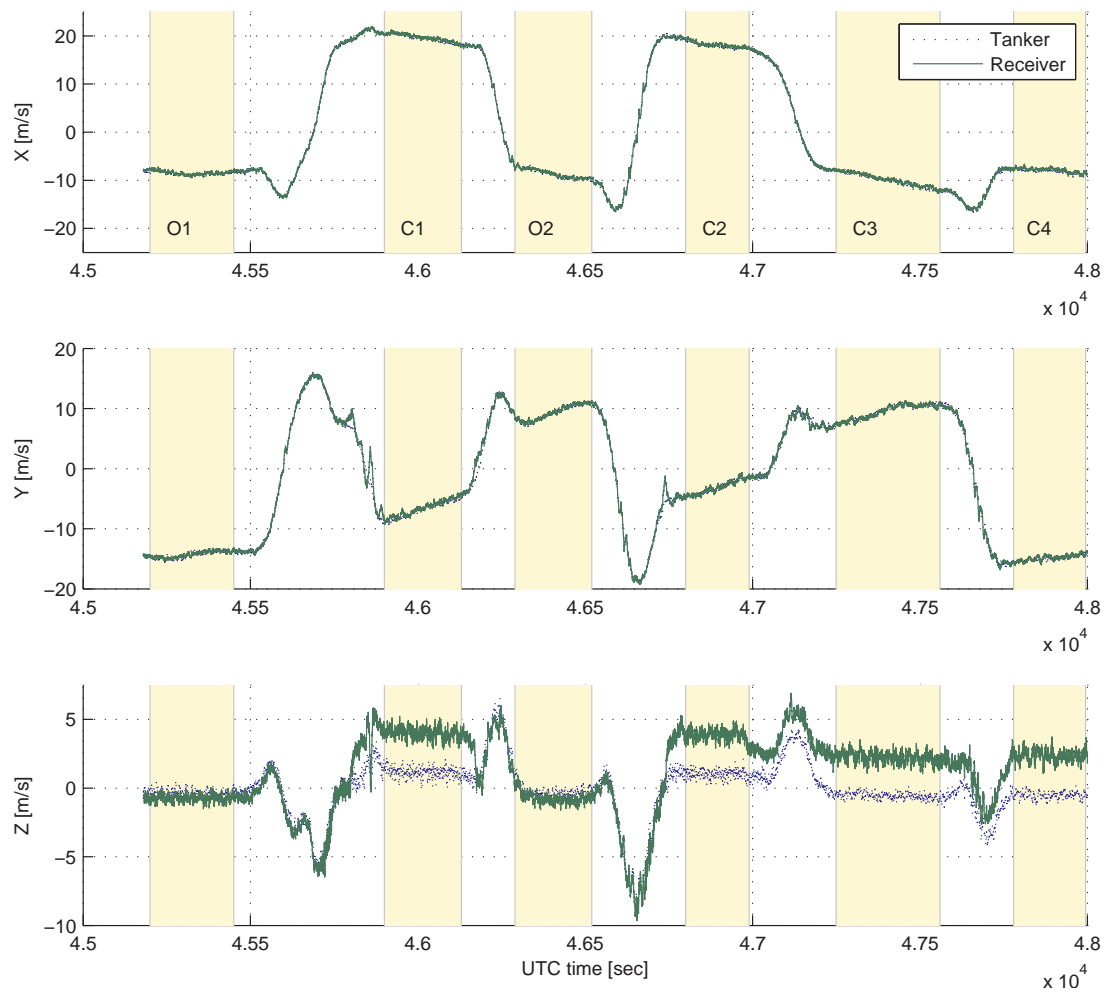
Figure 5.15. Wind components in receiver body frame, from simulation case 2.
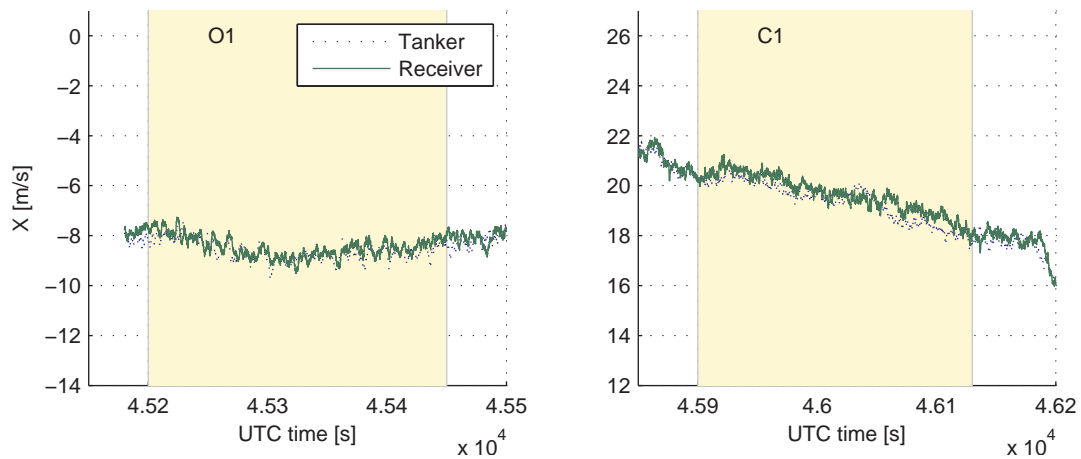
Figure 5.16. Detail view of the x-component of wind in observation-1 and contact-1 in Fig. 5.15.
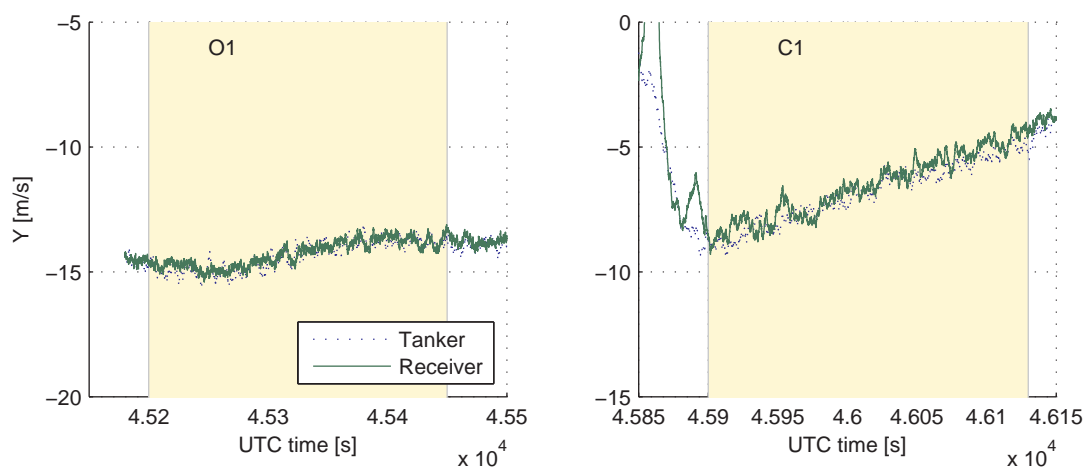
Figure 5.17. Detail view of the y-component of wind at observation-1 and contact-1 in Fig. 5.15.
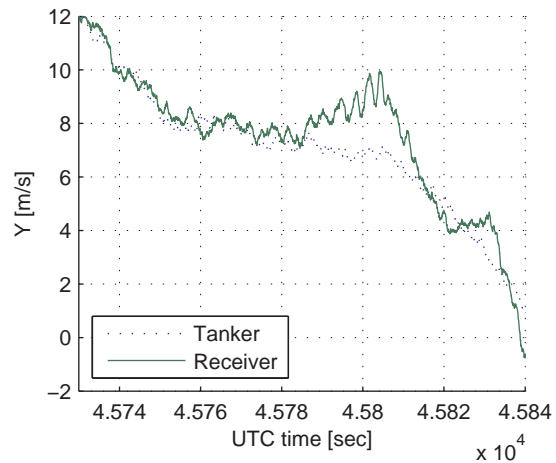
Figure 5.18. Detail view of the y-component of wind between observation-1 and contact-1 in Fig. 5.15.
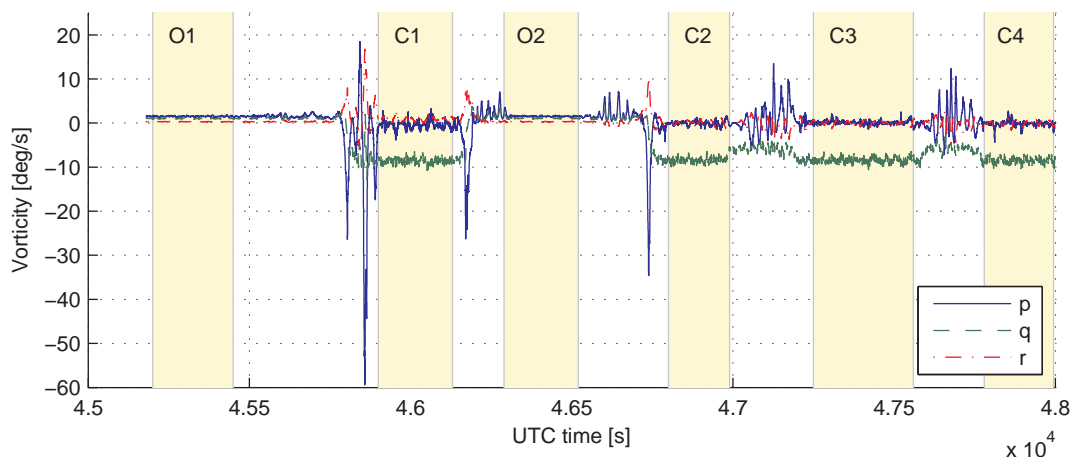
Figure 5.19. Receiver wind vorticity, from simulation case 2.
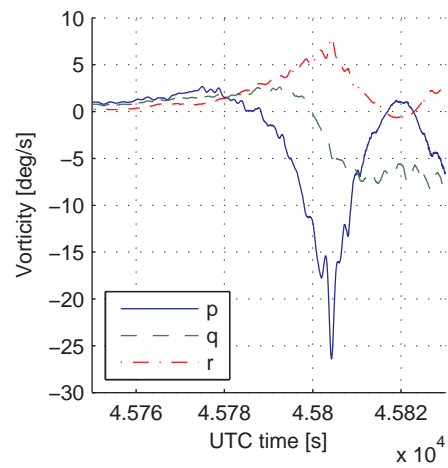
Figure 5.20. Detail view of Fig. 5.19.

wake vortex field in this fashion induces rolling and yawing moments. Unfortunately, these trends in the simulation cannot be validated against the flight data, since these measurements were unavailable from the test flight.

CHAPTER 6

CONCLUSIONS

Flight test data taken during a series of simulated aerial refueling maneuvers was analyzed. By manipulation of the existing air data measurements, the three components of the wind experienced by the tanker and receiver were separately identified. The effect of the induced winds from the tanker wake vortex system is clearly seen by comparing these components. The stochastic turbulence was characterized by comparing the deviation of the wind components from their mean value. A Power Spectral Density (PSD) analysis was performed to identify the parameters used by the Dryden turbulence model. This analysis showed that the turbulence characteristics of the wind do not change when the receiver moves to the contact position in the wake of the tanker. A PSD analysis of the acceleration and the angular velocity measurements showed a clear power increase in the signals when the receiver was flown at the contact position. This is attributed to the higher pilot workload required to maintain the contact position directly below the tanker.

Six degrees-of-freedom simulations were conducted in an attempt to replicate the flight results. Two controllers, a position command system and a speed, altitude and turn rate tracker, were studied. Different combinations of Dryden and flight-based turbulence models were also studied. A conclusive comparison of the simulation with the flight data in the frequency domain cannot be done because the simulation used a controller that does not accurately model the pilot. Nonetheless, the frequency response of the aircraft was found to differ depending on the turbulence modeling technique used, and the the acceleration and angular velocity responses in

the simulation with the flight data turbulence appeared closer to PSD computed from the flight data than those with the Dryden model.

Comparison between the simulation and the test flight in the time domain was more definitive. The VEMT (Vortex Effect Modeling Technique) was found to accurately model the effect of the wake vortex on the dynamics of the receiver aircraft. The response of the receiver when it went to the contact position in the simulation was in perfect agreement with the flight data. The increase in the pitch angle and thrust, and the decrease in the airspeed at the contact position relative to the observation position as observed in the test flight were repeated in the simulation. The induced wind components computed by VEMT in the simulation were also in agreement with those computed from the flight data. For example, the small decrease in the x-component of the wind and the increase in the downwash when the receiver moved to the contact position were clearly seen in the simulation. The effect of the prevailing wind on the downwash as experienced by the receiver was also shown in the simulation. A prevailing tailwind had a positive contribution to the downwash when the receiver flew with a positive pitch angle, and vice-versa. The prevailing wind also had an adverse effect on station-keeping performance. In the presence of strong prevailing wind, station-keeping performance during turns differed depending on the direction the tanker turns relative to the wind. Although not directly observed in the flight data, the simulation results also showed the sidewash effect of the wake vortices as well as the effective angular velocity of the air experienced by the receiver due to the induced nonuniform wind. This can be useful in explaining the response of the receiver moving behind the tanker in a test flight.

In future flight tests, the tanker and receiver flight measurements should be synchronized and sampled at the same rate to better facilitate post-flight analysis of the kind shown in the present work. Additional air data from the tanker, such

as the angle of attack and sideslip angle, should also be recorded, as it was for the receiver. Engine data such as a throttle setting should be recorded for both aircraft. Some of the assumptions made in the present work could be eliminated with better documentation of the locations of the sensors, as well as a detailed definition of the measured data.

The following topics are recommended for future work based on the experience gained in this research. Simulations that employ the VEMT can be used for developing controllers, evaluating closed-loop performance, and explaining observations from flight data. When data from a test flight where the receiver is flown by a controller rather than a pilot are available, similar analysis can be repeated. It would be much easier to implement the controller of the flight in the simulation than to model the pilot characteristics. This would eliminate the pilot induced effects that are difficult to isolate otherwise. This thesis has presented an effective method that can be implemented in real-time to compute the wind the aircraft is exposed to from the available sensor measurements. Aerial refueling control laws can be enhanced by this wind information. Relative dimensions of a pair of receiver-tanker aircraft may be a factor in the sensitivity of the receiver against the effect of the wake vortex. This can easily be analyzed with different receiver aircraft models, using the simulation environment developed. Additionally, different tanker-receiver combinations can be studied in the simulation environment. Further, performance of aerial refueling at different contact positions can be easily evaluated. Finally, the effect of the aerodynamic coupling on the tanker aircraft (e.g. bow wave effect) can be studied when the tanker and receiver aircraft are of similar size.

APPENDIX A

CONVERSION FROM GEODETIC TO LOCAL COORDINATES

In the flight data, tanker and receiver positions were recorded in terms of latitude, longitude, and altitude. In order to simulate their trajectories, it is necessary to convert these geodetic coordinates to a local rectangular coordinate system. Let (E) be the inertial frame fixed at the center of the Earth, with x_E at $0°$ longitude, y_E at $0°$ latitude, and z_E through the north pole. Let (I) be the local "flat Earth" inertial frame, described in Section 2.1. Now, x_I is aligned with the local north direction, y_I is aligned with the local east direction, and z_I points down toward the center of the Earth. The origin of (I) is the location of the tanker at the start of the test flight trajectory, at an altitude of 7010 m. The (x_I, y_I) plane is parallel to a plane tangent to the spherical Earth directly below the origin. Figure A.1 depicts these two frames, with the latitude and longitude angles (L_I, λ_I) of (I). Note that L is in positive degrees east and λ is in positive degrees north.

The rotation matrix from the (E) frame to the (I) frame is

$$\mathbf{R_{IE}} = \begin{bmatrix} -\sin L_I \cos \lambda_I & -\sin L_I \sin \lambda_I & \cos L_I \\ -\sin \lambda_I & \cos \lambda_I & 0 \\ -\cos L_I \cos \lambda_I & -\cos L_I \sin \lambda_I & -\sin L_I \end{bmatrix} \qquad \text{(A.1)}$$

Let (L_I, λ_I, h_I) be the latitude, longitude, and altitude of the origin of (I). Let (L_i, λ_i, h_i) be the same for some point i. Let $\underline{\rho}_i$ be the position vector of point i relative to (I). The representation of $\underline{\rho}_i$ in the I-frame has components given by

$$\rho_i = \mathbf{R_{IE}} \left\{ \begin{bmatrix} \cos L_i \cos \lambda_i \\ \cos L_i \sin \lambda_i \\ \sin L_i \end{bmatrix} (r + h_i) - \begin{bmatrix} \cos L_I \cos \lambda_I \\ \cos L_I \sin \lambda_I \\ \sin L_I \end{bmatrix} (r + h_I) \right\} \qquad \text{(A.2)}$$

where $r = 6{,}367{,}435$ m is the mean radius of the spherical Earth.
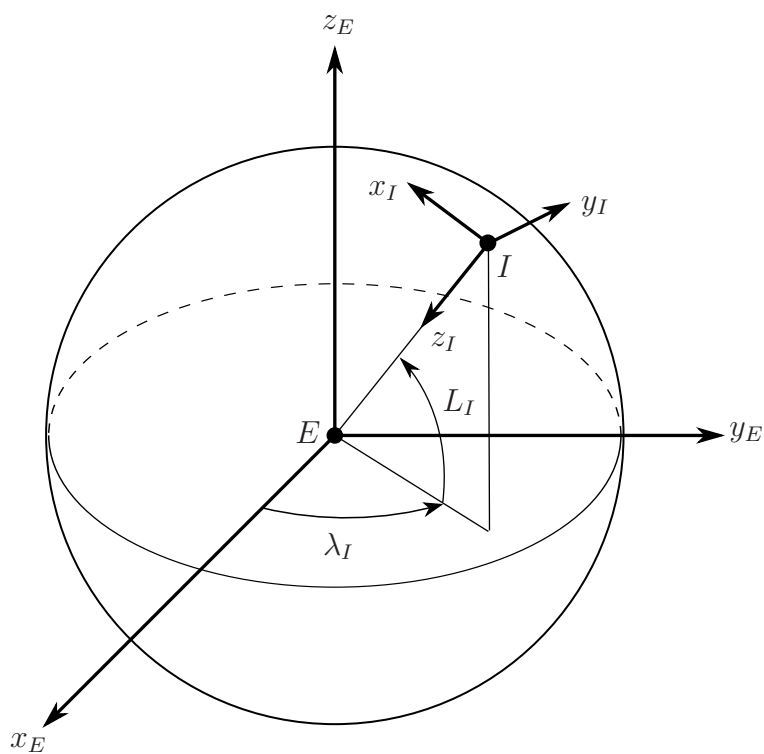
Figure A.1. Earth-centered and local coordinate systems, with latitude and longitude angles.

APPENDIX B

PSD FUNCTION TO STATE-SPACE CONVERSION

This appendix shows the spectral factorization procedure [44] to convert from the Dryden model PSD function form to the state-space representation as implemented in Simulink. The u_g and v_g components are shown for demonstration. The other components follow a similar procedure.

The Dryden PSD functions for the u_g and v_g components are [2]

$$\Phi_{u_g}(\Omega) \;=\; \sigma_u^2 \frac{2L_u}{\pi} \frac{1}{1+(L_u\Omega)^2} \tag{B.1}$$

$$\Phi_{v_g}(\Omega) \;=\; \sigma_v^2 \frac{L_v}{\pi} \frac{1+3(L_v\Omega)^2}{[1+(L_v\Omega)^2]^2} \tag{B.2}$$

The form of Φ_{u_g} and Φ_{v_g} given in Eqs. (B.1) and (B.2) are in terms of spatial frequency Ω in rad/m. These equations must be rewritten in terms of angular frequency ω in rad/s. This is accomplished using the following conversions [47]:

$$\Omega \;=\; \frac{\omega}{V} \tag{B.3}$$

$$\phi(\omega) \;=\; \frac{\Phi(\Omega)}{V} \tag{B.4}$$

where V is the magnitude of the nominal airspeed of the aircraft in m/s. First, Eq. (B.3) is substituted into Eqs. (B.1) and (B.2) for Ω. The result is divided by V according to Eq. (B.4), giving

$$\phi_{u_g}(\omega) \;=\; \sigma_u^2 \frac{2L_u}{\pi V} \frac{1}{1+(L_u\omega/V)^2} \tag{B.5}$$

$$\phi_{v_g}(\omega) \;=\; \sigma_v^2 \frac{L_v}{\pi V} \frac{1+3(L_v\omega/V)^2}{[1+(L_v\omega/V)^2]^2} \tag{B.6}$$

For each turbulence component, it is desired to use a linear filter $G(s)$ to shape a zero mean, unity-PSD Gaussian white noise input signal to yield an output random process with the PSD function described by the Dryden model functions. The relationship between the PSD of the input signal to a linear filter and the PSD of the output is

$$\phi_{\text{out}}(\omega) = |G(s)|^2_{s=j\omega}\, \phi_{\text{in}}(\omega) \tag{B.7}$$

In this case, $\phi_{\text{in}}(\omega) = 1$, which is the Gaussian white noise input. Therefore,

$$\phi_{\text{out}}(\omega) = |G(s)|^2_{s=j\omega} \tag{B.8}$$

Also note these equivalent statements

$$|G(s)|^2_{s=j\omega} = G(j\omega)G^*(j\omega) = G(j\omega)G(-j\omega) \tag{B.9}$$

where G^* is the complex conjugate of G. To identify $G(s)$, the task is to factor $\phi(\omega)$ into the product of some $G(j\omega)$ and its complex conjugate $G^*(j\omega)$ (or equivalently, $G(-j\omega)$). This factorization yields

$$\phi_{u_g}(\omega) = \sigma_u \sqrt{\frac{2L_u}{\pi V}} \frac{1}{1 + j\omega L_u/V} \cdot \sigma_u \sqrt{\frac{2L_u}{\pi V}} \frac{1}{1 + (-j\omega)L_u/V} \tag{B.10}$$

$$\phi_{v_g}(\omega) = \sigma_v \sqrt{\frac{L_v}{\pi V}} \frac{(1 + \sqrt{3}j\omega L_v/V)}{(1 + j\omega L_v/V)^2} \cdot \sigma_v \sqrt{\frac{L_v}{\pi V}} \frac{(1 + \sqrt{3}(-j\omega)L_v/V)}{(1 + (-j\omega)L_v/V)^2} \tag{B.11}$$

The procedure is to choose $G(s)$ from the above factors of $\phi(\omega)$ to have zeros and poles in the left side of the complex plane. This is the stable, minimum phase transfer function. By inspection, the transfer functions $G(s)$ for u_g and v_g are

$$G_{u_g}(s) = \sigma_u \sqrt{\frac{2L_u}{\pi V}} \frac{1}{1 + (L_u/V)s} \tag{B.12}$$

$$G_{v_g}(s) = \sigma_v \sqrt{\frac{L_v}{\pi V}} \frac{(1 + \sqrt{3}(L_v/V)s)}{(1 + (L_v/V)s)^2} \tag{B.13}$$

The conversion from transfer function to state-space model follows the standard procedure, first recognizing that

$$u_g(s) = G_{u_g}(s)\eta(s) \tag{B.14}$$

$$v_g(s) = G_{v_g}(s)\eta(s) \tag{B.15}$$

where η is the Gaussian white noise process driving the Dryden transfer function. The state-space representations are

$$\dot{u}_g = -\frac{V}{L_u}u_g + \sigma_u \sqrt{\frac{2V}{L_u \pi}}\,\eta \tag{B.16}$$

$$\begin{bmatrix} \dot{x}_1 \\ \dot{x}_2 \end{bmatrix} = \begin{bmatrix} 0 & 1 \\ -\dfrac{V^2}{L^2} & -\dfrac{2V}{L} \end{bmatrix} \begin{bmatrix} x_1 \\ x_2 \end{bmatrix} + \begin{bmatrix} 0 \\ \dfrac{V^2}{L^2} \end{bmatrix} \eta \tag{B.17a}$$

$$v_g = \sigma_v \sqrt{\frac{L_v}{\pi V}} \left(x_1 + \sqrt{3}\frac{L}{V} x_2 \right) \tag{B.17b}$$

APPENDIX C

6 DOF AIRCRAFT DYNAMICS EQUATIONS

The equations of motion used for the tanker and the receiver in this thesis are reproduced from Ref. [45]. We have added the Learjet 25's all-moving horizontal stabilizer to the receiver aircraft for this work, which was not present in Ref. [45]. The equations are otherwise identical.

C.1 Dynamics Equations of the Tanker Relative to the Inertial Frame

In matrix form, the translational kinematics equation is

$$\dot{r}_{B_T} \;=\; \mathbf{R_{B_T I}^T R_{B_T w_T}} V_{w_T} \tag{C.1}$$

where r_{B_T} is the position of the tanker relative to the inertial frame expressed in the inertial frame, $\mathbf{R_{B_T I}}$ is the rotation matrix from the inertial frame to the body frame of the tanker, $\mathbf{R_{B_T w_T}}$ is the rotation matrix from the tanker wind frame to body frame, V_{w_T} is the velocity of the tanker relative to the surrounding air expressed in the tanker wind frame.

Translational dynamics equation of the tanker aircraft in matrix form is

$$\begin{bmatrix} \dot{V}_T \\[4pt] \dot{\beta}_T \\[4pt] \dot{\alpha}_T \end{bmatrix} \;=\; \mathcal{E}_{\mathbf{T}}^{-1}\mathbf{S}(\omega_{\mathbf{B_T}})\mathbf{R_{B_T w_T}} V_{w_T} + \frac{1}{m_T}\mathcal{E}_{\mathbf{T}}^{-1}\left(\mathbf{R_{B_R I}} M_T \mathbf{R_{B_T w_T}} A_T + P_T\right) \tag{C.2}$$

where

$$\mathcal{E}_{\mathbf{T}}^{-1} = \begin{bmatrix} \cos\alpha_T\cos\beta_T & \sin\beta_T & \cos\beta_T\sin\alpha_T \\[6pt] -\frac{1}{V_T}\cos\alpha_T\sin\beta_T & \frac{1}{V_T}\cos\beta_T & -\frac{1}{V_T}\sin\alpha_T\sin\beta_T \\[6pt] -\frac{1}{V_T}\sec\beta_T\sin\alpha_T & 0 & \frac{1}{V_T}\cos\alpha_T\sec\beta_T \end{bmatrix} \tag{C.3}$$

The external forces acting on the tanker are the gravitational force M_T (expressed in the inertial frame), the aerodynamic force A_T (expressed in the wind frame

of the tanker) and propulsive force P_T (expressed in the body frame of the tanker).
In general, the representations of the forces are

$$M_T = \begin{bmatrix} 0 \\ 0 \\ m_T\,g \end{bmatrix} \quad A_T = \begin{bmatrix} -D_T \\ -S_T \\ -L_T \end{bmatrix} \quad P_T = \begin{bmatrix} T_T\cos\delta_T \\ 0 \\ -T_T\sin\delta_T \end{bmatrix} \tag{C.4}$$

where g is the gravitational acceleration, m_T is the mass of the tanker, $(D_T,\ S_T,\ L_T)$
are the drag, side force and lift on the tanker, respectively, T_T is the thrust magnitude,
and δ_T is the thrust inclination angle. Also, note that $\mathbf{S}(\cdot)$ is the skew-symmetric
matrix operation on the representation of a vector and defined as

$$\mathbf{S}(x) = \begin{bmatrix} 0 & x_3 & -x_2 \\ -x_3 & 0 & x_1 \\ x_2 & -x_1 & 0 \end{bmatrix} \tag{C.5}$$

for an arbitrary vector $\underline{x}$ with the representation $[x_1\ x_2\ x_3]^T$.

The aerodynamic forces are given by the following standard expressions

$$D_T = \frac{1}{2}\rho V_T^2 \mathcal{S}_T C_{D_T} \tag{C.6}$$

$$S_T = \frac{1}{2}\rho V_T^2 \mathcal{S}_T C_{S_T} \tag{C.7}$$

$$L_T = \frac{1}{2}\rho V_T^2 \mathcal{S}_T C_{L_T} \tag{C.8}$$

where $\mathcal{S}_T$ is the reference area of the tanker and ρ is the ambient air density. The
aerodynamic coefficients are

$$C_{D_T} = C_{D0} + C_{D\alpha^2}\,\alpha_T^2 \tag{C.9}$$

$$C_{S_T} = C_{S0} + C_{S\beta}\beta_T + C_{S\delta_r}\delta_{r_T} \tag{C.10}$$

$$C_{L_{wing}} = C_{L0} + C_{L\alpha}\alpha_T + C_{L\alpha2}\,(\alpha_T - \alpha_{ref})^2 + C_{Lq}\frac{c_T}{2V_T}q_T \tag{C.11}$$

$$C_{L_{tail}} = C_{L\delta_e}\delta_{e_T} \tag{C.12}$$

$$C_{L_T} = C_{L_{wing}} + C_{L_{tail}} \tag{C.13}$$

where (δ_{a_T}, δ_{e_T}, δ_{r_T}) are the deflections of the control surfaces (aileron, elevator, rudder, respectively) and c_T is the chord length for the tanker.

The rotational kinematics equation in matrix form is the well known standard equation:

$$\mathbf{R_{B_T I}} \mathbf{\dot{R}_{B_T I}} = -\mathbf{S}(\omega_{\mathbf{B_T}}) \tag{C.14}$$

where $\omega_{\mathbf{B_T}}$ is the representation of the angular velocity vector of the tanker relative to the inertial frame expressed in its own body frame as

$$\omega_{\mathbf{B_T}} = \begin{bmatrix} p_T \\ q_T \\ r_T \end{bmatrix} \tag{C.15}$$

The simulation uses a version of the rotational kinematics in terms of the 3-2-1 Euler angles.

The matrix form of the rotational dynamics of the tanker is modeled with the standard rotational dynamics equation:

$$\dot{\omega}_{B_T} = \underline{\mathbf{I}}_\mathbf{T}^{-1} M_{B_T} + \underline{\mathbf{I}}_\mathbf{T}^{-1} \mathbf{S}(\omega_{\mathbf{B_T}}) \underline{\mathbf{I}}_\mathbf{T} \omega_{B_T} \tag{C.16}$$

where $\underline{\mathbf{I}}_\mathbf{T}$ is the inertia matrix of the tanker aircraft, M_{B_T} is the moment of the external forces around the origin of tanker body frame and expressed in the tanker body frame as

$$M_{B_T} = \begin{bmatrix} \mathcal{L}_T \\ \mathcal{M}_T \\ \mathcal{N}_T \end{bmatrix} \tag{C.17}$$

$$\mathcal{L}_T = \frac{1}{2} \rho V_T^2 \mathcal{S}_T b_T C_{\mathcal{L}_T} \tag{C.18}$$

$$\mathcal{M}_T = \frac{1}{2} \rho V_T^2 \mathcal{S}_T c_T C_{\mathcal{M}_T} + \Delta_{z_T} T_T \tag{C.19}$$

$$\mathcal{N}_T = \frac{1}{2} \rho V_T^2 \mathcal{S}_T b_T C_{\mathcal{N}_T} \tag{C.20}$$

where b_T is the wingspan of the tanker aircraft and Δ_{z_T} is the moment arms of the thrust in the tanker's body frame. The aerodynamic moment coefficients are

$$C_{\mathcal{L}_T} = C_{\mathcal{L}0} + C_{\mathcal{L}\delta_a}\delta_{a_T} + C_{\mathcal{L}\delta_r}\delta_{r_T} + C_{\mathcal{L}\beta}\beta_T + C_{\mathcal{L}p}\frac{b_T}{2V_T}p_T + C_{\mathcal{L}r}\frac{b_T}{2V_T}r_T \qquad \text{(C.21)}$$

$$C_{\mathcal{M}_T} = C_{\mathcal{M}\alpha}\alpha_T + C_{\mathcal{M}\delta_e}\delta_{e_T} + C_{\mathcal{M}q}\frac{c_T}{2V_T}q_T \qquad \text{(C.22)}$$

$$C_{\mathcal{N}_T} = C_{\mathcal{N}0} + C_{\mathcal{N}\delta_a}\delta_{a_T} + C_{\mathcal{N}\delta_r}\delta_{r_T} + C_{\mathcal{N}\beta}\beta_T + C_{\mathcal{N}p}\frac{b_T}{2V_T}p_T + C_{\mathcal{N}r}\frac{b_T}{2V_T}r_T \qquad \text{(C.23)}$$

C.2 Dynamics Equations of the Receiver Relative to the Tanker Body Frame

In matrix form, the translational kinematics equation is

$$\dot{\xi} = \mathbf{R}_{\mathbf{B_R B_T}}^{\mathbf{T}}\mathbf{R}_{\mathbf{B_R w_R}}\,V_w + \mathbf{R}_{\mathbf{B_R B_T}}^{\mathbf{T}}\,W - \mathbf{R}_{\mathbf{B_T I}}\,\dot{r}_{B_T} + \mathbf{S}(\omega_{\mathbf{B_T}})\xi \qquad \text{(C.24)}$$

where ξ is the position of the receiver relative to the tanker expressed in the body frame of the tanker, $\mathbf{R}_{\mathbf{B_R w_R}}$ is the rotation matrix from the receiver wind frame to body frame, V_w is the velocity of the receiver relative to the surrounding air expressed in the receiver wind frame, W is the velocity of the surrounding air relative to the ground expressed in the receiver body frame, $\mathbf{R}_{\mathbf{B_R B_T}}$ is the rotation matrix from tanker body frame to receiver body frame, and $\dot{r}_{B_T}$ is the velocity of the tanker relative to the inertial frame.

The translational dynamics equation of the receiver aircraft including the wind effect in matrix form is

$$\begin{bmatrix} \dot{V}_R \\ \dot{\beta}_R \\ \dot{\alpha}_R \end{bmatrix} = \mathcal{E}_{\mathbf{R}}^{-1}\left[\mathbf{S}(\omega_{\mathbf{B_R B_T}}) + \mathbf{R}_{\mathbf{B_R B_T}}\mathbf{S}(\omega_{\mathbf{B_T}})\mathbf{R}_{\mathbf{B_R B_T}}^{\mathbf{T}}\right]\left(\mathbf{R}_{\mathbf{B_R w_R}}\,V_w + W\right)$$

$$-\mathcal{E}_{\mathbf{R}}^{-1}\dot{W} + \frac{1}{m_R}\mathcal{E}_{\mathbf{R}}^{-1}\left(\mathbf{R}_{\mathbf{B_R B_T}}\mathbf{R}_{\mathbf{B_T I}}M_R + \mathbf{R}_{\mathbf{B_R w_R}}\,A_R + P_R\right) \qquad \text{(C.25)}$$

where

$$\mathcal{E}_{\mathbf{R}}^{-1} = \begin{bmatrix} \cos\alpha\cos\beta & \sin\beta & \cos\beta\sin\alpha \\ -\frac{1}{V_R}\cos\alpha\sin\beta & \frac{1}{V_R}\cos\beta & -\frac{1}{V_R}\sin\alpha\sin\beta \\ -\frac{1}{V_R}\sec\beta\sin\alpha & 0 & \frac{1}{V_R}\cos\alpha\sec\beta \end{bmatrix} \tag{C.26}$$

The external forces acting on the receiver are the gravitational force M_R (expressed in the inertial frame), the aerodynamic force A_R (expressed in the wind frame of the receiver) and the propulsive force P_R (expressed in the body frame of the receiver). In general, the representations of the forces M_R, A_R and P_R are

$$M_R = \begin{bmatrix} 0 \\ 0 \\ m_R g \end{bmatrix} \quad A_R = \begin{bmatrix} -D \\ -S \\ -L \end{bmatrix} \quad P_R = \begin{bmatrix} T_x \\ T_y \\ T_z \end{bmatrix} \tag{C.27}$$

where m_R is the mass of the receiver, $(D,\ S,\ L)$ are the drag, side force and lift on the receiver, respectively, and $(T_x,\ T_y,\ T_z)$ are the components of the thrust vector in the body frame of the receiver.

The aerodynamic forces are given by

$$D = \frac{1}{2}\rho V_R^2 \mathcal{S}_R C_D \tag{C.28}$$

$$S = \frac{1}{2}\rho V_R^2 \mathcal{S}_R C_S \tag{C.29}$$

$$L = \frac{1}{2}\rho V_R^2 \mathcal{S}_R C_L \tag{C.30}$$

where $\mathcal{S}_R$ is the reference area of the receiver. The aerodynamic coefficients are

$$C_D = C_{D0} + C_{D\alpha}\alpha + C_{D\alpha2}\alpha^2 + C_{D\delta_e}\delta_e + C_{D\delta_e2}\delta_e^2 + C_{D\delta_s}\delta_s + C_{D\delta_s2}\delta_s^2 \tag{C.31}$$

$$C_S = C_{S0} + C_{S\beta}\beta + C_{S\delta_a}\delta_a + C_{S\delta_r}\delta_r \tag{C.32}$$

$$C_L = C_{L0} + C_{L\alpha}\alpha + C_{L\alpha2}(\alpha - \alpha_{ref})^2 + C_{Lq}\frac{c}{2V_R}q_{rel} + C_{L\delta_e}\delta_e + C_{L\delta_s}\delta_s \tag{C.33}$$

where $(\delta_a,\ \delta_e,\ \delta_s,\ \delta_r)$ are the deflections of the control effectors (aileron, elevator, stabilizer, rudder). Note that, in Eq. (C.33), q_{rel} is the angular velocity of the receiver relative to the surrounding air around the body y-axis.

The rotational kinematics equation of the receiver aircraft in matrix form is also the well known standard equation:

$$\mathbf{R_{B_R B_T}} \dot{\mathbf{R}}_{\mathbf{B_R B_T}}^{\mathbf{T}} = -\mathbf{S}(\omega_{\mathbf{B_R B_T}}) \tag{C.34}$$

where $\omega_{B_R B_T}$ is the representation of the angular velocity vector of the receiver aircraft relative to the tanker body frame expressed in its own body frame as

$$\omega_{B_R B_T} = \begin{bmatrix} p_{R_T} \\ q_{R_T} \\ r_{R_T} \end{bmatrix} \tag{C.35}$$

The matrix form of the rotational dynamics of the receiver is also modeled as

$$\begin{aligned} \dot{\omega}_{B_R B_T} &= \underline{\mathbf{I}}_{\mathbf{R}}^{-1} M_{B_R} + \underline{\mathbf{I}}_{\mathbf{R}}^{-1} \mathbf{S}(\omega_{\mathbf{B_R B_T}} + \mathbf{R_{B_R B_T}} \omega_{\mathbf{B_T}}) \underline{\mathbf{I}}_{\mathbf{R}} \left(\omega_{B_R B_T} + \mathbf{R_{B_R B_T}} \omega_{B_T} \right) \\ &\quad - \mathbf{S}(\omega_{\mathbf{B_R B_T}}) \mathbf{R_{B_R B_T}} \omega_{B_T} - \mathbf{R_{B_R B_T}} \dot{\omega}_{B_T} \end{aligned} \tag{C.36}$$

where $\underline{\mathbf{I}}_{\mathbf{R}}$ is the inertia matrix of the receiver aircraft, M_{B_R} is the moment of the external forces around the origin of the receiver body frame and expressed in the receiver body frame as

$$M_{B_R} = \begin{bmatrix} \mathcal{L} \\ \mathcal{M} \\ \mathcal{N} \end{bmatrix} \tag{C.37}$$

The moment has two main components; due to aerodynamic forces and due to the thrust, thus

$$\mathcal{L} = \frac{1}{2} \rho V_R^2 \mathcal{S}_R b C_{\mathcal{L}} - \Delta_z T_y + \Delta_y T_z \tag{C.38}$$

$$\mathcal{M} = \frac{1}{2} \rho V_R^2 \mathcal{S}_R c C_{\mathcal{M}} - \Delta_z T_x - \Delta_x T_z \tag{C.39}$$

$$\mathcal{N} = \frac{1}{2} \rho V_R^2 \mathcal{S}_R b C_{\mathcal{N}} - \Delta_y T_x + \Delta_x T_y \tag{C.40}$$

where b is the wingspan, c is the cord length of the receiver aircraft, and $(\Delta_x, \Delta_y, \Delta_z)$ are the moment arms of the thrust in the body frame of the receiver. The aerodynamic moment coefficients are

$$C_{\mathcal{L}} = C_{\mathcal{L}0} + C_{\mathcal{L}\delta_a}\delta_a + C_{\mathcal{L}\delta_r}\delta_r + C_{\mathcal{L}\beta}\beta + C_{\mathcal{L}p}\frac{b}{2V_R}p_{rel} + C_{\mathcal{L}r}\frac{b}{2V_R}r_{rel} \tag{C.41}$$

$$C_{\mathcal{M}} = C_{\mathcal{M}0} + C_{\mathcal{M}\alpha}\alpha + C_{\mathcal{M}\delta_e}\delta_e + C_{\mathcal{M}\delta_s}\delta_s + C_{\mathcal{M}q}\frac{c}{2V_R}q_{rel} \tag{C.42}$$

$$C_{\mathcal{N}} = C_{\mathcal{N}0} + C_{\mathcal{N}\delta_a}\delta_a + C_{\mathcal{N}\delta_r}\delta_r + C_{\mathcal{N}\beta}\beta + C_{\mathcal{N}p}\frac{b}{2V_R}p_{rel} + C_{\mathcal{N}r}\frac{b}{2V_R}r_{rel} \tag{C.43}$$

where $(p_{rel}, q_{rel}, r_{rel})$ are components of the angular velocity of the aircraft relative to the surrounding air. When the aircraft is in a vortex field as in the case of tanker's trailing wake vortex field, these angular velocity components will be different from the angular velocity relative to the tanker.

APPENDIX D

TANKER AND RECEIVER CONTROLLERS

The controllers for the tanker and the receiver used in this thesis were developed in Ref. [45]. The tanker controller used here is identical to that of [45]. Receiver controller-1 is based on [45], but the weighting matrices in the LQR cost function are set such that thrust vectoring control variables are not used. This is obviously because the Learjet 25 does not have thrust vectoring capability. Another modification from Ref. [45] is that the number of nominal conditions used in the gain scheduling is increased from 4 to 6. This is done to include nominal conditions of aircraft turning right and left. The following summarizes Ref. [45] to show the overall structure of the control laws.

The tanker controller and both receiver controllers share a common MIMO state feedback LQR and integral control design, with gain scheduling control based on commanded speed and yaw rate. A block diagram of the controllers is shown in Fig. D.1. The gain scheduling controller is based on the four nominal conditions shown in Table D.1. Two of the conditions correspond to straight, steady-level flight, and the other two correspond to steady turns.
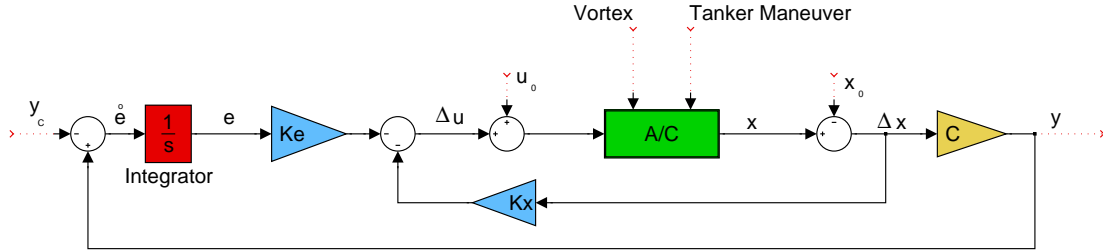

Figure D.1. State feedback and integral control structure. Reproduced from [45].

The state vector based on the linearized equations of motion in Appendix C for both aircraft is

$$\Delta \underline{x} = [\Delta V \ \Delta \beta \ \Delta \alpha \ \Delta p \ \Delta q \ \Delta r \ \Delta \psi \ \Delta \theta \ \Delta \phi \ \Delta x \ \Delta y \ \Delta z]^{T} \qquad (D.1)$$

Table D.1. Controller nominal conditions

Nominal Condition	Yaw rate	Airspeed
1	$\dot{\psi}_1$	V_1
2	$\dot{\psi}_1$	V_2
3	$\dot{\psi}_2$	V_1
4	$\dot{\psi}_2$	V_2

The control input vectors for the controllers are

$$\Delta\underline{u} = [\Delta\delta_a \ \Delta\delta_e \ \Delta\delta_r \ \Delta\xi \ ]^T \qquad \text{(Tanker)} \qquad \text{(D.2)}$$

$$\Delta\underline{u} = [\Delta\delta_a \ \Delta\delta_e \ \Delta\delta_r \ \Delta\xi \ \Delta\delta_y \ \Delta\delta_z]^T \qquad \text{(Receiver)} \qquad \text{(D.3)}$$

where ξ is a throttle setting. In the control input vector for the receiver, δ_y and δ_z are engine nozzle deflections for an aircraft capable of thrust vectoring control. Thrust vectoring is not used on the Learjet 25 receiver in this thesis by using very high weighting in the LQR cost function for these control variables. As a result, they are fixed at their nominal values.

Recall from Section 5.1 that the tanker controller and receiver controller-2 are airspeed, altitude, and yaw rate tracking, and the receiver controller-1 is tanker-receiver relative position tracking. Thus, the error vectors for the controllers are

$$\underline{\dot{e}} = \begin{bmatrix} \Delta V - \Delta V_c \\ \Delta z - \Delta z_c \\ \Delta\dot{\psi} - \Delta\dot{\psi}_c \end{bmatrix} \qquad \text{(Tanker, Receiver controller-2)} \qquad \text{(D.4)}$$

$$\underline{\dot{e}} = \begin{bmatrix} \Delta x - \Delta x_c \\ \Delta y - \Delta y_c \\ \Delta z - \Delta z_c \end{bmatrix} \qquad \text{(Receiver controller-1)} \qquad \text{(D.5)}$$

In the above equations, Δ indicates deviation from the nominal condition. Subscript c is the commanded signal. The state feedback control laws are

$$\Delta\underline{u_i} = -\mathbf{K_{x_i}}\,\Delta\underline{x} - \mathbf{K_{e_i}}\,\underline{e} \tag{D.6}$$

where $i \in \{1, 2, 3, 4\}$ correspond to the four nominal conditions in Table D.1, and $[\mathbf{K_x}\ \mathbf{K_e}]$ is the state feedback gain matrix obtained by minimizing the cost function in the LQR design technique. A gain scheduling controller is employed with Lagrangian interpolation between the linear controllers at the four nominal conditions. The gain scheduling control law is

$$
\begin{aligned}
\Delta\underline{u} =\ & \frac{\left(\dot{\psi}_c - \dot{\psi}_2\right)(V_c - V_2)}{\left(\dot{\psi}_1 - \dot{\psi}_2\right)(V_1 - V_2)}\,\underline{u}_1 + \frac{\left(\dot{\psi}_c - \dot{\psi}_2\right)(V_c - V_1)}{\left(\dot{\psi}_1 - \dot{\psi}_2\right)(V_2 - V_1)}\,\underline{u}_2 \\
& + \frac{\left(\dot{\psi}_c - \dot{\psi}_1\right)(V_c - V_2)}{\left(\dot{\psi}_2 - \dot{\psi}_1\right)(V_1 - V_2)}\,\underline{u}_3 + \frac{\left(\dot{\psi}_c - \dot{\psi}_1\right)(V_c - V_1)}{\left(\dot{\psi}_2 - \dot{\psi}_1\right)(V_2 - V_1)}\,\underline{u}_4
\end{aligned}
\tag{D.7}
$$

For the tanker controller and receiver controller-1, the gain scheduling controller is based on the tanker's commanded airspeed and yaw rate. Receiver controller-2 uses the receiver's commanded airspeed and yaw rate.

REFERENCES

[1] Waishek, J., *Derivation of the Dynamics Equations for Receiver Aircraft in Aerial Refueling*, MSAE thesis, The University of Texas at Arlington, Arlington, TX, December 2007.

[2] "Flying Qualities of Piloted Airplanes," Tech. Rep. U.S. Military Specification MIL-F-8785C, 5 November 1980.

[3] Bloy, A. and Trochalidis, V., "Performance and longitudinal stability and control of large receiver aircraft during air to air refueling," *Aeronautical Journal*, Vol. 93:930, 1989, pp. 367–378.

[4] Bloy, A., West, M., Lea, K., and Jouma'a, M., "Lateral aerodynamics interference between tanker and receiver in air-to-air refueling," *Journal of Aircraft*, Vol. 30:5, 1993, pp. 705–710.

[5] Bloy, A. and West, M., "Interference between tanker wing wake with roll-up and receiver aircraft," *Journal of Aircraft*, Vol. 31:5, 1994, pp. 1214–1216.

[6] Bloy, A. and Jouma'a, M., "Lateral and directional stability and control in air-to-air refueling," *Proceedings of the Institution of Mechanical Engineers, Part G: Journal of Aerospace Engineering*, Vol. 209:4, 1995, pp. 299–305.

[7] Bloy, A. and Lea, K., "Directional stability of a large receiver aircraft in air-to-air refueling," *Journal of Aircraft*, Vol. 32:2, 1995, pp. 453–455.

[8] Pachter, M., Houpis, C., and Trosen, D., "Design of an air-to-air automatic refueling flight control system using quantitative feedback theory," *International Journal of Robust and Nonlinear Control*, Vol. 7:6, 1997, pp. 561–580.

[9] Coblei, B., "Capabilities and Future Applications of the NASA Autonomous Formation Flight (AFF) Aircraft," *AIAA 1st UAV Conference*, Portsmouth, VA, May 2002, AIAA paper 2002-3443.

[10] Valasek, J., Kimmett, J., Hughes, D., Gunnam, K., and Junkins, J., "Vision Based Sensor and Navigation System for Autonomous Aerial Refueling," *AIAA 1st UAV Conference*, Portsmouth, VA, May 2002, AIAA paper 2002-3441.

[11] Johnson, K. and Awni, K., "A Roll Autopilot for Autonomous Air Refueling," *AIAA Guidance, Navigation, and Control Conference and Exhibit*, Monterey, CA, August 2002, AIAA paper 2002-4752.

[12] Fravolini, M., Ficola, A., Napolitano, M., Campa, G., and Perhinschi, M., "Development of Modelling and Control Tools for Aerial Refueling for UAVs," *AIAA Guidance, Navigation, and Control Conference and Exhibit*, Austin, TX, August 2003, AIAA paper 2003-5798.

[13] Campa, G., Seanor, B., Perhinschi, M., Fravolini, M., Ficola, A., and Napolitano, M., "Autonomous Aerial Refueling for UAVs Using a Combined GPS-Machine Vision Guidance," *AIAA Guidance, Navigation, and Control Conference and Exhibit*, Providence, RI, August 2004.

[14] Lavretsky, V. S. E. and Hovakimyan, N., "Aerial Refueling Autopilot Design Methodology: Application to F-16 Aircraft Model," *AIAA Guidance, Navigation, and Control Conference and Exhibit*, Providence, RI, August 2004.

[15] Hansen, J., Murray, J., and Campos, N., "The NASA Dryden AAR Project: A Flight Test Approach to an Aerial Refueling System," *AIAA Atmospheric Flight Mechanics Conference and Exhibit*, Providence, RI, August 2004.

[16] Bennington, M. A. and Visser, K. D., "Aerial Refueling Implications for Commercial Aviation," *Journal of Aircraft*, Vol. 42:2, 2005, pp. 366–375.

[17] Jewell, W. and Stapleford, R., "Mathematical Models used to Simulate Aircraft Encounters with Wake Vortices," No. STI TR-1035-4 (DOT-FA73WA-3276-1), 1975, pp. 38–57.

[18] Pachter, M., D'Azzo, J., and Proud, A., "Tight Formation Flight Control," *Journal of Guidance, Control, and Dynamics*, Vol. 24:2, 2001, pp. 246–254.

[19] Johnson, W., Teper, G., and Rediess, H., "Study of Control System Effectiveness in Alleviating Vortex Wake Upsets," *Journal of Aircraft*, Vol. 11:3, 1974, pp. 148–154.

[20] Dogan, A. and Venkataramanan, S., "Nonlinear Control for Reconfiguration of Unmanned–Aerial–Vehicle Formation," *Journal of Guidance, Control and Dynamics*, Vol. 28:4, 2005, pp. 667–678.

[21] Dogan, A., Venkataramanan, S., and Blake, W., "Modeling of Aerodynamic Coupling Between Aircraft in Close Proximity," *Journal of Aircraft*, Vol. 42:4, 2005, pp. 941–955.

[22] Venkataramanan, S. and Dogan, A., "Modeling of Aerodynamic Coupling Between Aircraft in Close Proximities," *Proceedings of the AIAA Atmospheric Flight Mechanics Conference and Exhibit*, Providence, RI, August 2004, AIAA paper 2004-5172.

[23] Venkataramanan, S. and Dogan, A., "Dynamic Effects of Trailing Vortex with Turbulence & Time-varying Inertia in Aerial Refueling," *Proceedings of the AIAA Atmospheric Flight Mechanics Conference and Exhibit*, Providence, RI, August 2004, AIAA paper 2004-4945.

[24] Venkataramanan, S. and Dogan, A., "A MultiUAV Simulation for Formation Reconfiguration," *Proceedings of the AIAA Modeling and Simulation Technologies Conference and Exhibit*, Providence, RI, August 2004, AIAA paper 2004-4800.

[25] Venkataramanan, S., Dogan, A., and Blake, W., "Vortex Effect Modelling in Aircraft Formation Flight," *Proceedings of the AIAA Atmospheric Flight Mechanics Conference and Exhibit*, Austin, TX, August 2003, AIAA paper 2003-5385.

[26] Venkataramanan, S. and Dogan, A., "Nonlinear Control for Reconfiguration of UAV Formation," *Proceedings of the AIAA Guidance, Navigation, and Control Conference*, Austin, TX, August 2003, AIAA paper 2003-5725.

[27] Venkataramanan, S., *Dynamics and Control of Multiple UAVs Flying in Close Proximity*, MSAE thesis, The University of Texas at Arlington, Arlington, TX, July 2004.

[28] Dogan, A., Sato, S., and Blake, W., "Flight Control and Simulation for Aerial Refueling," *Proceedings of AIAA Guidance, Navigation, and Control Conference*, San Francisco, CA, August 2005, AIAA paper 2005-6264.

[29] Kim, E., Dogan, A., and Blake, W., "Control of a Receiver Aircraft Relative to the Tanker in Racetrack Maneuver," *Proceedings of the AIAA Guidance, Navigation, and Control Conference*, Keystone, CO, August 2006, AIAA paper 2006-6710.

[30] Tucker, J., Dogan, A., and Blake, W., "Derivation of the Dynamics Equations of Receiver Aircraft in Aerial Refueling," *Proceedings of the AIAA 45th AIAA Aerospace Sciences Meeting and Exhibit*, Reno, NV, August 2007, AIAA paper 2007-251.

[31] Tandale, M. D., Bowers, R., and Valasek, J., "Trajectory Tracking Controller for Vision-Based Probe and Drogue Autonomous Aerial Refueling," *Journal of Guidance, Control, and Dynamics*, Vol. 29:4, 2006, pp. 846–857.

[32] Franklin, G. F., Powell, J. D., and Workman, M., *Digital Control of Dynamic Systems*, chap. 5, Addison Wesley Longman, Menlo Park, CA, 1998.

[33] *MATLAB Documentation*, The MathWorks, R2007b.

[34] Proakis, J. G., Rader, C. M., Ling, F., and Nikias, C. L., *Advanced Digital Signal Processing*, chap. 1, Macmillan Publishing Company, New York, NY, 1992.

[35] Stoica, P. and Moses, R., *Introduction to Spectral Analysis*, chap. 1–2, Prentice Hall, Upper Saddle River, NJ, 1997.

[36] Stoica, P. and Moses, R., *Spectral Analysis of Signals*, chap. 2.7.2, Pearson Education, Inc., Upper Saddle River, NJ.

[37] Lan, C. E. and Roskam, J., *Airplane Aerodynamics and Performance*, Roskam Aviation and Engineering Corporation, Ottawa, KS, 1988.

[38] Staff, A. R., "Equations, Tables, and Charts for Compressible Flow," Tech. Rep. 1135, NACA, Ames Aeronautical Laboratory, Moffett Field, CA, 1953.

[39] Moorhouse, D. J. and Woodcock, R. J., "Background Information And User Guide For MIL-F-8785C, Military Specification Flying Qualities Of Piloted Airplanes," Interim Report For Period May 1977 – May 1981 AFWAL-TR-81-3109, Flight Dynamics Laboratory, AF Wright Aeronautical Laboratories, AFSC, Wright-Patterson AFB, OH 45433, July 1982.

[40] Etkin, B., "Turbulence Wind and Its Effect on Flight," *Journal of Aircraft*, Vol. 15:5, 1981, pp. 327–45.

[41] Pamadi, B. N., *Performance, Stability, Dynamics, and Control of Airplanes*, chap. 1.6, AIAA, Reston, VA, 2nd ed., 2004.

[42] Thwaites, B., editor, *Incompressible Aerodynamics: An Account of the Theory and Observation of the Steady Flow of Incompressible Fluid Past Aerofoils, Wings, and Other Bodies*, Dover, Mineola, NY, 1987, pp. 34–35.

[43] Campbell, C. W., "A Spatial Model of Wind Shear and Turbulence for Flight Simulation," Tech. Rep. TP-2313, NASA George C. Marshall Space Flight Center, Alabama 35812, May 1984.

[44] Friedland, B., *Control System Design, An Introduction to State-Space Methods*, chap. 10, McGraw-Hill, Inc., New York, NY, 1986.

[45] Kim, E., *Control and Simulation of Relative Motion for Aerial Refueling in Race-track Maneuver*, MSAE thesis, The University of Texas at Arlington, Arlington, TX, May 2007.

[46] Dogan, A., Kim, E., and Blake, W., "Control and Simulation of Relative Motion for Aerial Refueling in Racetrack Maneuvers," *Journal of Guidance, Control and Dynamics*, Vol. 30, No. 5, 2007, pp. 1551–1557.

[47] McLean, D., *Automatic Flight Control Systems*, chap. 5, Prentice Hall International, Hemel Hempstead, Herts, UK, 1990.

BIOGRAPHICAL STATEMENT

TIMOTHY LEWIS was born in Corpus Christi, TX. Among his earliest childhood memories is making birthday cards on an Apple IIe. He has been using computers to solve problems his whole life. A parallel development has been his interest in aviation and space exploration. As a teenager, he sought to become an astronaut. In high school, he thrived in advanced calculus and physics courses. With these skills and interests, entering the aerospace engineering program at the University of Texas at Arlington was a natural decision.

In the undergraduate program at UTA, his favorite subjects included flight dynamics, modeling, simulation, and control. He continued these pursuits in the graduate program in the Computer Aided Control Systems Design (CACSD) Lab with Dr. Atilla Dogan. He accompanied Dr. Dogan to Wright–Patterson AFB, Ohio in Summer 2007 as part of the Air Force Research Laboratory, Air Vehicles Directorate Summer Research Program. This experience cemented his interest in working in a national research laboratory after completing his university education.

Timothy will pursue a Ph.D. in aerospace engineering at the Georgia Institute of Technology, beginning Fall 2008.